*Mathematical Biosciences and Engineering*

https://www.aimspress.com/journal/mbe

MBE, 23(4): 987–1049.
DOI: 10.3934/mbe.2026038
Received: 06 December 2025
Revised: 29 January 2026
Accepted: 05 February 2026
Published: 04 March 2026

*Research article*

# Immune dysregulation in COVID-19: Mathematical modeling of the within-host dynamics

**Keopagnapech Ngoun[1], Nicolas Alvarez[1,2], Ayesh Awad[3] and Hwayeon Ryu[2,*]**

[1] Department of Engineering, Elon University, 100 Campus Drive, Elon, NC, 27244, USA

[2] Department of Mathematics and Statistics, Elon University, 100 Campus Drive, Elon, NC, 27244, USA

[3] Center for Gastrointestinal Biology and Disease, University of North Carolina at Chapel Hill, 130 Mason Farm Road, Bioinformatics Building CB# 7080, Chapel Hill, NC, 27599, USA

* **Correspondence:** Email: hryu@elon.edu; Tel: +13362786451.

**Abstract:** The COVID-19 pandemic has spurred extensive research into viral transmission and control, yet the mechanisms of the human immune response to SARS-CoV-2 remain incompletely understood, particularly the role of natural killer (NK) cells and cytokine regulation in disease severity. Mathematical modeling provides a powerful approach to bridge this gap by linking viral dynamics with immune interactions. In this work, we developed a mechanistic within-host model, formulated in a system of coupled ordinary and delayed differential equations, to investigate the contributions of NK cell activity, interferon signaling, and pro-inflammatory cytokines to viral clearance and disease outcome. Model parameters were estimated from experimental data, and computational simulations were used to explore how dysregulated NK responses and cytokine feedback loops may drive divergent clinical outcomes. Local sensitivity analysis identified the most influential parameters shaping host–pathogen dynamics, highlighting potential control points for intervention. In addition, knockdown simulations were performed to mimic potential therapeutic interventions, allowing us to evaluate their advantages and limitations *in silico*. These findings provided mechanistic insights into COVID-19 immune dynamics and offered a foundation for guiding the design of future treatment strategies.

**Keywords:** mathematical modeling; COVID-19; immune response; sensitivity analysis; knockdown simulation
**Mathematics Subject Classification:** 92B05, 92C42, 37N25, 90C31

## 1. Introduction

Despite an extensive volume of research, the mechanisms governing host immune dynamics in COVID-19 remain incompletely understood. Severe disease is often associated with hyperinflammatory responses, yet many studies have relied on heterogeneous cohorts with limited longitudinal sampling and rarely integrate viral load, cytokine profiles, and immune-cell phenotypes within the same individuals across disease severity. Confounding factors such as vaccination status, prior infection, viral variants, and therapeutic interventions further complicate inference [1], while blood-based measurements may fail to capture immune activity in tissue compartments central to pathology [2, 3]. As a result, many findings remain correlative, leaving unresolved how cytokine programs shape immune cell transitions, which feedback loops govern disease resolution versus escalation, and when interventions are most effective [4, 5].

A hallmark pathology of severe COVID-19 is the cytokine storm, characterized by excessive cytokine release, immune cell over-activation, and tissue injury [6, 7]. Dysregulated innate and adaptive responses, including lymphopenia and overactivation of myeloid populations, contribute to lung injury, multi-organ failure, and poor prognosis [8, 9]. Among immune subsets, natural killer (NK) cell dysfunction has emerged as an important feature. Although NK cell numbers are generally preserved, their cytotoxic activity is impaired, often in the context of elevated interleukin-6 (IL-6) [10]. The underlying biology of this dysfunction remains poorly understood, and existing therapies, including corticosteroids [10], IL-6 inhibitors such as tocilizumab [11], and antivirals like Paxlovid [12], provide only partial benefits. These findings highlight the need for deeper mechanistic insight into NK biology and its integration within the broader immune response.

Mathematical modeling has provided valuable tools to explore host–virus interactions in COVID-19. Differential equation frameworks have been used to capture viral kinetics together with elements of the innate and adaptive immune response. Such models have reproduced observed clinical trajectories, including viral load dynamics, lymphocyte depletion, and cytokine production, while also generating mechanistic hypotheses to explain differences between mild and severe cases [13–15]. By explicitly linking viral replication with immune-mediated control, these efforts have underscored how the timing and coordination of immune responses strongly influence disease outcomes.

Among a series of previous within-host modeling studies [16–24], the earlier work based on ordinary differential equations (ODEs) [16, 18] have focused on therapeutic interventions in an animal model of COVID-19. Their results showed that antiviral effectiveness depends critically on both potency and initiation time, and predicting scenarios of viral rebound under short-course early treatment. Later work [25, 26] incorporated dense, daily viral load sampling (obtained from human subjects) into mechanistic models to quantify heterogeneity in viral expansion, clearance, and peak timing, while also linking viral load trajectories to infectiousness. A more recent model [27] extended and unified these approaches by analyzing a large dataset of viral loads (obtained from the daily testing program of the National Basketball Association), identifying six distinct shedding patterns and modeling how immune timing and intensity explain divergent peak loads, durations, and rebound phenomena. Collectively, these studies highlight how individual-level variation in immune and viral dynamics shapes both therapeutic outcomes and transmission potential, while emphasizing the central role of immune heterogeneity and treatment timing in controlling infection.

Despite these advances, NK cells are often absent from within-host models or represented only in

highly simplified terms. One recent effort explicitly included NK cells [28], but considered only simplified cytokine-mediated dynamics, leaving NK cell dysfunction unexplored. Other models treat NK cells as generic innate effectors that aid early viral clearance, without accounting for their context-dependent impairment [15, 29]. Yet clinical studies suggest that NK cells, while numerically preserved in many COVID-19 patients, exhibit impaired cytotoxic function, particularly in the presence of elevated IL-6 [30–33]. The failure to capture these altered effector functions limits our ability to use models to probe how NK dysfunction contributes to uncontrolled inflammation or prolonged viral persistence. Likewise, the within-host studies (e.g., [16, 18, 25–27]) did not explicitly distinguish disease severity by immune or cytokine responses, largely due to limited experimental data. Incorporating NK dysfunction and cytokine-mediated pathways into a model could therefore provide new insights into the cellular feedback loops that drive divergent clinical trajectories between mild and severe disease.

In addition to NK dynamics, cytokine signaling pathways remain incompletely represented in previous modeling frameworks. While type I interferons (IFN-$\alpha$ or IFN-$\beta$) are often included [14], type II IFN (IFN-$\gamma$) and tumor necrosis factor-$\alpha$ (TNF-$\alpha$) are rarely modeled despite evidence linking their dysregulation to severe outcomes [7, 34–38].

TNF-$\alpha$ is a pro-inflammatory mediator that recruits immune cells but can also exacerbate pathology [39–42]. Elevated TNF-$\alpha$ levels are observed in severe COVID-19 [6, 7, 43], where it drives infiltration of NK cells, macrophages, neutrophils, and dendritic cells [41, 44]. Anti-TNF-$\alpha$ therapies have been proposed [44, 45] and shown to reduce hospitalization risk among infected patients [46], though their prophylactic use in uninfected populations remains uncertain and ethically challenging.

IFN-$\gamma$ is another cytokine implicated in COVID-19 pathogenesis, with both antiviral and immunoregulatory functions [47, 48]. Although protective in many infectious diseases [49, 50] and retaining antiviral activity in COVID-19 [51], reports of IFN-$\gamma$ levels are inconsistent across severities [7, 34–36]. Some studies link high IFN-$\gamma$ to severe disease, others to diminished expression in critical cases, underscoring its complex role. In addition, a study [52] suggested that IFN-$\gamma$ and TNF-$\alpha$ may act synergistically. They showed both trigger macrophage apoptosis, suggesting targeted inhibition could mitigate immunopathology. This synergy highlights a critical but underexplored mechanism of COVID-19 and underscores the need for models that jointly incorporate IFN-$\gamma$ and TNF-$\alpha$.

Here, we develop a mathematical model of SARS-CoV-2 infection that explicitly incorporates NK cytotoxic function and the interactions of TNF-$\alpha$ and IFN-$\gamma$ with both innate and adaptive immune responses. Our goal is to move beyond correlative findings and generate mechanistic insights into how specific cytokine programs and immune subsets drive divergent clinical trajectories. By anchoring our framework to prior modeling efforts and clinical observations, we aim to clarify how NK cells and cytokine interactions contribute to immune dysregulation, to identify control points that tip the balance between viral clearance and immunopathology, and to provide testable predictions for the targeting of immunomodulatory therapies. Ultimately, this work seeks to advance mechanistic understanding of COVID-19 pathogenesis and inform future therapeutic strategies.

Our paper is structured as follows: Section 2 provides the description of the mathematical model we developed (Section 2.1), the model equations (Section 2.2), the parameter estimation and numerical simulations (Section 2.3), and the well-posedness and positivity of solutions of the model (Section 2.4). Section 3 provides our main results for mild versus severe disease (Section 3.1), for

local sensitivity analysis (Section 3.2), and for *in silico* knockdown analysis on selected immune cells from mild disease (Section 3.3) and on pro-inflammatory cytokines from severe case (Section 3.4). We discuss our main findings in a broader context, model limitations, and suggestions for future work in Section 4. The appendix materials provide more details on the process of parameter estimation and homeostasis calculation, and additional model results.

## 2. Mathematical model and methods

### *2.1. Model description*

To study the dynamics of SARS-CoV-2 infection and the immune cell dysfunctions responsible for severe disease case, we develop a mathematical model of host-pathogen interactions, adapted and substantially expanded from [14]. While the previous work of [14] focused on type I IFN dynamics against COVID-19 virus and its relationship to disease severity, we additionally incorporate IFN-$\gamma$, TNF-$\alpha$, and NK cells into our model due to their critical roles in immune response to COVID-19. IFN-$\gamma$ is a pleiotropic cytokine, which acts as a potent antiviral agent, but can induce excessive macrophage apoptosis [53, 54]. TNF-$\alpha$ is a pro-inflammatory cytokine responsible for the up-regulated production of other pro-inflammatory cytokines [45] and the recruitment of NK cells. NK cell dysfunction is observed in severe cases of COVID-19, causing substantially less infected cells to be eliminated [55].

Figure 1 shows a schematic diagram of our model which consists of three main sets of components: lung epithelial cells, immune cells (both innate and adaptive), and cytokines. Susceptible lung epithelial cells ($S$) that encounter SARS-CoV-2 ($V$) may become infected ($I$), as shown in Figure 1A. Upon infection, the immune response is orchestrated by cytokines that stimulate resident immune cell subsets and recruit additional cells from the bone marrow and circulation. Infected cells either die ($D$) due to viral cytopathic effects or immune-mediated killing by inflammatory macrophages ($M_{\Phi I}$), neutrophils ($N$), $CD8^+$ T cells ($T$), or NK cells ($K$), or they produce new viruses through replication. Infected cells also secrete type I IFN [56], which induce resistance in lung epithelial cells ($R$) and thereby limit further viral infection [57].

The dynamics of inflammatory macrophages are governed by three distinct pathways: (i) conversion of tissue-resident alveolar macrophages ($M_{\Phi R}$) in response to dead or infected cells [58], (ii) activation of alveolar macrophages by IFN-$\gamma$ or TNF-$\alpha$ [59], and (iii) differentiation of monocytes ($M$) stimulated by IL-6, TNF-$\alpha$, and granulocyte-macrophage colony-stimulating factor (GM-CSF) [60]. Monocytes, recruited by infected cells and GM-CSF, therefore represent a key precursor population. Once differentiated, inflammatory macrophages clear dead cells but eventually undergo exhaustion (leading to cell death) during this process. Neutrophils ($N$) are recruited by IL-6 and G-CSF [61], and can induce collateral damage in both infected and uninfected epithelial cells [62, 63]. Their levels increase in COVID-19, further elevated by G-CSF and IL-6, which are strongly up-regulated in severe cases [6]. As part of the adaptive immune response, cluster of differentiation 8-positive T ($CD8^+$ T) cells ($T$) are recruited to infection sites following antigen recognition, with their expansion modulated positively by type I IFN and negatively by IL-6 [64–66].

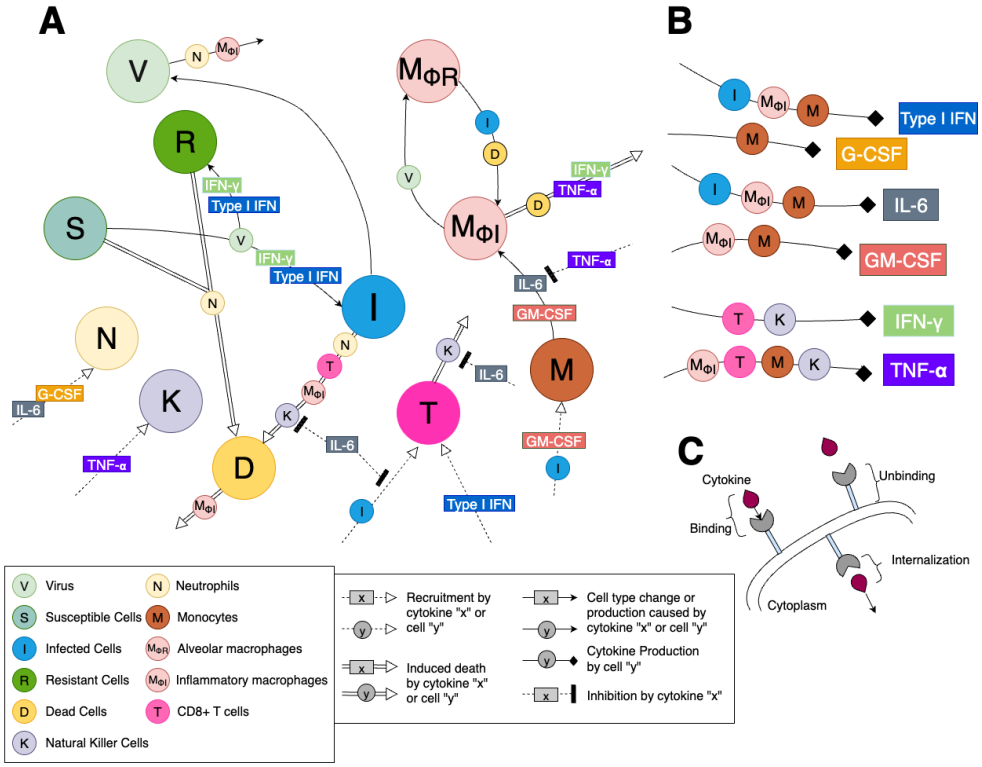


**Figure 1.** Schematic diagram of immune response to SARS-CoV-2 model. The model in Eqs (2.1)–(2.23) is illustrated by the detailed dynamics **A)** for cells, cytokines, and their interactions, **B)** for cytokine production, and **C)** for cell-cytokine binding kinetics. Different lines represent cell recruitment (dotted line with triangle arrow), induced cell death (double line), cell type change or production (solid line with triangle arrow), cytokine production (solid line with rhombus arrow), and cytokine inhibition (dotted line with rectangle arrow). **A)** Virus ($V$) infects susceptible lung epithelial cells which can then turn into infected ($I$) or resistant ($R$) cells depending on the concentration of type I IFN and of IFN-$\gamma$. Infected cells can die and produce new virus (i.e., viral replication) or can be removed by inflammatory macrophages ($M_{\Phi I}$), CD8$^+$ T cells ($T$), neutrophils ($N$), or NK cells ($K$) via apoptosis induction to become dead cells ($D$). NK cells eliminate target cells and are recruited by TNF-$\alpha$ while IL-6 can inhibit the cytotoxic activity of NK cells. Neutrophils can cause collateral damage (death) in all epithelial cells, including healthy ones, and are recruited by G-CSF and IL-6 concentrations. CD8$^+$ T cells are recruited by infected cells and up-regulated by type I IFN concentration while the T cell recruitment being inhibited by IL-6 concentration. Monocytes ($M$) are recruited by infected cells and GM-CSF, then differentiate into inflammatory macrophages based on the concentrations of GM-CSF and IL-6. This differentiation process can be inhibited by TNF-$\alpha$. Tissue-resident macrophages ($M_{\Phi R}$) also become inflammatory macrophages in response to the presence of dead and infected cells. The death of inflammatory macrophages can be induced by dead cells, TNF-$\alpha$, and IFN-$\gamma$. Inflammatory macrophages are responsible for clearing up dead cells. **B)** Type I IFN is produced by infected cells, inflammatory macrophages, and monocytes while IFN-$\gamma$ by T cells and NK cells. Monocytes are the sole producer of G-CSF. Both monocytes and inflammatory macrophages serve as producers for IL-6 and GM-CSF though IL-6 is also produced by infected cells. Inflammatory macrophages, T cells, monocytes, and NK cells all produce TNF-$\alpha$. **C)** Each cell-cytokine interaction modeled includes cytokine receptor binding, internalization process, and unbinding kinetics.

The production dynamics of cytokines are summarized in Figure 1B. IFN-$\gamma$ is primarily produced by T cells and NK cells, enacting antiviral mechanisms [53]. TNF-$\alpha$, largely secreted by inflammatory macrophages and monocytes [67, 68], contributes to the excessive inflammation observed in severe patients [44]. Monocytes serve as major cytokine producers, generating all cytokines in the model except IFN-$\gamma$ [69]. IL-6 not only drives monocyte-to-macrophage differentiation but also inhibits key processes, such as T cell recruitment by infected cells and NK cell–mediated clearance of infected cells [33]. G-CSF, produced solely by monocytes, further amplifies neutrophil responses. Cytokines function via receptor-mediated binding. Only free, unbound cytokines can signal effectively [70]; hence, our model explicitly distinguishes between bound and unbound cytokines, with receptor binding, internalization, and unbinding kinetics, as illustrated in Figure 1C.

### *2.2. Model equations*

Our model is formulated as a system of twenty-three coupled nonlinear ordinary and delay differential equations (Eqs (2.1)–(2.23)) for eleven cell populations and six cytokines, in which, for each cytokine, both unbound and bound concentrations are modeled explicitly. The dynamics for lung epithelial cells are adapted from [14], except that IFN-$\gamma$ now affects the infection and viral replication processes alongside type I IFN (see Figure 1A). In addition, constants for each cytokine's average receptor number used in the corresponding equations (i.e., Eqs (2.12)–(2.23)) are provided in (A.1)–(A.6). Tables 1 and 2 list the variables and selected biological pathways represented in the equations.

The complete list of model parameters and their values is summarized in Tables A.1–A.12 in appendix materials. Throughout the model, interactions between cytokines and cells are described by both positive (stimulatory) and negative (inhibitory) Hill functions, respectively:

$$\frac{p\,Z^h}{Z^h + s^h}, \qquad \frac{p\,s^h}{Z^h + s^h},$$

where $Z$, $s$, $h$, and $p$ denote the interacting component, its half-effect value, the Hill coefficient, and the interaction rate, respectively [71, 72]. In what follows, the production (or recruitment/differentiation) rate of a given cell $X$ by cytokine $Y$ is denoted by $p_{X,Y}$; the half-effect concentration (i.e., $s$ in the Hill function above) of cytokine $X$ acting on cell population $Y$ by $\epsilon_{X,Y}$; and the half-effect concentration of cell $Y$ affecting cytokine $X$ by $\eta_{X,Y}$. The natural death rate of cell $Y$ is denoted by $d_Y$, and the rate of induced death of cell $Y$ by cell $Z$ by $\delta_{Y,Z}$. Lastly, the proliferation rate of cell $Y$ is denoted by $\lambda_Y$, with carrying capacity $Y_{\max}$.

$$\frac{dV}{dt} = \overbrace{pI}^{a} - \delta_{V,M_\Phi} M_{\Phi I} V - \delta_{V,N} N V - d_V V, \tag{2.1}$$

$$\frac{dS}{dt} = \lambda_S \left(1 - \frac{S + I + R + D}{S_{max}}\right) S - \beta S V - \overbrace{\frac{\rho \delta_N S N^{h_N}}{N^{h_N} + IC_{50,N}^{h_N}}}^{b}, \tag{2.2}$$

$$\frac{dI}{dt} = \overbrace{\frac{\beta}{2}\left(\frac{\epsilon_{F,I}}{F_B+\epsilon_{F,I}}+\frac{\epsilon_{\gamma,I}}{\gamma_B+\epsilon_{\gamma,I}}\right)S(t-\tau_I)V(t-\tau_I)}^{c} - \overbrace{\left(\frac{\delta_{I,K}KI}{K+\epsilon_{K,I}}\right)\left(\frac{\epsilon_{L,K}}{L_B+\epsilon_{L,K}}\right)}^{d} - \frac{\delta_N I N^{h_N}}{N^{h_N}+IC_{50,N}^{h_N}} \tag{2.3}$$
$$- \delta_{I,M_{\Phi I}} M_{\Phi I} I - \delta_{I,T} T I - d_I I,$$

$$\frac{dR}{dt} = \lambda_S\left(1-\frac{S+I+R+D}{S_{max}}\right)R + \overbrace{\frac{\beta}{2}\left(\frac{F_B}{F_B+\epsilon_{F,I}}+\frac{\gamma_B}{\gamma_B+\epsilon_{\gamma,I}}\right)S(t-\tau_I)V(t-\tau_I)}^{c} - \frac{\rho\delta_N R N^{h_N}}{N^{h_N}+IC_{50,N}^{h_N}}, \tag{2.4}$$

$$\frac{dD}{dt} = d_I I + \frac{\delta_N(\rho S+\rho R+I)N^{h_N}}{N^{h_N}+IC_{50,N}^{h_N}} + \delta_{I,M_{\Phi I}} M_{\Phi I} I + \delta_{I,T} T I - d_D D \tag{2.5}$$
$$+ \overbrace{(\delta_{M_\Phi,D}-\delta_{D,M_\Phi})(M_{\Phi R}+M_{\Phi I})D}^{e} + \overbrace{\left(\frac{\delta_{I,K}KI}{K+\epsilon_{K,I}}\right)\left(\frac{\epsilon_{L,K}}{L_B+\epsilon_{L,K}}\right)}^{d} + \overbrace{\left(\frac{\delta_{M_{\Phi I},\gamma}\gamma_B\alpha_B}{\gamma_B\alpha_B+\epsilon_{M_{\Phi I},\gamma}}\right)M_{\Phi I}}^{f},$$

$$\frac{dM_{\Phi I}}{dt} = a_{I,M_{\Phi I}} M_{\Phi R}(I+D) + \overbrace{\frac{p_{M_{\Phi I},G}G_B^{h_{M,M_{\Phi I}}}M}{G_B^{h_{M,M_{\Phi I}}}+\epsilon_{G,M_{\Phi I}}^{h_{M,M_{\Phi I}}}}}^{g} + \overbrace{\left(\frac{p_{M_{\Phi I},L}L_B M}{L_B+\epsilon_{L,M_{\Phi I}}}\right)\left(\frac{\epsilon_{\alpha,M_{\Phi I}}^{h_{M_{\Phi I},\alpha}}}{\alpha_B^{h_{M_{\Phi I},\alpha}}+\epsilon_{\alpha,M_{\Phi I}}^{h_{M_{\Phi I},\alpha}}}\right)}^{h} \tag{2.6}$$
$$- \delta_{M_\Phi,D} D M_{\Phi I} - d_{M_{\Phi I}} M_{\Phi I} - \lambda_{M_{\Phi R}}\left(1-\frac{M_{\Phi R}}{M_{\Phi max}}\right)\frac{M_{\Phi I}}{V+\epsilon_{V,M_{\Phi R}}} - \overbrace{\left(\frac{\delta_{M_{\Phi I},\gamma}\gamma_B\alpha_B}{\gamma_B\alpha_B+\epsilon_{M_{\Phi I},\gamma}}\right)M_{\Phi I}}^{f},$$

$$\frac{dM_{\Phi R}}{dt} = -a_{I,M_{\Phi I}} M_{\Phi R}(I+D) - \delta_{M_\Phi,D} D M_{\Phi R} + \lambda_{M_{\Phi R}}\left(1-\frac{M_{\Phi R}}{M_{\Phi max}}\right)\frac{M_{\Phi I}}{V+\epsilon_{V,M_{\Phi R}}} - d_{M_{\Phi R}} M_{\Phi R}, \tag{2.7}$$

$$\frac{dK}{dt} = K_{prod}^* K_R + \frac{p_{K,\alpha}\alpha_B K}{\alpha_B+\epsilon_{\alpha,K}} - d_K K, \tag{2.8}$$

$$\frac{dT}{dt} = \frac{p_{T,I} I(t-\tau_T)\epsilon_{L,T}}{L_B+\epsilon_{L,T}} + \overbrace{\frac{p_{T,F}F_B T}{F_B+\epsilon_{F,T}}}^{i} - \overbrace{\left(\frac{\delta_{T,K}TK}{K+\epsilon_{K,T}}\right)\left(\frac{\epsilon_{L,K}}{L_B+\epsilon_{L,K}}\right)}^{j} - d_T T, \tag{2.9}$$

$$\frac{dM}{dt} = \overbrace{\left(M_{prod}^* + \left(\psi_{M_{max}} - M_{prod}^*\right)\frac{G_B^{h_M}}{G_B^{h_M}+\epsilon_{G,M}^{h_M}}\right)M_R}^{k} + \frac{p_{M,I} I M}{I+\epsilon_{I,M}} - \overbrace{\frac{p_{M_{\Phi I},G}G_B^{h_{M,M_{\Phi I}}}M}{G_B^{h_{M,M_{\Phi I}}}+\epsilon_{G,M_{\Phi I}}^{h_{M,M_{\Phi I}}}}}^{g} \tag{2.10}$$
$$- \overbrace{\left(\frac{p_{M_{\Phi I},L}L_B M}{L_B+\epsilon_{L,M_{\Phi I}}}\right)\left(\frac{\epsilon_{\alpha,M_{\Phi I}}^{h_{M_{\Phi I},\alpha}}}{\alpha_B^{h_{M_{\Phi I},\alpha}}+\epsilon_{\alpha,M_{\Phi I}}^{h_{M_{\Phi I},\alpha}}}\right)}^{h} - d_M M,$$

$$\frac{dN}{dt} = \left(N_{prod}^* + \left(\psi_{N_{max}} - N_{prod}^*\right)\frac{C_{BF}-C_{BF}^*}{C_{BF}-C_{BF}^*+\epsilon_{C,N}}\right)N_R + \frac{p_{N,L}L_B}{L_B+\epsilon_{L,N}} - d_N N, \tag{2.11}$$

$$\frac{dL_U}{dt} = \overbrace{\frac{p_{L,I}I}{I+\eta_{L,I}} + \frac{p_{L,M_{\Phi I}}M_{\Phi I}}{M_{\Phi I}+\eta_{L,M_{\Phi I}}} + \frac{p_{L,M}M}{M+\eta_{L,M}}}^{l} - \overbrace{k_{lin_L}L_U}^{m} - \overbrace{k_{B_L}((M+N+T)A_L - L_B)L_U}^{n} + \overbrace{k_{U_L}L_B}^{o}, \tag{2.12}$$

$$\frac{dL_B}{dt} = -\overbrace{k_{int_L}L_B}^{p} + \overbrace{k_{B_L}((M+N+T)A_L - L_B)L_U}^{n} - \overbrace{k_{U_L}L_B}^{o}, \tag{2.13}$$

$$\frac{dF_U}{dt} = \frac{p_{F,I}I}{I+\eta_{F,I}} + \frac{p_{F,M_{\Phi I}}M_{\Phi I}}{M_{\Phi I}+\eta_{F,M_{\Phi I}}} + \frac{p_{F,M}M}{M+\eta_{F,M}} - k_{lin_F}F_U - k_{B_F}((I+T)A_F - F_B)F_U + k_{U_F}F_B, \tag{2.14}$$

$$\frac{dF_B}{dt} = -k_{int_F}F_B + k_{B_F}((I+T)A_F - F_B)F_U - k_{U_F}F_B, \tag{2.15}$$

$$\frac{d\gamma_U}{dt} = \frac{p_{\gamma,T}T}{T+\eta_{\gamma,T}} + \frac{p_{\gamma,K}K}{K+\eta_{\gamma,K}} - k_{lin_\gamma}\gamma_U - k_{B_\gamma}\left((I+T+M_{\Phi I})A_\gamma - \gamma_B\right)\gamma_U + k_{U_\gamma}\gamma_B, \tag{2.16}$$

$$\frac{d\gamma_B}{dt} = -k_{int_\gamma}\gamma_B + k_{B_\gamma}\left((I+T+M_{\Phi I})A_\gamma - \gamma_B\right)\gamma_U - k_{U_\gamma}\gamma_B, \tag{2.17}$$

$$\begin{aligned}\frac{d\alpha_U}{dt} =& \frac{p_{\alpha,T}T}{T+\eta_{\alpha,T}} + \frac{p_{\alpha,M_{\Phi I}}M_{\Phi I}}{M_{\Phi I}+\eta_{\alpha,M_{\Phi I}}} + \frac{p_{\alpha,M}M}{M+\eta_{\alpha,M}} + \frac{p_{\alpha,K}K}{K+\eta_{\alpha,K}} - k_{lin_\alpha}\alpha_U \\ & - k_{B_\alpha}\left((I+T+M_{\Phi I}+K+M)A_\alpha - \alpha_B\right)\alpha_U + k_{U_\alpha}\alpha_B,\end{aligned} \tag{2.18}$$

$$\frac{d\alpha_B}{dt} = -k_{int_\alpha}\alpha_B + k_{B_\alpha}\left((I+T+M_{\Phi I}+K+M)A_\alpha - \alpha_B\right)\alpha_U - k_{U_\alpha}\alpha_B, \tag{2.19}$$

$$\frac{dG_U}{dt} = \frac{p_{G,M_{\Phi I}}M_{\Phi I}}{M_{\Phi I}+\eta_{G,M_{\Phi I}}} + \frac{p_{G,M}M}{M+\eta_{G,M}} - k_{lin_G}G_U - k_{B_G}\left(MA_G - G_B\right)G_U + k_{U_G}G_B, \tag{2.20}$$

$$\frac{dG_B}{dt} = -k_{int_G}G_B + k_{B_G}\left(MA_G - G_B\right)G_U - k_{U_G}G_B, \tag{2.21}$$

$$\frac{dC_U}{dt} = \frac{p_{C,M}M}{M+\eta_{C,M}} - k_{lin_C}C_U - k_{B_C}\left(NA_C - C_B\right)(C_U)^W + k_{U_C}C_B, \tag{2.22}$$

$$\frac{dC_B}{dt} = -k_{int_C}C_B + k_{B_C}\left(NA_C - C_B\right)(C_U)^W - k_{U_C}C_B. \tag{2.23}$$

The dynamics for virus $V$, susceptible $S$, infected $I$, resistant $R$, and dead $D$ cells (in Eqs (2.1)–(2.5)) are adapted from [14] with the effect of additional terms including NK cells, IFN-$\gamma$, and TNF-$\alpha$ incorporated. Virus replicates at rate of $p$ (pathway $a$) from infected cells while its clearance is modulated by inflammatory macrophages via apoptosis and neutrophils. The susceptible cell population is governed by a logistic growth at rate $\lambda_S$, their infection interacting with virus at rate $\beta$, and bystander damage of epithelial cells by neutrophils (pathway $b$) through the release of reactive oxygen species [62, 63] using a Hill function.

The concentrations of bound type I IFN ($F_B$) and bound IFN-$\gamma$ ($\gamma_B$) regulate the creation of infected and resistant cells [51, 73] in that the increased concentrations of both IFNs make more cells to become resistant to infection while making less cells infected, as reflected in Eqs (2.3) and (2.4) or pathway $c$. The potency of this regulation is governed by the half-effect parameters, $\epsilon_{F,I}$ and $\epsilon_{\gamma,I}$. The delay $\tau_I$ represents the eclipse phase (i.e., time elapsed between successful cell infection and the start of virus production), after which infected cells begin to actively produce virus until undergoing their lytic death at rate $d_I$. Though various immune cells contribute to the clearance of infected cells, in our model we consider only macrophages and CD8$^+$ T cells, which lead to the apoptosis-induced death at rates $\delta_{I,M_{\Phi I}}$

and $\delta_{I,T}$, respectively. Moreover, the last term of Eq (2.3) (pathway $d$) shows that the killing of infected cells by NK cells is inhibited by IL-6 to include a biologically realistic representation of NK cell's limited role in COVID-19 [32].

Dead cells ($D$) are accumulated through several ways: infected cell lysis $d_I$, neutrophil damage of all epithelial cells $\delta_N$, the induced death of infected cells via macrophage phagocytosis $\delta_{I,M_{\Phi I}}$, $CD8^+$ T cell killing $\delta_{I,T}$, NK killing $\delta_{I,K}$, macrophage exhaustion from clearing up dead cells $\delta_{M_\Phi,D}$ [74], and inflammatory macrophage death (of PANoptosis) synergistically modulated by both IFN-$\gamma$ and TNF-$\alpha$ (see pathway $f$) with $\delta_{M_{\Phi I},\gamma}$ and half-effect $\epsilon_{M_{\Phi I},\gamma}$ [52]. These dead cells degrade at a relatively high rate $d_D$ [75] while being cleared up through phagocytosis by macrophages at rate $\delta_{D,M_\Phi}$.

**Table 1.** List of model variables and their description in Eqs (2.1)–(2.23).

| Variable | Description | Unit |
|---|---|---|
| $V$ | Viral load | cop/ml |
| $S$ | Susceptible cells | $10^9$ cells/ml |
| $I$ | Infected cells | $10^9$ cells/ml |
| $R$ | Resistant cells | $10^9$ cells/ml |
| $D$ | Dead cells | $10^9$ cells/ml |
| $M_{\Phi I}$ | Inflammatory macrophages | $10^9$ cells/ml |
| $M_{\Phi R}$ | Alveolar (or resident) macrophages | $10^9$ cells/ml |
| $K$ | NK cells | $10^9$ cells/ml |
| $T$ | $CD8^+$ T cells | $10^9$ cells/ml |
| $M$ | Monocytes | $10^9$ cells/ml |
| $N$ | Neutrophils | $10^9$ cells/ml |
| $K_R$ | Bone marrow reservoir NK cells | $10^9$ cells/ml |
| $M_R$ | Bone marrow reservoir monocytes | $10^9$ cells/ml |
| $N_R$ | Bone marrow reservoir neutrophils | $10^9$ cells/ml |
| $L_{U,B}$ | Unbound ($U$) or bound ($B$) IL-6 | pg/ml |
| $F_{U,B}$ | Unbound or bound type I IFN | pg/ml |
| $\gamma_{U,B}$ | Unbound or bound IFN-$\gamma$ | pg/ml |
| $\alpha_{U,B}$ | Unbound or bound TNF-$\alpha$ | pg/ml |
| $G_{U,B}$ | Unbound or bound GM-CSF | pg/ml |
| $C_{U,B}$ | Unbound or bound G-CSF | pg/ml |
| $C_{BF}$ | Neutrophil G-CSF receptor bound fraction | unitless |

**Table 2.** Description of selected biological pathways in Eqs (2.1)–(2.23).

| Pathway | Description |
|---|---|
| $a$ | Cellular lysis |
| $b$ | Destruction of susceptible cells by neutrophils |
| $c$ | Type I IFN and IFN-$\gamma$ inhibition of viral replication |
| $d$ | IL-6 inhibition of infected cells killed by NK cells |
| $e$ | Macrophage exhaustion for dead cells |
| $f$ | Macrophage cell death synergistically induced by IFN-$\gamma$ and TNF-$\alpha$ |
| $g$ | GM-CSF-induced monocyte differentiation to inflammatory macrophages |
| $h$ | IL-6-induced monocyte differentiation inhibited by TNF-$\alpha$ |
| $i$ | T cell proliferation by type I IFN |
| $j$ | T cell clearance by NK cells, which is inhibited by IL-6 |
| $k$ | Pharmacokinetics and pharmacodynamics of GM-CSF on monocytes |
| $l$ | Production of IL-6 stimulated by infected cells, macrophages, and monocytes |
| $m$ | IL-6 renal clearance |
| $n$ | IL-6 binding |
| $o$ | IL-6 unbinding |
| $p$ | IL-6 internalization |

The production of inflammatory macrophages ($M_{\Phi I}$) is regulated by three different pathways (acting individually or in concert): a transition from alveolar macrophages stimulated by infected and dead cells at a maximum rate $a_{I,M_{\Phi I}}$, monocytes differentiation stimulated by GM-CSF ($G_U$ and $G_B$) with a maximum production rate $p_{M_{\Phi I},G}$ and half-effect $\epsilon_{G,M_{\Phi I}}$ (in pathway $g$), and monocyte differentiation by IL-6 ($L_U$ and $L_B$) with a maximum production rate $p_{M_{\Phi I},L}$ and half-effect $\epsilon_{L,M_{\Phi I}}$ (in pathway $h$), as shown in the first three terms of Eq (2.6). Specifically, the IL-6-dependent monocyte differentiation (i.e., pathway $h$) is inhibited by TNF-$\alpha$ because its presence derives monocyte differentiation more toward dendritic cells than macrophages [76, 77]. The next two terms in Eq (2.6) represent the induced death of macrophage from clearing dead cells $\delta_{M_\Phi,D}$ and natural death $d_{M_{\Phi I}}$, respectively. The logistic term with $M_{\Phi max}$ models that the inflammatory macrophages replenish the alveolar macrophage population in the lung as the virus is cleared, thus, the replenishment of alveolar macrophages is inversely proportional to viral load with half-effect $\epsilon_{V,M_{\Phi R}}$. Resident macrophages are similarly modeled to undergo a switch to inflammatory macrophages stimulated by infected and dead cells, their replenishment as the virus is cleared up, macrophage exhaustion from dead cell clearance at rate $\delta_{M_\Phi,D}$, and natural death at rate $d_{M_{\Phi R}}$.

NK cells ($K$) are modeled to stay at their homeostasis level with reservoir release rate $K^*_{prod}$ before infection, after which more NK cells are actively recruited by TNF-$\alpha$ [78] with a maximum rate $p_{K,\alpha}$ and half-effect $\epsilon_{\alpha,K}$. They are cleared through natural death at rate $d_K$.

The population of CD8$^+$ T cells ($T$) is governed by the delay differential equation (2.9) where the first term describes cell recruitment at rate $p_{T,I}$ with the delay $\tau_T$. The delay period accounts for the time needed for the arrival of effector CD8$^+$ T cells at the infection site following dendritic cell activation, their migration to the lymph nodes, and the activation of CD8$^+$ T cells. In this term, inhibition by IL-6 concentration (bound $L_B$) is incorporated with half effect $\epsilon_{L,T}$ given that high

concentrations of IL-6 result in $CD8^+$ T cell exhaustion [79, 80]. In severe COVID-19 cases, impaired or delayed IFN signaling leads to defective virus-specific T cell activation and proliferation, which ultimately contributes to profound T cell lymphopenia [81, 82]. Thus, it is assumed that the expansion (or proliferation) process of the T cell population is mediated by type I IFN, as described in the pathway $i$ with the Hill function. In addition, IL-6 has been found to contribute to NK cell dysfunction in target cell recognition [83] in severe COVID-19. Thus, T cells are modeled to be targeted (and cleared) by NK cells at rate of $\delta_{T,K}$ (pathway $j$) but this clearance is inhibited by the IL-6 concentration. T cell apoptosis occurs at rate $d_T$.

Craig et al. [84] have shown that even under normal, healthy conditions (i.e., at homeostasis), endogeneous cytokine levels are not static or in a near-equilibrium state. To describe the pharmacokinetics and pharmacodynamics of cytokine binding and unbinding processes, we use the framework established in [84]. The general form of the pharmacokinetic relationship is given by

$$\begin{aligned} \frac{dC_U}{dt} &= C_P - k_e C_U - k_B(SA_C - C_B)C_U^W + k_U C_B, \\ \frac{dC_B}{dt} &= -k_{int} C_B + k_B(SA_C - C_B)C_U^W - k_U C_B, \end{aligned} \tag{2.24}$$

where $C_U$ and $C_B$ are unbound and bound cytokines with $k_U$ and $k_B$ being respective unbinding and binding rates, respectively. $C_P$ is the rate of endogeneous cytokine production, $k_{int}$ is the internalization rate of bound cytokine, and $k_e$ is the elimination rate. Here, $W$ is a stoichiometric constant and the sum concentration of all cells modulated by this cytokine $C$ denoted by $S$. The calculation of a scaling factor $A_C$ is determined by

$$A_C = \hat{p} C_W R 10^n,$$

where $\hat{p}$ is a constant relating the stoichiometry between cytokine molecules and their receptors, $R$ is the number of receptors to each cytokine on a cell's surface, and $10^n$ is a correcting factor for cellular units (see Eqs (A.1)–(A.6)). The molecular weight is based on a standard calculation by dividing the cytokine's molar mass (MM) by Avogadro's number (i.e., $C_W = MM/(6.02214 \times 10^{23})$). The cytokine concentration is then governed by the above expressions (2.24) and additional terms representing interactions of bound components with immune cells.

The dynamics for monocytes $M$ and neutrophils $N$ (Eqs (2.10) and (2.11), respectively) interacting with cytokines are adapted from [14, 84], based on the cell-cytokine interaction using the Hill function, and the pharmacokinetics and pharmacodynamics of GM-CSF on monocytes and of G-CSF on neutrophils [85]. Specifically, as shown in pathway $k$, monocytes are recruited by bound GM-CSF [86] with bone marrow monocytes ($M_R$) recruited at a homeostatic rate $M^*_{prod}$. This recruitment rate increases up to maximum rate $\psi_{M_{max}}$ modulated by GM-CSF. In addition, infected cells produce monocytes at a maximal rate of $p_{M,I}$ with half-effect $\epsilon_{I,M}$, but they will subsequently differentiate to inflammatory macrophages (as above in pathway $g$) or go through natural death at rate $d_M$. Neutrophil recruitment from bone marrow reservoir neutrophils ($N_R$) is similarly modeled with the bound fraction of G-CSF [84] ($C_{BF} = C_B(t)/(A_C N(t))$) with its maximal value $\psi_{N_{max}}$. During the acute phase of inflammation, IL-6 is produced by endothelial cells, which leads to the attraction of neutrophils [87]. This recruitment is described in the second term of Eq (2.11) with maximal rate $p_{N,L}$ and half-effect parameter $\epsilon_{L,N}$. Neutrophils die at rate $d_N$.

Model equations for cytokine production (Figure 1B) are provided in Eqs (2.12)–(2.23). Unbound IL-6 ($L_U$) is produced by infected cells, inflammatory macrophages, and monocytes (pathway $l$), with bound IL-6 ($L_B$) resulting from binding to receptors on the surface of neutrophils, $CD8^+$ T cells, and monocytes (pathway $n$). Though unbound type I IFNs ($F_U$) are known to be secreted by multiple cell types upon viral infection, including lymphocytes, macrophages, endothelial cells, and fibroblasts [73], we model its unbound production from infected cells, inflammatory macrophages, and monocytes, and its binding to receptors on both $CD8^+$ T cells and infected cells to produce bound type I IFN ($F_B$). While type I IFN is secreted upon viral infection, IFN-$\gamma$ ($\gamma_U$ and $\gamma_B$) is secreted later due to delay in $CD8^+$ T cell arrival at the infection site. Unbound IFN-$\gamma$ production is modulated by $CD8^+$ T cells and NK cells with bound IFN-$\gamma$ produced via binding to receptors of infected cells, $CD8^+$ T cells, and macrophages. Unbound TNF-$\alpha$ ($\alpha_U$) are produced by inflammatory macrophages, monocytes, and NK and $CD8^+$ T cells. Though the programmed death of infected cells induced by TNF-$\alpha$ [88] was not incorporated due to its insignificant effect in our model dynamics, binding of TNF-$\alpha$ to the receptors of infected as well as all other immune cells interacting with TNF-$\alpha$ is added in Eq (2.18). Unbound GM-CSF ($G_U$) is assumed to be produced from inflammatory macrophages and monocytes with bound GM-CSF ($G_B$) produced via binding to monocyte receptors. The production of GM-CSF by $CD8^+$ T cells [89] is excluded due to its insignificant effect in the full model's dynamics. Lastly, unbound G-CSF ($C_U$) is secreted by monocytes, and bound to neutrophil receptors to produce bound G-CSF ($C_B$).

### *2.3. Parameter estimation and numerical simulation*

Model parameters for our model (Eqs (2.1)–(2.23)) are provided in appendix materials, and they were determined through direct extraction from literature and curve fitting to capture empirical effects (by following similar data-fitting methods, e.g., `fmincon` or `lsqnonlin` functions in MATLAB) with data used in [14]. Initial values for the model variables are summarized in Table A.1. Data needed for NK cells, two added cytokines IFN-$\gamma$ and TNF-$\alpha$, and their interactions with other components in the model were adapted from either existing data for SARS-CoV-2, or previous work for Middle East respiratory syndrome coronavirus (MERS-CoV) or SARS-CoV [90, 91], if needed and applicable. Any remaining parameters were calculated to preserve homeostatic equilibrium in healthy condition (i.e., in the absence of infection). A comprehensive description of the parameter estimation process can be found in appendix materials.

With the model with all calibrated parameters, we numerically solved our model using `ode45` and `ddesd` in MATLAB to conduct the model validation against data and obtain all simulation results that follow. All codes used for model analysis are provided to replicate our results presented herein. See Data Availability for more information.

### *2.4. Well-posedness and positivity of solutions*

We assume nonnegative initial conditions for all state variables and strictly positive parameter values for all rate constants and half-saturation (Hill) parameters (e.g., $IC_{50,\cdot} > 0$ and $\epsilon_\cdot > 0$), as summarized in Tables A.1–A.12. Under these assumptions, all denominators appearing in Hill-type expressions in the model are strictly positive for all time. In particular, for any state variable $X$, denominators of the form $X^h + \epsilon^h$ satisfy $X^h + \epsilon^h \geq \epsilon^h > 0$, and expressions such as $K + \epsilon_{K,I}$, $L_B + \epsilon_{L,\cdot}$, and $I + \epsilon_{I,M}$ (in Eqs (2.3),

(2.9), and (2.10), respectively) are bounded below by positive constants. Hence, the righthand sides of the model equations (Eqs (2.1)–(2.23)) are well-defined for all $t \geq 0$.

Moreover, our system is quasi-positive, implying that for a variable $X$, the corresponding righthand side satisfies

$$\left.\frac{dX}{dt}\right|_{X=0} \geq 0$$

provided that all remaining state variables are nonnegative. Specifically, when $D = 0$ in Eq (2.5), all terms that decrease $D$ (including the linear decay term and interaction terms proportional to $D$) vanish, while the remaining source terms are nonnegative, yielding $\left.\frac{dD}{dt}\right|_{D=0} \geq 0$. Similarly, when $M = 0$ in Eq (2.10) (respectively, $N = 0$ in Eq (2.11)), all loss terms proportional to $M$ (respectively, $N$) vanish and the remaining production or recruitment terms are nonnegative, implying $\left.\frac{dM}{dt}\right|_{M=0} \geq 0$ and $\left.\frac{dN}{dt}\right|_{N=0} \geq 0$. Therefore, solutions satisfy $D(t), M(t), N(t) \geq 0$, and, likewise, all other state variables remain nonnegative for all $t \geq 0$.

## 3. Main results

### *3.1. Model predictions for mild versus severe disease*

To identify key drivers that differentiate severe from mild dynamics, we numerically simulated our within-host model (Eqs (2.1)–(2.23)) with two contrasting parameter sets: a baseline set to reproduce mild disease dynamics and an adjusted set to recapitulate severe dynamics. In clinical COVID-19 studies [30, 69, 92, 93], patients with severe disease were reported to have significantly lower levels of type I IFN, along with elevated monocyte and IL-6 concentrations. Elevated IL-6, in particular, correlates with NK-cell dysfunction due to its inhibitory effect on cytolytic activity of NK cells. In addition, IFN-$\gamma$ production by $CD8^+$ T cells is impaired because the ratio of $CD4^+$ to $CD8^+$ T cells increases, and $CD8^+$ T cells produce more IFN-$\gamma$ than $CD4^+$ T cells [94].

To generate severe dynamics based on these observations, the rates of type I IFN production by infected cells ($p_{F,I}$), IFN-$\gamma$ production by T cells ($p_{\gamma,T}$), and the half-effect parameter for IL-6 inhibition of NK-cell cytotoxicity ($\epsilon_{L,K}$) were decreased, whereas the production rate of monocytes by infected cells ($p_{M,I}$) and the half-effect coefficient for type I IFN production by inflammatory macrophages ($\eta_{F,M_{\Phi I}}$) were increased. To ensure that all five parameters need to be changed to recapitulate severe disease, we systematically evaluated the effect of individual and partial parameter perturbations on model behaviors (results not shown). See Table A.2 for parameter modifications used for severe COVID-19 dynamics. Model predictions are compared in Figure 2, with mild disease shown as black solid lines and severe disease as red dashed lines. For model validation, viral loads from SARS-CoV-2 infection in humans reported in [95] (based on data from Singapore [96] and Germany [97]) were used, as indicated by open circles in Figure 2A.

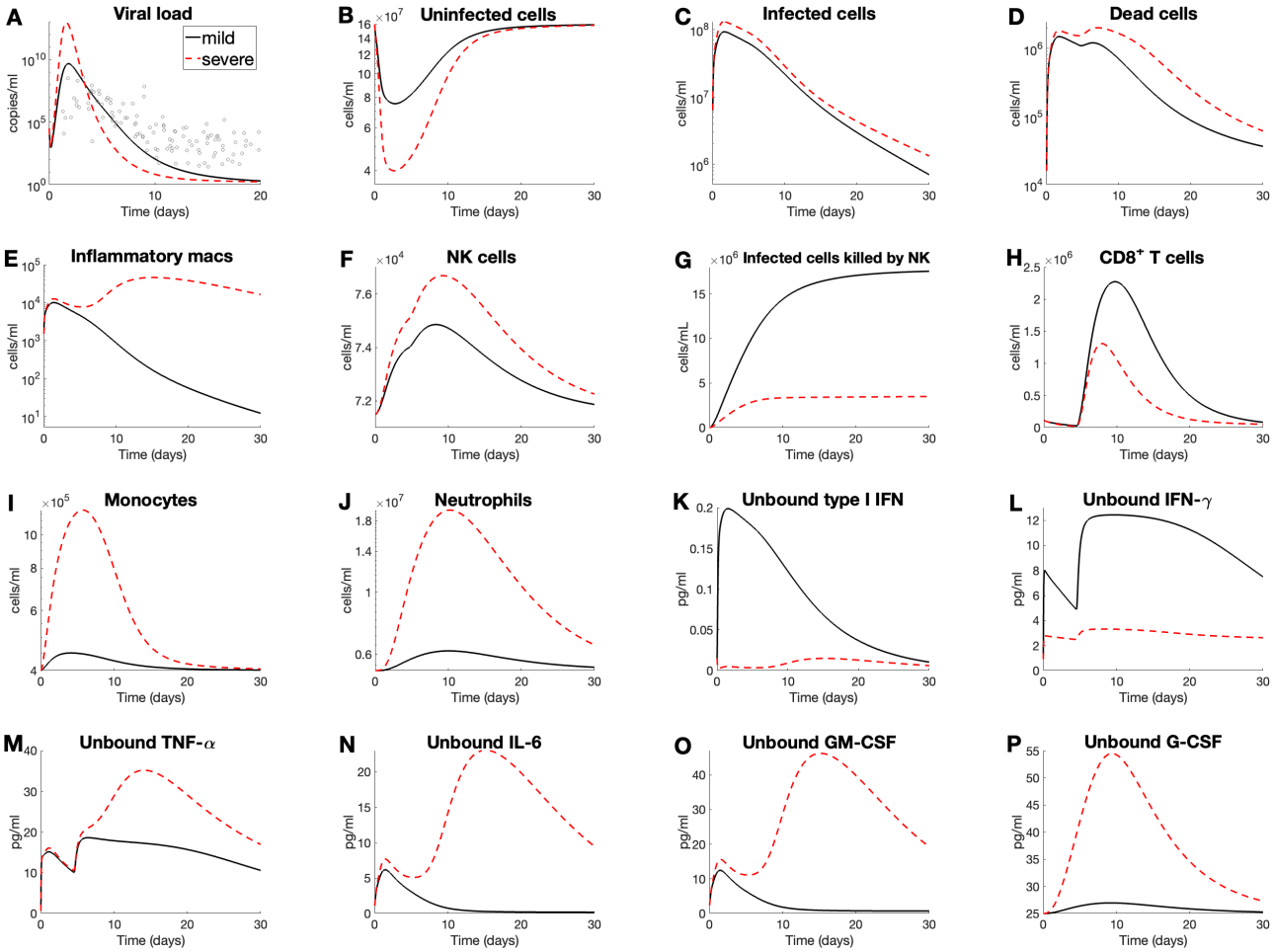


**Figure 2.** Model predictions for mild versus severe COVID-19 dynamics. Mild disease (solid lines) dynamics obtained by solving Eqs (2.1)–(2.23) with baseline parameters summarized in appendix materials. Viral load data (open circles) from eight human patients (three from Singapore and five from Germany by Goyal et al. [95]) are overlayed with predicted viral dynamics. Severe disease case (dashed lines) obtained by modifying selected parameters; decreasing production rate of type I IFN (via $p_{F,I}$ and $\eta_{F,M_\Phi}$), increasing monocyte recruitment rate ($p_{M,I}$), decreasing NK cell's cytotoxicity ($\epsilon_{L,K}$), and decreasing production rate of IFN-$\gamma$ by T cells ($p_{\gamma,T}$). The list of severe parameter values is summarized in Table A.2. The graphs depict the predicted concentrations of individual cell types or cytokines over the course of a 30-day infection. Only unbound cytokine concentrations (i.e., panels K)–P)) are shown, as these are clinically measurable and represent the pool available for receptor binding and downstream signaling. Time-series predictions of all other variables (i.e., including resident macrophages and all bound cytokines) are provided in appendix materials.

The mild case shows effective clearance of the virus within ~10 days, with all cell populations and cytokine concentrations returning to their respective homeostatic levels and only minimal tissue damage (Figure 2B). Specifically, the innate immune response is restrained: inflammatory macrophages, NK cells, monocytes, and neutrophils reach their peaks within 10 days post-infection

(Figure 2E,F,I,J), followed by CD8$^+$ T-cell activation peaking after day 10 (Figure 2H). The cytokine dynamics in mild disease demonstrate a rapid response in type I IFN, IL-6, and GM-CSF (Figure 2K,N,O, respectively). The dynamics of IFN-$\gamma$ and TNF-$\alpha$ (Figure 2L,M) are distinct in that an initial rise occurs immediately after infection, followed by a rapid decline, after which concentrations reach their highest peak at around one week and remain at a relatively stable level for another week.

Using the adjusted parameter set, the model exhibits a dramatic shift in disease progression. Although the predicted viral load (Figure 2A) remains comparable to that of mild infection, the severe scenario is characterized by a cytokine storm, with heightened levels of TNF-$\alpha$, IL-6, GM-CSF, and G-CSF, consistent with experimental findings [6, 7, 45, 98]. This is accompanied by elevated ratios of innate to adaptive immune cells (Figure 2E–J) and substantial loss of healthy lung tissue (Figure 2B). We note that the peak value of the dead-cell compartment $D$ (Figure 2D) does not differ dramatically between mild and severe simulations. In our framework, severity is not determined solely by $\max_t D(t)$; rather, the severe case is distinguished by sustained dysregulated inflammation (cytokine-storm-like cytokine exposure and impaired resolution), which can drive pathology even when the instantaneous peak of $D$ is comparable. Accordingly, tissue injury can also be assessed via time-course burden measures (e.g., duration above baseline and/or cumulative damage), alongside cytokine exposure profiles.

Moreover, in severe cases the interferon response (Figure 2K,L) is characterized by a delayed and weakened peak of type I IFNs and by a comparatively reduced IFN-$\gamma$ peak relative to mild cases, aligning well with data presented in [6, 35, 93]. In contrast to mild disease, inflammatory macrophages and neutrophils remain elevated for at least 30 days after initial infection (Figure 2E,J). Notably, inflammation remains high in severe disease, with increased TNF-$\alpha$ and GM-CSF concentrations, despite the virus being cleared slightly faster ($\sim$1 day) than in mild disease (Figure 2A). The peak of inflammatory macrophages rises from $\sim 10^4$ cells/ml (mild) to $\sim 10^5$ cells/ml (severe).

The model also reproduces the substantial reduction in CD8$^+$ T-cell concentrations in severe case (Figure 2H), indicative of T-cell lymphopenia, consistent with clinical observations in patients with severe COVID-19 [90, 99]. Interestingly, even though NK-cell concentrations increase (Figure 2F), their cytotoxic ability against infected cells shows a marked threefold reduction (Figure 2G). This indicates impaired functional capacity, leading to NK-cell dysfunction [100]. Despite varying only five parameters ($p_{F,I}, p_{\gamma,T}, p_{M,I}, \epsilon_{L,K}, \eta_{F,M_{\Phi I}}$), the model generates a distinct severe case, with cytokine dynamics qualitatively consistent with clinical observations for type I IFN [93, 101], IFN-$\gamma$ [102], TNF-$\alpha$ [44], IL-6 [103, 104], and G-CSF [105, 106].

### *3.2. Sensitivity analysis identifies key pathways in the immune response to SARS-CoV-2 infection*

To further examine the effects of parameter variation, we conducted a local sensitivity analysis (LSA) by increasing each parameter value by 5% from its baseline set (used for the mild dynamics in Figure 2) and quantifying the resulting changes in selected variables to assess each parameter's impact on host–pathogen dynamics. For each perturbation, we recorded predictions for key outputs over a 30-day window, including viral load, immune cell activation, tissue damage, and cytokine exposure. These outputs were then compared with baseline simulation results, and relative changes were calculated.

To facilitate visualization, model outputs were normalized using $z$-scores [107]. This standardization subtracts the mean and divides by the standard deviation, placing variables with

different units on a common scale and enabling direct comparison of sensitivity magnitudes. Each parameter was assigned a sensitivity score, defined as the maximum absolute $z$-score across all outputs, and parameters were ranked accordingly; the top 23 most influential were selected for visualization in the heatmap of Figure 3A. The identified parameters include ones relating to virus productivity ($p, \delta_{V,N}$), the infected cell death by NK cells ($\delta_{I,K}, \epsilon_{K,I}$), macrophages and CD8$^+$ T cell dynamics ($M_{\Phi R,0}, p_{T,I}$), G-CSF ($k_{B_C}$), IL-6 ($p_{L,M_{\Phi I}}, k_{lin_L}, \eta_{L,M_{\Phi I}}$), and the production of TNF-$\alpha$, type I IFN, and IFN-$\gamma$ ($p_{\alpha,T}, p_{F,I}, p_{\gamma,T}$).

The heatmap shows the effects of perturbations on maximum viral load, maximum dead cells, minimum uninfected cells (tissue), peak immune cell concentrations (inflammatory macrophages, CD8$^+$ T cells, and NK cells), maximum infected cells killed by NK cells, and maximum unbound cytokine levels (IL-6, type I IFN, IFN-$\gamma$, and TNF-$\alpha$). Each heatmap cell represents the $z$-score-normalized deviation of a model output in response to a 5% parameter perturbation. The color scale ranges from blue (strong negative effect), through white (no effect), to red (strong positive effect), conveying both the magnitude and direction of influence while highlighting the most sensitive parameters. The maximum increase and maximum decrease values for each metric are listed in Table 3. In addition, time-series dynamics for viral load, uninfected cells (tissue), infected cells killed by NK cells, and unbound IL-6, IFN-$\gamma$, and TNF-$\alpha$ concentrations with the 5% increase of the selected parameters, which produce the maximum and minimum increases according to Table 3, are provided in Figure 3B–G.

In Figure 3A, a higher production rate of type I IFN by infected cells ($p_{F,I}$) results in increased levels of unbound type I IFN, i.e., maximum level as well as the total exposure, based on max($F_U$) and total($F_U$) defined as the area under the unbound type I IFN curve over the course of exposure, respectively. This is accompanied by a moderate increase in undamaged tissue (min($S + R$)) and a reduction in maximum dead cells (max($D$)). These findings are consistent with the important role of type I IFN in promoting antiviral responses during early infection [108]. In contrast, increasing the renal clearance rate of unbound type I IFN ($k_{lin_F}$) strongly decreases type I IFN levels, thereby impairing antiviral defense. This reduction is accompanied by moderate declines in uninfected and resistant cell populations (as also shown in Figure 3C), while effects on immune cells and other cytokine levels remain modest. These results underscore the importance of sustained IFN signaling for viral control and are consistent with clinical observations of augmented clearance phenomena [109]. Sensitivity results for IFN-$\gamma$ show similar trends: increasing the production rate of IFN-$\gamma$ by T cells ($p_{\gamma,T}$) promotes antiviral control, whereas increasing its renal clearance rate ($k_{lin_\gamma}$) impairs it, as further supported by Figure 3F.

Increasing the recruitment rate of T cells in response to infected cells ($p_{T,I}$) enhances T-cell expansion (max($T$)) and dead-cell accumulation, while reducing total type I IFN exposure. Minimum undamaged tissue, however, is unaffected. This suggests that enhanced T-cell recruitment promotes clearance of infected cells but has minimal impact on collateral tissue damage. Notably, NK-cell activity appears reduced despite stable NK-cell numbers (max($K$)), due to the substantial increase in dead cells driven by infected-cell clearance [110, 111].

**Table 3.** List of values for the maximum increase and maximum decrease of each metric.

| Output | Max virus ($\log_{10}$(copies/ml)) | Min tissue (cells/ml) | Max inflam. macs (cells/ml) | Max T cells (cells/ml) |
|---|---|---|---|---|
| Max increase | $k_{int_C}$: 0.49 | $k_{B_\gamma}$: $6.36 \times 10^5$ | $M_{\Phi R,0}$: $6.49 \times 10^2$ | $p_{T,I}$: $1.12 \times 10^5$ |
| Max decrease | $C_{U,0}$: −0.79 | $k_{lin_\gamma}$: $-6.33 \times 10^5$ | $C_{U,0}$: $-2.61 \times 10^2$ | $d_T$: $-0.79 \times 10^5$ |
| Output | Infected cells killed by NK (cells/ml) | Max IL-6 (pg/ml) | IFN-$\gamma$ (pg/ml) | TNF-$\alpha$ (pg/ml) |
| Max increase | $\delta_{I,K}$: $6.49 \times 10^5$ | $M_{\Phi R,0}$: 0.37 | $p_{\gamma,T}$: 0.5 | $p_{\alpha,T}$: 0.61 |
| Max decrease | $\epsilon_{I,K}$: $-8.3 \times 10^5$ | $k_{lin_L}$: −0.32 | $k_{lin_\gamma}$: −0.58 | $k_{lin_\alpha}$: −0.87 |

In addition, while increasing the initial number of resident macrophages ($M_{\Phi R,0}$) significantly decreases the exposure to type I IFN or IFN-$\gamma$, it leads to higher macrophage expansion ($\max(M_{\Phi I})$), elevated IL-6 levels ($\max(L_U)$), and increased maximum TNF-$\alpha$ levels ($\max(\alpha_U)$). The increase IL-6 level slightly reduces the number of infected cells cleared by NK cells due to stronger IL-6–mediated inhibition of NK cytotoxicity [55], as can be seen by comparing Figure 3D,E (especially in response to increased $M_{\Phi R,0}$). This reflects the strong role of macrophages in IL-6 production and its positive feedback on macrophage expansion [60]. While early macrophage presence and activation can enhance innate responses, excessive IL-6 promotes systemic inflammation and impairs balanced immunity, in part due to NK-cell dysfunction [112]. Moreover, the higher death rate of NK cells ($d_K$) significantly reduces NK cell population, which consequently impairs their cytotoxic function (Figure 3D) and decreases the production of IFN-$\gamma$ and TNF-$\alpha$ (Figure 3F,G).

A higher initial concentration of unbound G-CSF ($C_{U,0}$) or its binding rate ($k_{B_C}$) reduces peak viral load (Figure 3B), dead cells, macrophages, T cells, and concentrations of all cytokines considered in our LSA. This suggests that early G-CSF availability facilitates effective infection control, limiting the need for excessive immune activation and reducing tissue damage. It also implies the therapeutic potential of early G-CSF supplementation, although careful consideration of timing and dosage would be critical to avoid overstimulation or suppression of cytokine-mediated immune dynamics following intervention [113].

Although not explicitly shown in the heatmap in Figure 3A (but shown in the complete LSA results, provided in appendix materials), a higher viral infection rate ($\beta$) markedly increases viral load, tissue damage, and immune dysregulation, as expected. Elevated $\beta$ also drives higher levels of unbound IL-6 and type I IFN, consistent with uncontrolled viral replication leading to hyperinflammation and cytokine storm, as observed in patients with severe COVID-19 [114]. See appendix materials for more information.

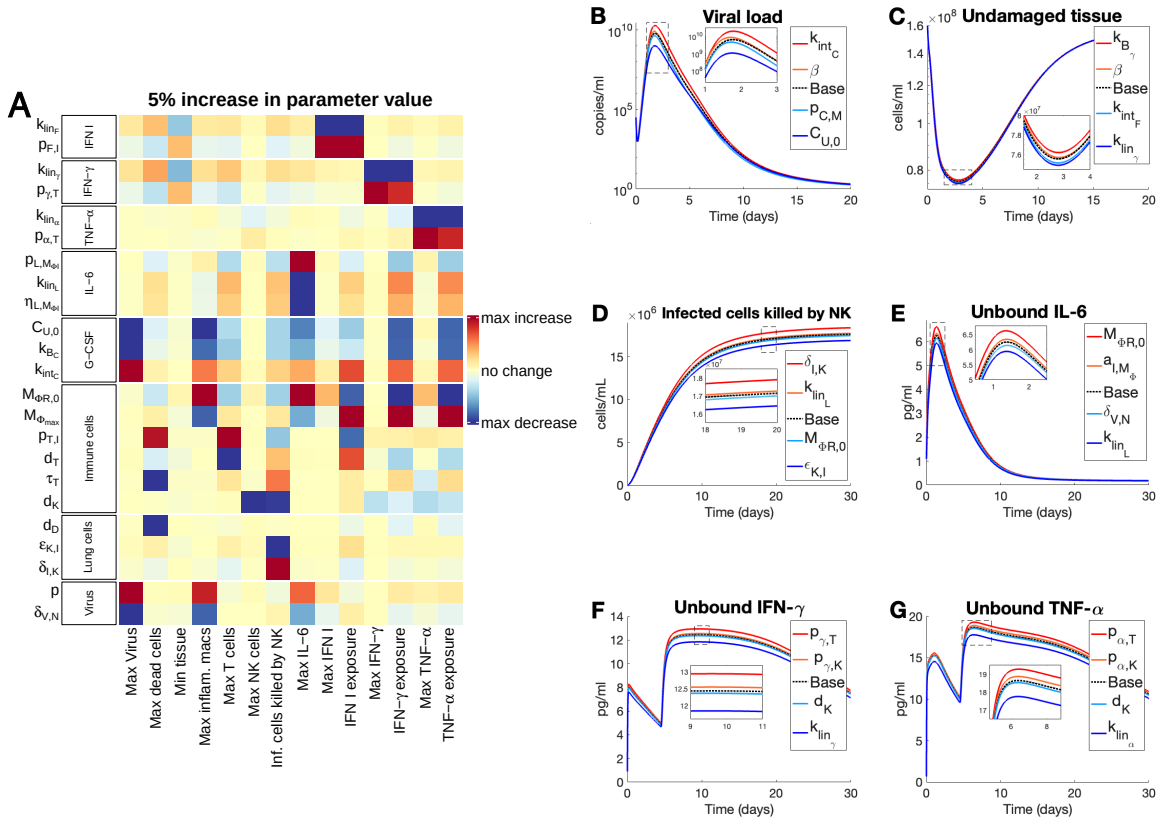


**Figure 3.** Top 23 sensitive parameters (with +5% perturbation) identified by local sensitivity analysis. Each parameter was increased by 5% from its originally estimated value (i.e., mild disease parameters in Figure 2) and the resulting model dynamics were simulated. Predictions were then compared to baseline specifically for maximum viral load (max($V$)), maximum concentration of dead cells (max($D$)), minimum uninfected cells or tissues (min($S+R$)), maximum concentrations of three immune cells–inflammatory macrophages (max($M_{\Phi I}$)), CD8$^+$ T cells (max($T$)), maximum concentration of NK cells (max($K$)), and maximum concentration of infected cells killed by NK. The maximum concentrations of the four cytokines, IL-6 (max($L_U$)), type I IFN (max($F_U$)), IFN-$\gamma$ (max($\gamma_U$)), and TNF-$\alpha$ (max($\alpha_U$)) along with the corresponding total exposure to the last three cytokines. **A)** Heat map shows the magnitude of the change of each metric from a 5% increase in the parameter value compared to baseline, where blue and red represent the maximum and minimum values, respectively, observed in the output metric. The top 23 most sensitive parameters (categorized by a group of IFN I, IFN-$\gamma$, TNF-$\alpha$, G-CSF, IL-6, immune cells, lung cells, and virus) are shown here, and for the complete parameter sensitivity results, see the appendix materials. The explicit value of the maximum increase and maximum decrease of each metric is given in Table 3 below. The $z$-score normalization was applied to account for differences in scale and units across outputs, allowing for meaningful comparison of sensitivity magnitudes across all variables. **B)–G)**: Time-series dynamics of viral load, undamaged tissue (uninfected cells), infected cells killed by NK cells, and unbound IL-6, IFN-$\gamma$, and TNF-$\alpha$ given 5% increases in the noted parameters for each color. Colors of the curves correspond to the coloring of the heatmap in **A)**.

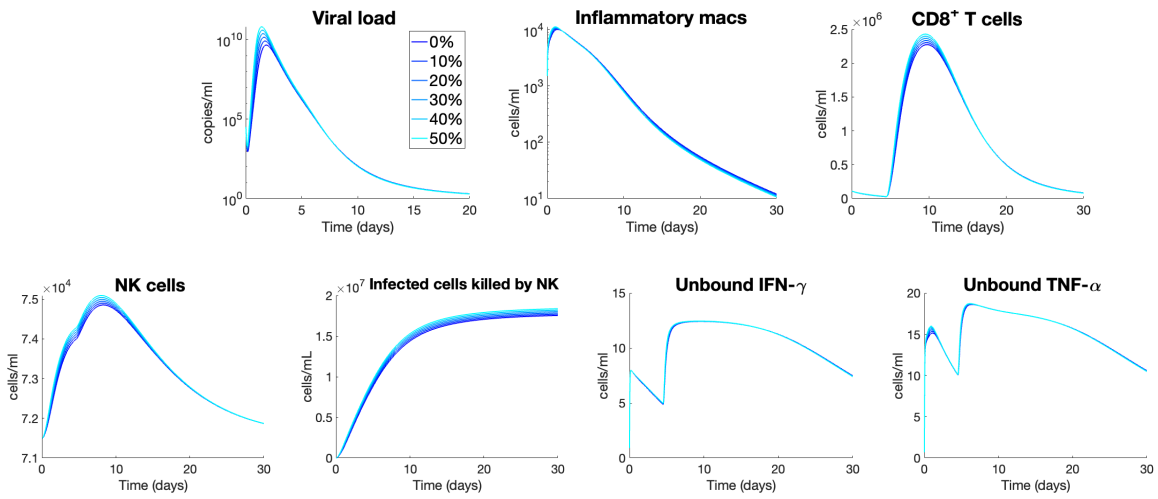


**Figure 4.** Viral infectivity rate $\beta$ has small effects on overall immune dynamics. Dynamics for viral load, inflammatory macrophage, $CD8^+$ T Cell, NK cells, and infected cells killed by NK cells, unbound IFN-$\gamma$, and unbound TNF-$\alpha$ are obtained using the baseline parameters (used for mild disease in Figure 2) except increasing the viral infection rate $\beta$ (by $0, 10, 20, 30, 40, 50\%$).

As noted in [14], the viral infectivity rate ($\beta$) can be influenced by viral mutations or varying densities of cellular angiotensin-converting enzyme 2 (ACE2) receptors between individuals. To assess whether the relative homogeneity of the immune response is preserved especially with new cytokine interactions added to our model, we varied the viral infectivity rate ($\beta$) by the same amount (0–50% with increments of 10%) and the corresponding results for viral load, inflammatory macrophages, T cells, NK cells, infected cells killed by NK, and unbound IFN-$\gamma$ and TNF-$\alpha$ were recorded in Figure 4. Although some variability is observed, both qualitative and quantitative behaviors including the shape and maximum concentrations of cytokines, including IFN-$\gamma$ and TNF-$\alpha$, remain largely similar to the baseline case simulations. In addition, changes in inflammatory macrophages, T cells, NK cells, and NK cell cytotoxicity are minimal with their qualitative behaviors preserved. Importantly, viral load remains relatively the same except the higher peaks as $\beta$ increases, suggesting that the increased infectivity alone is not sufficient to significantly alter disease progression and severity.

### 3.3. *In silico knockdown analyses reveal how immune status influences disease outcomes*

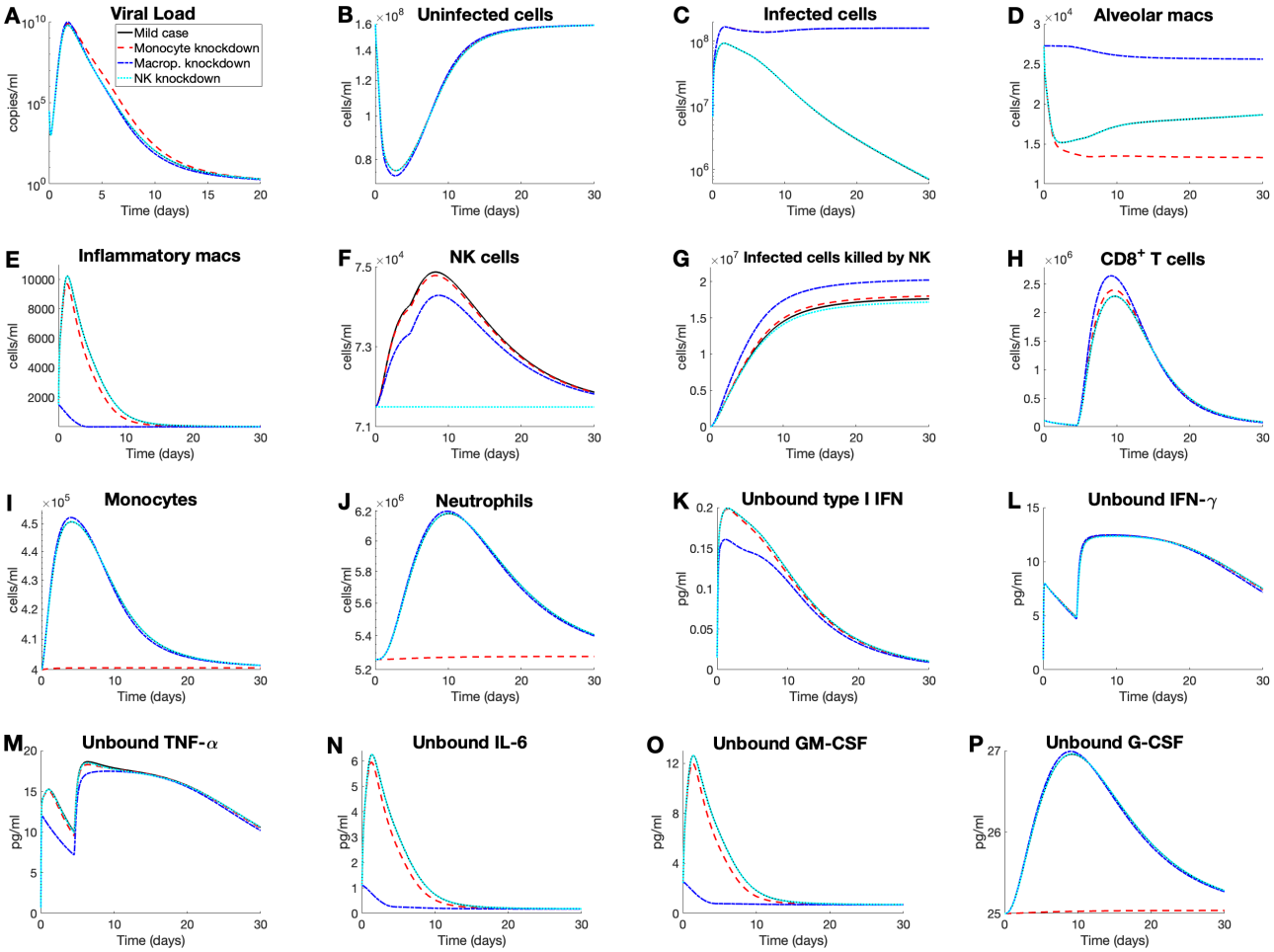


**Figure 5.** Effects of monocyte, macrophage, and NK cells knockdown on mild disease courses. *In silico* knockdown experiments in the mild disease scenario (as shown in Figure 2; black solid line) were performed by implementing the recruitment knockdown of monocytes (i.e., no monocyte recruitment; red dash line), of inflammatory macrophages (i.e., not inflammatory macrophage creation via antigen stimulation or monocyte differentiation; blue dash-dot line), and of neutrophils (i.e., no neutrophil recruitment; cyan dot line), while keeping homeostasis and death rates the same. Model dynamics of the *in silico* knockdown are shown for A) viral load, B) uninfected cells, C) infected cells, D)–J): immune cells and infected killed by NK cells (panel G), and K)–P): unbound cytokines.

To assess the specific contributions of innate immune subsets to disease progression, we performed a series of *in silico* knockdown experiments. We focused on the mild disease course (Figure 2, black solid line), since severe cases already involve systemic dysregulation, making it difficult to isolate the effects of individual cell types. In each simulation, recruitment of a given immune cell population was set to zero while initial abundances and death rates were left unchanged. Specifically, neutrophil recruitment was set to $p_{N,L} = 0$; inflammatory macrophage creation and recruitment to $a_{I,M_{\Phi I}} = p_{M_{\Phi I},L} = p_{M_{\Phi I},G} = 0$;

monocyte recruitment and differentiation to $p_{M,I} = p_{M_{\Phi I},G} = p_{M_{\Phi I},L} = 0$; and NK cell recruitment to $p_{K,\alpha} = 0$. The resulting dynamics are summarized in Figure 5.

In the monocyte knockdown (red dashed line), loss of monocyte recruitment disrupted alveolar macrophages, NK-cell activity, neutrophil counts, and G-CSF concentration (Figure 5D–F,J,P). Because monocytes are precursors to macrophages [115], their absence caused a marked reduction in resident macrophages. Monocytes also promote production of most cytokines except IFN-$\gamma$ (Figure 1B); accordingly, cytokine levels declined, with G-CSF showing the sharpest decrease (Figure 5P). Reduced G-CSF lowered neutrophil recruitment (Figure 5J). Although monocytes do not directly affect NK-cell numbers, the higher pool of infected cells increased NK-mediated killing (Figure 5G). Viral load was slightly prolonged (Figure 5A), indicating delayed clearance [116].

When inflammatory macrophages were knocked down (blue dash-dotted line), IL-6 and GM-CSF levels were most affected (Figure 5N,O). Without macrophages, innate cytokine signaling was broadly impaired, reducing type I IFN, TNF-$\alpha$, IL-6, and GM-CSF production (Figure 5K,M–O), consistent with their central role in cytokine secretion (Figure 1C). Viral control was also compromised, with sustained high numbers of infected cells (Figure 5C) [117, 118]. Macrophage loss decreased TNF-$\alpha$ (Figure 5M), reducing NK recruitment (Figure 5F). However, the elevated infected-cell burden boosted NK-mediated killing (Figure 5G), underscoring compensatory interactions among innate subsets.

In the NK-cell knockdown (cyan dotted line), cytokine dynamics were largely unchanged, but infected-cell clearance was modestly impaired (Figure 5G) [119]. Viral load and uninfected-cell trajectories were nearly identical across knockdowns (Figure 5A–C), illustrating the immune system's ability to buffer the loss of individual components.

Across all knockdown scenarios, $CD8^+$ T cells were maintained or slightly elevated relative to the mild case (Figure 5H). This suggests that adaptive responses compensated for innate dysfunction, preserving viral clearance and IFN-$\gamma$ dynamics (Figure 5A,L). Importantly, none of the knockdowns reproduced the hallmarks of severe disease (e.g., loss of uninfected lung tissue, expansion of inflammatory macrophages; Figure 5B,E). Thus, while individual innate-cell perturbations altered immune trajectories, severe disease emerges from systemic dysregulation rather than the loss of a single cell subset.

### *3.4. In silico cytokine knockdown investigations suggest therapeutic treatments for severe disease*

To evaluate whether limiting specific pro-inflammatory cytokines can mitigate disease severity and point toward therapeutic strategies, we simulated knockdowns of IL-6, TNF-$\alpha$, and IFN-$\gamma$ on the severe disease trajectory (from Figure 2, red dashed line), as summarized in Figure 6. In each case, cytokine production terms were set to zero for their modeled sources: for IL-6 ($p_{L,I} = p_{L,M_{\Phi I}} = p_{L,M} = 0$), TNF-$\alpha$ ($p_{\alpha,T} = p_{\alpha,M} = p_{\alpha,K} = 0$), and IFN-$\gamma$ ($p_{\gamma,K} = p_{\gamma,T} = 0$). Note that though TNF-$\alpha$ is predominantly recruited by inflammatory macrophages, their recruitment rate (i.e., $p_{\alpha,M_{\Phi I}}$) was kept at nonzero to mimic the most realistic medical knockdown intervention while focusing more on the potential effects of cytokine knockdown on NK cell function.

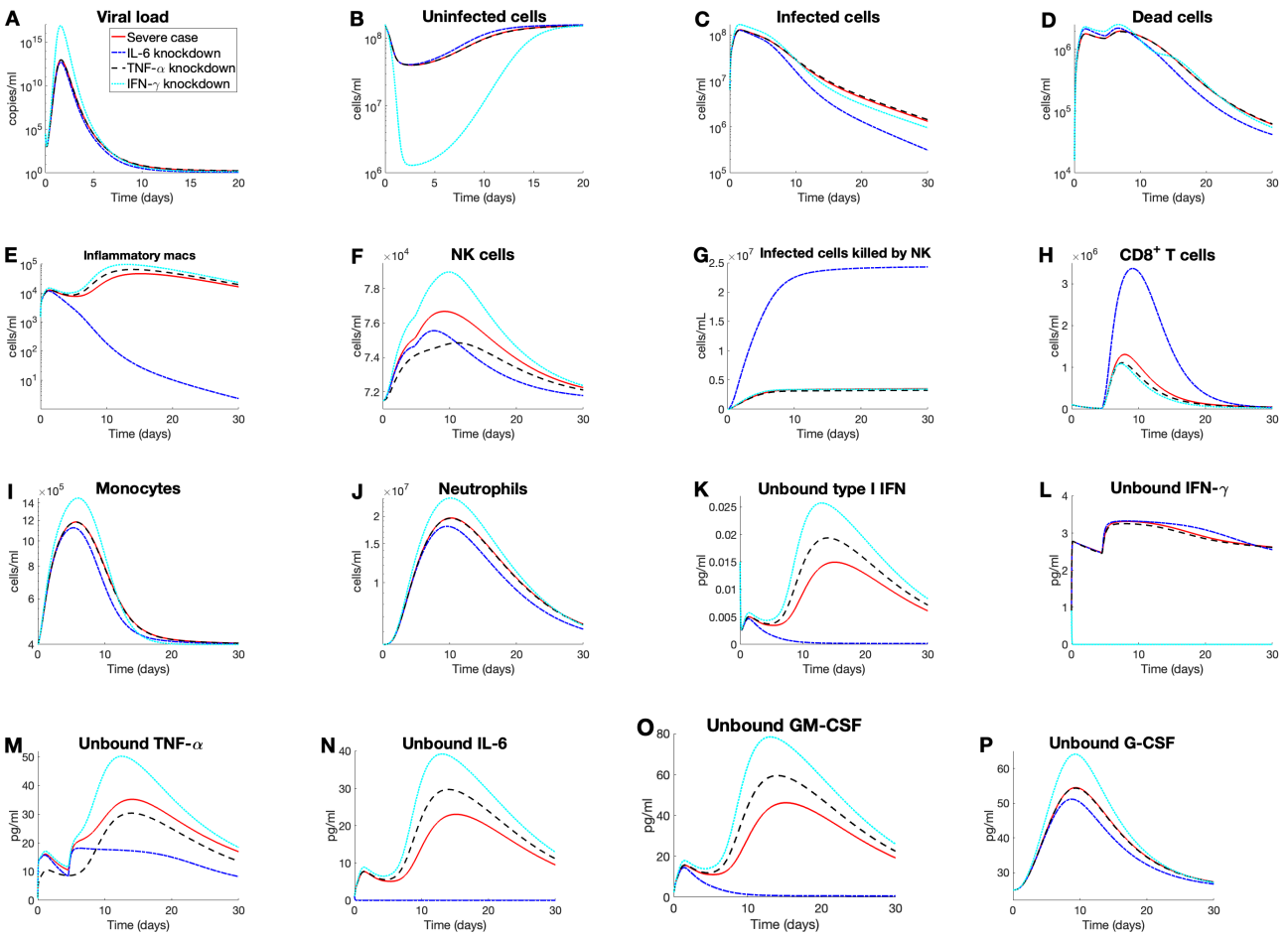


**Figure 6.** Effects of IL-6, TNF-$\alpha$, and IFN-$\gamma$ knockdown on severe disease courses. We performed *in silico* knockdown experiments in the severe disease scenario (Figure 2; red solid line) by knocking down the production of IL-6 (by infected cells, inflammatory macrophages, and monocytes; blue dash-dot line), of TNF-$\alpha$ (by CD8$^+$ T cells and monocytes; black dash line), and of IFN-$\gamma$ (by NK and CD8$^+$ T cells; cyan dot line). Model dynamics of the *in silico* knockdown are plotted for A) viral load, B)–D) lung cells, E)–J) immune cells and infected cells killed by NK cells (panel G), and K)–P) unbound cytokines.

**IL-6 knockdown** IL-6 knockdown scenario results in a markedly rapid decline in infected cells, less tissue damage, and higher population of CD8$^+$ T cells, compared to TNF-$\alpha$ and IFN-$\gamma$ knockdowns (Figure 6B–D,H). This is consistent with clinical finding that IL-6 contributes to hyper-inflammation and cytokine storm, which can exacerbate the severity of COVID-19, for example, with elevated infected cells and tissue damage but reduced T-cell activity [112, 120, 121]. In addition, limiting IL-6 production leads to substantially reduced macrophage population, highlighting its role in macrophage activation and recruitment in lung tissue [58]. Specifically, given that IL-6 induces the differentiation of the recruited monocytes to inflammatory macrophages [60], its blockage could mitigate the immune response from excessive inflammation (Figure 6E). In contrast, the CD8$^+$

T cell response is notably enhanced by IL-6 knockdown, given the inhibitory role of IL-6 in T cell expansion [122], leading to an elevated peak comparable to a mild case, as can be seen by comparing Figure 2H (black solid line) and Figure 6H (blue dash-dot line).

IL-6 knockdown markedly lowers NK-cell abundance with peaks falling to ~75% of the severe-case level (Figure 6F), suggesting that, although IL-6 contributes to NK dysfunction in severe inflammation, it supports NK-cell maintenance under inflammatory stress and, most importantly, restores the ability for NK cells to kill infected cells (Figure 6G).

In addition to immune cell activities, IL-6 knockdown significantly reduces the concentrations of all cytokines except IFN-$\gamma$. Both type I IFN and GM-CSF are suppressed (Figure 6K,O, respectively), consistent with their dependence on monocytes and inflammatory macrophages (Figures 1B and 6E). While IL-6 knockdown dampens macrophage-driven inflammation, as mentioned above, it also weakens early antiviral defenses and may impair viral clearance [123]. Moreover, the near-absence of GM-CSF and, consequently, a reduction in recruited monocytes (Figure 6O,I, respectively) indicate IL-6 as a major upstream driver in severe disease [124]; given GM-CSF's roles in leukocyte recruitment and lung tissue support [86], its depletion in the absence of IL-6 risks delayed resolution and prolonged infection. Overall, IL-6 knockdown, while beneficial in reducing inflammatory damage, may suppress critical immune functions required for effective viral clearance and tissue homeostasis.

The concentration of G-CSF, a cytokine central to neutrophil production, maturation, and function [85], is lowered by IL-6 knockdown (Figure 6P). While the reduced IL-6 production may alleviate hyper-inflammation in severe COVID-19, the accompanying G-CSF drop can impair neutrophil responses (Figure 6J) and weaken host defense [125], underscoring a therapeutic trade-off between dampening inflammation and preserving immune competence. Also, the IL-6/TNF-$\alpha$ axis shows reciprocal control: IL-6 knockdown reduces TNF-$\alpha$ by limiting macrophage activation, whereas TNF-$\alpha$ knockdown elevates IL-6 by removing regulatory restraint (Figure 6M,N; Figure 1). Therapeutically, perturbing either node can shift the balance toward under- or over-production of the other, with implications for inflammation control and tissue protection [126, 127]. Lastly, IL-6 knockdown exerts time-dependent effects on IFN-$\gamma$ (Figure 6L) in that its level rises around 10–20 days after symptom onset but drops below severe case after 20 days, suggesting more prolonged inflammation.

**IFN-$\gamma$ knockdown** IFN-$\gamma$ knockdown produces a higher NK-cell peak than the severe case (Figure 6F), consistent with IFN-$\gamma$-mediated negative feedback on NK cells [128]. Despite increased NK cell population, however, IFN-$\gamma$ blockage leads to the increased peak of viral load but lowered T-cell level (Figure 6A,H, respectively) while having excessive inflammation, as well demonstrated by elevated concentrations for all other cytokines. This finding implies that IFN-$\gamma$ is detrimental to viral clearance and T cell level [129, 130], and its loss destabilizes immune regulation.

**TNF-$\alpha$ knockdown** Finally, TNF-$\alpha$ knockdown yields a stronger net anti-inflammatory effect in NK cell proliferation (Figure 6F), reflecting TNF-$\alpha$'s critical role in NK activation, proliferation, and survival [78]. The reduced NK cell population subsequently descreases IFN-$\gamma$ recruitment (as shown in Figures 1B and 6L). Despite the overall reduction in inflammatory signaling, however, inflammatory macrophages increase slightly (Figure 6E) because TNF-$\alpha$ regulates macrophage

activity and limits monocyte differentiation to inflammatory macrophages. Thus, its loss may lessen macrophage apoptosis and remove this restraint, allowing accumulation [131]. Consistent with increased macrophage numbers, GM-CSF rises during TNF-$\alpha$ knockdown (Figure 6O), as GM-CSF production tracks monocyte/macrophage abundance and TNF-$\alpha$ normally inhibits their differentiation/activation [76]. The observed elevation of GM-CSF following TNF-$\alpha$ suppression may indicate a compensatory mechanism possibly aimed at sustaining macrophage function despite the loss of TNF-$\alpha$ signaling. TNF-$\alpha$ knockdown also elevates type I IFN (Figure 6K), suggesting that TNF-$\alpha$ may exert a negative regulatory effect on IFN signaling [132], possibly functioning as a feedback mechanism to limit excessive immune activation.

**Synthesis** Overall, IL-6 knockdown mitigates hyperinflammation and restores T cell and NK cytotoxic function despite lowering NK counts (as can be seen in Figure 6F,G), but at the cost of impaired cytokine support (type I IFN, GM-CSF, and G-CSF). TNF-$\alpha$ knockdown reduces inflammation but destabilizes macrophage control and suppresses NK activity. IFN-$\gamma$ knockdown worsens infection despite transient NK expansion. Together, these results suggest that therapeutic benefit lies not in complete suppression but in *targeted modulation*, particularly of IL-6 and TNF-$\alpha$, to balance inflammation control with preservation of antiviral immunity, consistent with clinical findings [11, 44, 45, 133].

## 4. Conclusions

In this study, we present a comprehensive within-host model of SARS-CoV-2 infection that highlights the pivotal roles of NK cells and cytokines, particularly IFN-$\gamma$ and TNF-$\alpha$, in shaping disease trajectories. Unlike previous models, ours incorporates specific immune cells and cytokines implicated in immune dysfunction and severe COVID-19 outcomes [35, 134]. By simulating their interactions, our framework provides insights into pathways that contribute both to successful viral clearance and to excessive inflammatory responses associated with acute lung injury and mortality. To our knowledge, this is the first attempt to primarily investigate key pathways of immune cell dysfunction, especially in the context of NK cells. By combining simulations, sensitivity analyses, and knockdown experiments, the model highlights the critical role of NK-cell function, the nuanced effects of IL-6 blockade, and the context-dependent impact of IFN-$\gamma$ and TNF-$\alpha$ signaling. These insights not only align with emerging clinical observations but also underscore the need for personalized and combinatorial therapeutic strategies.

Despite comparable NK-cell counts in mild and severe cases, severe COVID-19 is marked by functional NK-cell impairment, often driven by elevated IL-6 levels. Clinically, high IL-6 correlates with reduced granzyme A-expressing NK cells, reflecting suppressed cytotoxicity [30]. Our NK-cell knockdown simulations (Figure 5) recapitulated this, showing minimal effects on cytokine dynamics but a marked impairment in viral clearance. These findings reinforce the essential role of NK cells in early infection control and align with reports [33, 135] linking NK dysfunction to prolonged viral persistence and disease severity. Moreover, cytokines such as IL-6 and transforming growth factor-beta (TGF-$\beta$) exacerbate NK impairment by downregulating adhesion and cytotoxic functions [32], suggesting that therapeutic strategies to restore NK function, including IL-6 blockade, could enhance viral clearance and improve clinical outcomes.

Clinical trials of IL-6 inhibitors have produced mixed results. The WHO REACT meta-analysis of over 10,000 patients found that IL-6 receptor antagonists, when combined with glucocorticoids, reduced 28-day mortality, particularly in patients on noninvasive ventilation [136]. However, benefits were inconsistent in mechanically ventilated patients, and efficacy was contingent on concurrent glucocorticoid use, suggesting a synergistic rather than stand-alone role. Other studies (e.g., [137]) question IL-6 as a primary target, noting that levels in COVID-19 often fall below thresholds associated with efficacy in other inflammatory diseases. Potential risks, including secondary infections due to immunosuppression, further complicate its utility. This suggests that IL-6 blockade alone is insufficient but may contribute to benefit in well-selected patients, particularly in combination with glucocorticoids or janus kinase inhibitors (JAK) inhibitors [133]. Our findings highlight the importance of precision-medicine approaches and the use of biomarkers (e.g., serostatus [138]) to identify subgroups most likely to respond.

We also modeled the reported synergy between IFN-$\gamma$ and TNF-$\alpha$, which drives PANoptosis (i.e., programmed cell death) in macrophages [52]. Our multiplicative representation in the model yielded minimal synergistic effects, despite clinical observations of high TNF-$\alpha$, moderate IFN-$\gamma$, and elevated inflammatory macrophages [34, 118]. This discrepancy suggests that co-targeting TNF-$\alpha$ and IFN-$\gamma$ may not provide the anticipated therapeutic benefit, in line with clinical results in [52].

During severe COVID-19, IFN-$\gamma$ levels are difficult to quantify, with studies reporting both elevated and diminished concentrations [7, 34–36]. This uncertainty poses a challenge for modeling, as assumptions must be made regarding which IFN-$\gamma$ range best reflects severe disease. While our model cannot resolve exact concentrations, it illustrates how varying IFN-$\gamma$ levels influence immune dynamics. IFN-$\gamma$ knockdown simulations in severe cases (Figure 6) exacerbated T-cell lymphopenia, elevated TNF-$\alpha$ and IL-6, and worsened outcomes. These results suggest that IFN-$\gamma$ inhibition would likely be harmful, particularly in patients already exhibiting low IFN-$\gamma$ levels.

Conversely, clinical studies during the early pandemic highlighted potential therapeutic roles for IFN-$\gamma$ supplementation [139–141]. IFN-$\gamma$ treatment was reported to aid in the management of community-acquired infections and ventilator-associated pneumonia (VAP) in COVID-19 patients [140]. Interestingly, its efficacy appeared bidirectional: in one study, severely ill patients with immune deficiencies recovered following IFN-$\gamma$ administration [141], while another reported recovery in patients with hyper-inflammatory responses complicated by VAP [140]. In line with these reports, our simulations suggest that increasing IFN-$\gamma$ in mild cases promoted greater tissue protection and improved immune responses, indicating that moderate IFN-$\gamma$ supplementation could be beneficial. Further research is needed to determine whether there is a threshold above which IFN-$\gamma$ becomes pathogenic in severe COVID-19. Together, these findings suggest that IFN-$\gamma$ may be a broadly safe yet context-sensitive therapeutic option across diverse immunoprofiles.

Despite the complexity of our model and the breadth of results, this study has several limitations that should be addressed in future work. First, we note that our model emphasizes pro-inflammatory cytokines and immune responses associated with cytokine storm in COVID-19. While this focus enables detailed investigation of hyperinflammatory dynamics, it also makes the system toward exhibiting strong immune-mediated viral clearance, as can be seen in a slightly faster decay of viral load compared to the majority of patient data in Figure 2A. The absence of regulatory or anti-inflammatory mechanisms that temper immune killing likely contributes to the relatively rapid viral elimination observed in the model results. Incorporating such balancing pathways will likely

slow down the decay of viral load further and represents an important direction for future model refinement.

In addition, macrophage polarization was not explicitly modeled, although the M1 phenotype is closely linked to cytokines included in our framework such as IFN-$\gamma$, TNF-$\alpha$, and GM-CSF [142]. Future extensions could incorporate macrophage polarization and exogenous drivers such as IL-4, IL-10, IL-13, and TGF-$\beta$. Moreover, we modeled the innate immune response in unvaccinated individuals. Given widespread vaccination, future work should account for adaptive immunity, including B-cell and antibody dynamics, and examine how vaccination alters cytokine-driven pathways. Finally, we did not include TNF-$\alpha$–induced epithelial apoptosis, which some studies suggest may be significant [44]. Including these processes could further refine predictions of disease severity and therapeutic response.

## CRediT authorship contribution statement

**Keopagnapech Ngoun:** Conceptualization, Methodology, Validation, Formal analysis, Investigation, Software, Visualization, Writing - original draft, Writing - review & editing.
**Nicolas Alvarez:** Conceptualization, Methodology, Validation, Formal analysis, Investigation, Software, Visualization, Writing - original draft, Writing - review & editing.
**Ayesh Awad:** Conceptualization, Methodology, Validation, Investigation, Software, Visualization, Writing - review & editing.
**Hwayeon Ryu:** Conceptualization, Methodology, Validation, Formal analysis, Investigation, Software, Visualization, Writing - original draft, Writing - review & editing, Project administration, Funding acquisition.

## Acknowledgments

All authors were supported by the National Science Foundation under Grant No. DMS-2151990 (PI: Hwayeon Ryu). The research of Hwayeon Ryu was also supported by the Elon University Faculty Research and Development Full-Year, Full-Pay Sabbatical Award with Financial Assistance.

The authors thank Murilo Ferreira Lopes for his contributions to the early stages of model formulation and parameter estimation in this study.

## Conflict of interest

The authors declare that they have no known competing financial interests or personal relationships that could have appeared to influence the work reported in this paper.

## Data Availability

Matlab codes for parameter estimation and numerical simulation including knockdown experiments (Sections 2.3 and 3), and Matlab and R codes for local sensitivity analysis (shown in Section 3.2) are all available on the Github repository via https://github.com/kngoun/COVID_Lung_Immune_Model.git.

## Use of Generative-AI tools declaration

The authors declare that they used an artificial intelligence (AI) tool (ChatGPT 5.1) to check grammatical and spelling errors in Sections 1 and 4. The prompts included "correct grammatical and spelling errors". The authors reviewed and edited the generated output and take full responsibility for the final content.

## References


1. B. Zeng, L. Gao, Q. Zhou, K. Yu, F. Sun, Effectiveness of COVID-19 vaccines against SARS-CoV-2 variants of concern: A systematic review and meta-analysis, *BMC Med.*, **20** (2022), 200. https://doi.org/10.1186/s12916-022-02397-y
2. D. L. Farber, Tissues, not blood, are where immune cells function, *Nature*, **593** (2021), 506–509. https://doi.org/10.1038/d41586-021-01396-y
3. P. A. Szabo, P. Dogra, J. I. Gray, S. B. Wells, T. J. Connors, S. P. Weisberg, et al., Longitudinal profiling of respiratory and systemic immune responses reveals myeloid cell-driven lung inflammation in severe COVID-19, *Immunity*, **54** (2021), 797–814. https://doi.org/10.1016/j.immuni.2021.03.005
4. R. S. Thwaites, A. Uruchurtu, M. K. Siggins, F. Liew, C. D. Russell, S. C. Moore, et al., Inflammatory profiles across the spectrum of disease reveal a distinct role for GM-CSF in severe COVID-19, *Sci. Immunol.*, **6** (2021), eabg9873. https://doi.org/10.1126/sciimmunol.abg9873
5. C. Liu, A. J. Martins, W. W. Lau, N. Rachmaninoff, J. Chen, L. Imberti, et al., Time-resolved systems immunology reveals a late juncture linked to fatal COVID-19, *Cell*, **184** (2021), 1836–1857. https://doi.org/10.1016/j.cell.2021.02.018
6. B. Hu, S. Huang, L. Yin, The cytokine storm and COVID-19, *J. Med. Virol.*, **93** (2021), 250–256. https://doi.org/10.1002/jmv.26232
7. C. Huang, Y. Wang, X. Li, L. Ren, J. Zhao, Y. Hu, et al., Clinical features of patients infected with 2019 novel coronavirus in Wuhan, China, *The Lancet*, **395** (2020), 497–506. https://doi.org/10.1016/S0140-6736(20)30183-5
8. P. Mehta, D. F. McAuley, M. Brown, E. Sanchez, R. S. Tattersall, J. J. Manson, COVID-19: Consider cytokine storm syndromes and immunosuppression, *The Lancet*, **395** (2020), 1033–1034. https://doi.org/10.1016/S0140-6736(20)30628-0
9. R. J. Jose, A. Manuel, COVID-19 cytokine storm: The interplay between inflammation and coagulation, *Lancet Respir. Med.*, **8** (2020), e46–e47. https://doi.org/10.1016/S2213-2600(20)30216-2
10. A. Bahsoun, Y. Fakih, R. Zareef, F. Bitar, M. Arabi, Corticosteroids in COVID-19: Pros and cons, *Front. Med.*, **10** (2023), 1202504. https://doi.org/10.3389/fmed.2023.1202504
11. P. Du, J. Geng, F. Wang, X. Chen, Z. Huang, Y. Wang, Role of IL-6 inhibitor in treatment of COVID-19-related cytokine release syndrome, *Int. J. Med. Sci.*, **18** (2021), 1356. https://doi.org/10.7150/ijms.53564

12. R. Najjar-Debbiny, N. Gronich, G. Weber, J. Khoury, M. Amar, N. Stein, et al., Effectiveness of paxlovid in reducing severe coronavirus disease 2019 and mortality in high-risk patients, *Clin. Infect. Dis.*, **76** (2023), e342–e349. https://doi.org/10.1093/cid/ciac443

13. Z. Zhou, D. Li, Z. Zhao, S. Shi, J. Wu, J. Li, et al., Dynamical modelling of viral infection and cooperative immune protection in COVID-19 patients, *PLOS Comput. Biol.*, **19** (2023), e1011383. https://doi.org/10.1371/journal.pcbi.1011383

14. A. L. Jenner, R. A. Aogo, S. Alfonso, V. Crowe, X. Deng, A. P. Smith, et al., COVID-19 virtual patient cohort suggests immune mechanisms driving disease outcomes, *PLOS Pathog.*, **17** (2021), e1009753. https://doi.org/10.1371/journal.ppat.1009753

15. L. Fan, Z. Qiu, Q. Deng, T. Guo, L. Rong, Modeling SARS-CoV-2 infection dynamics: Insights into viral clearance and immune synergy, *Bull. Math. Biol.*, **87** (2025), 67. https://doi.org/10.1007/s11538-025-01442-0

16. A. Goyal, E. F. Cardozo-Ojeda, J. T. Schiffer, Potency and timing of antiviral therapy as determinants of duration of SARS-CoV-2 shedding and intensity of inflammatory response, *Sci. Adv.*, **6** (2020), eabc7112. https://doi.org/10.1126/sciadv.abc7112

17. M. Sadria, A. T. Layton, Modeling within-host SARS-CoV-2 infection dynamics and potential treatments, *Viruses*, **13** (2021), 1141. https://doi.org/10.3390/v13061141

18. A. Goyal, E. R. Duke, E. F. Cardozo-Ojeda, J. T. Schiffer, Modeling explains prolonged SARS-CoV-2 nasal shedding relative to lung shedding in remdesivir-treated rhesus macaques, *iScience*, **25** (2022), 104448. https://doi.org/10.1016/j.isci.2022.104448

19. B. Chatterjee, H. S. Sandhu, N. M. Dixit, Modeling recapitulates the heterogeneous outcomes of SARS-CoV-2 infection and quantifies the differences in the innate immune and CD8 T-cell responses between patients experiencing mild and severe symptoms, *PLOS Pathog.*, **18** (2022), e1010630. https://doi.org/10.1371/journal.ppat.1010630

20. N. Heitzman-Breen, S. M. Ciupe, Modeling within-host and aerosol dynamics of SARS-CoV-2: The relationship with infectiousness, *PLOS Comput. Biol.*, **18** (2022), e1009997. https://doi.org/10.1371/journal.pcbi.1009997

21. T. Song, Y. Wang, X. Gu, S. Qiao, Modeling the within-host dynamics of SARS-CoV-2 infection based on antiviral treatment, *Mathematics*, **11** (2023), 3485. https://doi.org/10.3390/math11163485

22. I. Al-Darabsah, K. L. Liao, S. Portet, A simple in-host model for COVID-19 with treatments: Model prediction and calibration, *J. Math. Biol.*, **86** (2023), 20. https://doi.org/10.1007/s00285-022-01849-6

23. C. Byrne, J. T. Schiffer, Ensemble modeling of SARS-CoV-2 immune dynamics in immunologically naïve rhesus macaques predicts that potent, early innate immune responses drive viral elimination, *Front. Immunol.*, **15** (2024), 1426016. https://doi.org/10.3389/fimmu.2024.1426016

24. L. Schuh, P. V. Markov, V. M. Veliov, N. I. Stilianakis, A mathematical model for the within-host (re)infection dynamics of SARS-CoV-2, *Math. Biosci.*, **371** (2024), 109178. https://doi.org/10.1016/j.mbs.2024.109178

25. R. Ke, C. Zitzmann, D. D. Ho, R. M. Ribeiro, A. S. Perelson, In vivo kinetics of SARS-CoV-2 infection and its relationship with a person's infectiousness, *Proc. Natl. Acad. Sci.*, **118** (2021), e2111477118. https://doi.org/10.1073/pnas.2111477118

26. R. Ke, P. P. Martinez, R. L. Smith, L. L. Gibson, A. Mirza, M. Conte, et al., Daily longitudinal sampling of SARS-CoV-2 infection reveals substantial heterogeneity in infectiousness, *Nat. Microbiol.*, **7** (2022), 640–652. https://doi.org/10.1038/s41564-022-01105-z

27. K. Owens, S. Esmaeili, J. T. Schiffer, Heterogeneous SARS-CoV-2 kinetics due to variable timing and intensity of immune responses, *JCI Insights*, **9** (2024), e176286. https://doi.org/10.1172/jci.insight.176286

28. I. Ghosh, Within host dynamics of SARS-CoV-2 in humans: Modeling immune responses and antiviral treatments, *SN Comput. Sci.*, **2** (2021), 482. https://doi.org/10.1007/s42979-021-00919-8

29. J. Li, J. Wu, J. Zhang, L. Tang, H. Mei, Y. Hu, et al., A multicompartment mathematical model based on host immunity for dissecting COVID-19 heterogeneity, *Heliyon*, **8** (2022), e09488. https://doi.org/10.1016/j.heliyon.2022.e09488

30. A. Mazzoni, L. Salvati, L. Maggi, M. Capone, A. Vanni, M. Spinicci, et al., Impaired immune cell cytotoxicity in severe COVID-19 is IL-6 dependent, *J. Clin. Invest.*, **130** (2020), 4694–4703. https://doi.org/10.1172/JCI138554

31. G. Leem, S. Cheon, H. Lee, S. J. Choi, S. Jeong, E. S. Kim, et al., Abnormality in the NK-cell population is prolonged in severe COVID-19 patients, *J. Allergy Clin. Immunol.*, **148** (2021), 996–1006. https://doi.org/10.1016/j.jaci.2021.07.022

32. J. Barros-Martins, R. Förster, B. Bošnjak, NK cell dysfunction in severe COVID-19: TGF-$\beta$-induced downregulation of integrin beta-2 restricts NK cell cytotoxicity, *Signal Transduction Targeted Ther.*, **7** (2022), 32. https://doi.org/10.1038/s41392-022-00892-5

33. J. Bi, NK cell dysfunction in patients with COVID-19, *Cell. Mol. Immunol.*, **19** (2022), 127–129. https://doi.org/10.1038/s41423-021-00825-2

34. Z. J. Hu, J. Xu, J. M. Yin, L. Li, W. Hou, L. L. Zhang, et al., Lower circulating interferon-gamma is a risk factor for lung fibrosis in COVID-19 patients, *Front. Immunol.*, **11** (2020), 585647. https://doi.org/10.3389/fimmu.2020.585647

35. J. Liu, S. Li, J. Liu, B. Liang, X. Wang, H. Wang, et al., Longitudinal characteristics of lymphocyte responses and cytokine profiles in the peripheral blood of SARS-CoV-2 infected patients, *EBioMedicine*, **55** (2020), 102763. https://doi.org/10.1016/j.ebiom.2020.102763

36. A. C. Gadotti, M. de Castro Deus, J. P. Telles, R. Wind, M. Goes, R. G. C. Ossoski, et al., IFN-$\gamma$ is an independent risk factor associated with mortality in patients with moderate and severe COVID-19 infection, *Virus Res.*, **289** (2020), 198171. https://doi.org/10.1016/j.virusres.2020.198171

37. S. Mansoor, A. R. Butt, A. Bibi, S. Mushtaq, I. Ullah, F. Alshahrani, et al., Expression of IFN-Gamma is significantly reduced during severity of COVID-19 infection in hospitalized patients, *PLOS ONE*, **18** (2023), e0291332. https://doi.org/10.1371/journal.pone.0291332

38. R. Savan, M. Gale, Innate immunity and interferon in SARS-CoV-2 infection outcome, *Immunity*, **56** (2023), 1443–1450. https://doi.org/10.1016/j.immuni.2023.06.018

39. S. M. Schumacher, S. V. Naga Prasad, Tumor necrosis factor-$\alpha$ in heart failure: An updated review, *Curr. cardiol. Rep.*, **20** (2018), 117. https://doi.org/10.1007/s11886-018-1067-7

40. H. Bruunsgaard, K. Andersen-Ranberg, J. v.B Hjelmborg, B. K. Pedersen, B. Jeune, Elevated levels of tumor necrosis factor alpha and mortality in centenarians, *Am. J. Med.*, **115** (2003), 278–283. https://doi.org/10.1016/s0002-9343(03)00329-2

41. D. I. Jang, A. H. Lee, H. Y. Shin, H. R. Song, J. H. Park, T. B. Kang, et al., The role of tumor necrosis factor alpha (TNF-$\alpha$) in autoimmune disease and current TNF-$\alpha$ inhibitors in therapeutics, *Int. J. Mol. Sci.*, **22** (2021), 2719. https://doi.org/10.3390/ijms22052719

42. W. H. Mahallawi, O. F. Khabour, Q. Zhang, H. M. Makhdoum. B. A. Suliman, MERS-CoV infection in humans is associated with a pro-inflammatory Th1 and Th17 cytokine profile, *Cytokine*, **104** (2018), 8–13. https://doi.org/10.1016/j.cyto.2018.01.025

43. B. Chen, C. Clark, T. Chou, Granulocyte/macrophage colony-stimulating factor stimulates monocyte and tissue macrophage proliferation and enhances their responsiveness to macrophage colony-stimulating factor, *Blood*, **71** (1988), 997–1002. https://doi.org/10.1182/blood.V71.4.997.997

44. Z. M. Zawawi, J. Kalyanasundram, R. M. Zain, R. Thayan, D. F. Basri, W. B. Yap, Prospective roles of tumor necrosis factor-alpha (TNF-$\alpha$) in COVID-19: Prognosis, therapeutic and management, *Int. J. Mol. Sci.*, **24** (2023), 6142. https://doi.org/10.3390/ijms24076142

45. Y. Guo, K. Hu, Y. Li, C. Lu, K. Ling, C. Cai, et al., Targeting TNF-$\alpha$ for COVID–19: Recent advanced and controversies, *Front. Public Health*, **10** (2022), 833967. https://doi.org/10.3389/fpubh.2022.833967

46. G. Kokkotis, K. Kitsou, I. Xynogalas, V. Spoulou, G. Magiorkinis, I. Trontzas, et al., Systematic review with meta-analysis: COVID-19 outcomes in patients receiving anti-TNF treatments, *Aliment. Pharmacol. Ther.*, **55** (2022), 154–167. https://doi.org/10.1111/apt.16717

47. A. J. Lee, A. A. Ashkar, The dual nature of type I and type II interferons, *Front. Immunol.*, **9** (2018), 2061. https://doi.org/10.3389/fimmu.2018.02061

48. H. Kelchtermans, A. Billiau, P. Matthys, How interferon-$\gamma$ keeps autoimmune diseases in check, *Trends Immunol.*, **29** (2008), 479–486. https://doi.org/10.1016/j.it.2008.07.002

49. The International Chronic Granulomatous Disease Cooperative Study Group, A controlled trial of interferon gamma to prevent infection in chronic granulomatous disease, *N. Engl. J. Med.*, **324** (1991), 509–516. https://doi.org/10.1056/NEJM199102213240801

50. A. Elyasi, I. Voloshyna, S. Ahmed, L. J. Kasselman, J. Behbodikhah, J. De Leon, et al., The role of interferon-$\gamma$ in cardiovascular disease: An update, *Inflammation Res.*, **69** (2020), 975–988. https://doi.org/10.1007/s00011-020-01382-6

51. B. Silva, P. A. Krogstad, R. M. Teles, P. R. Andrade, J. Rajfer, M. G. Ferrini, et al., IFN-$\gamma$-mediated control of SARS-CoV-2 infection through nitric oxide, *Front. Immunol.*, **14** (2023), 1284148. https://doi.org/10.3389/fimmu.2023.1284148

52. R. Karki, B. R. Sharma, S. Tuladhar, E. P. Williams, L. Zalduondo, P. Samir, et al., Synergism of TNF-$\alpha$ and IFN-$\gamma$ triggers inflammatory cell death, tissue damage, and mortality in SARS-CoV-2 infection and cytokine shock syndromes, *Cell*, **184** (2021), 149–168. https://doi.org/10.1016/j.cell.2020.11.025

53. N. Todorović-Raković, J. R. Whitfield, Between immunomodulation and immunotolerance: The role of IFN$\gamma$ in SARS-CoV-2 disease, *Cytokine*, **146** (2021), 155637. https://doi.org/10.1016/j.cyto.2021.155637

54. C. T. Ng, L. Y. Fong, M. N. H. Abdullah, Interferon-gamma (IFN-$\gamma$): Reviewing its mechanisms and signaling pathways on the regulation of endothelial barrier function, *Cytokine*, **166** (2023), 156208. https://doi.org/10.1016/j.cyto.2023.156208

55. C. van Eeden, L. Khan, M. S. Osman, J. W. C. Tervaert, Natural killer cell dysfunction and its role in COVID-19, *Int. J. Mol. Sci.*, **21** (2020), 6351. https://doi.org/10.3390/ijms21176351

56. M. H. Abdolvahab, S. Moradi-Kalbolandi, M. Zarei, D. Bose, K. Majidzadeh-A, L. Farahmand, Potential role of interferons in treating COVID-19 patients, *Int. Immunopharmacol.*, **90** (2021), 107171. https://doi.org/10.1016/j.intimp.2020.107171

57. A. J. Sadler, B. R. Williams, Interferon-inducible antiviral effectors, *Nat. Rev. Immunol.*, **8** (2008), 559–568. https://doi.org/10.1038/nri2314

58. M. R. Fernando, J. L. Reyes, J. Iannuzzi, G. Leung, D. M. McKay, The pro-inflammatory cytokine, interleukin-6, enhances the polarization of alternatively activated macrophages, *PLOS ONE*, **9** (2014), e94188. https://doi.org/10.1371/journal.pone.0094188

59. A. Dallagi, J. Girouard, J. Hamelin-Morrissette, R. Dadzie, L. Laurent, C. Vaillancourt, et al., The activating effect of IFN-$\gamma$ on monocytes/macrophages is regulated by the LIF–trophoblast–IL-10 axis via Stat1 inhibition and Stat3 activation, *Cell. Mol. Immunol.*, **12** (2015), 326–341. https://doi.org/10.1038/cmi.2014.50

60. P. Chomarat, J. Banchereau, J. Davoust, A. K. Palucka, IL-6 switches the differentiation of monocytes from dendritic cells to macrophages, *Nat. Immunol.*, **1** (2000), 510–514. https://doi.org/10.1038/82763

61. F. Colotta, F. Re, N. Polentarutti, S. Sozzan, A. Mantovani, Modulation of granulocyte survival and programmed cell death by cytokines and bacterial products, *Blood*, **80** (1992), 2012–20. https://doi.org/10.1182/blood.V80.8.2012.2012

62. B. Drescher, F. Bai, Neutrophil in viral infections, friend or foe, *Virus Res.*, **171** (2013), 1–7. https://doi.org/10.1016/j.virusres.2012.11.002

63. I. E. Galani, E. Andreakos, Neutrophils in viral infections: Current concepts and caveats, *J. Leucocyte Biol.*, **98** (2015), 557–564. https://doi.org/10.1189/jlb.4VMR1114-555R

64. S. L. Swain, K. K. McKinstry, T. M. Strutt, Expanding roles for CD4+ T cells in immunity to viruses, *Nat. Rev. Immunol.*, **12** (2012), 136–148. https://doi.org/10.1038/nri3152

65. M. Z. Tay, C. M. Poh, L. Rénia, P. A. MacAry, L. F. Ng, The trinity of COVID-19: Immunity, inflammation and intervention, *Nat. Rev. Immunol.*, **20** (2020), 363–374. https://doi.org/10.1038/s41577-020-0311-8

66. A. U. Haq, The effect of IFN-gamma and alpha on CON-A stimulated T-cell proliferation: Role of monocytes, *Am. J. Med. Sci.*, **292** (1986), 350–355. https://doi.org/10.1097/00000441-198612000-00003

67. V. J. Costela-Ruiz, R. Illescas-Montes, J. M. Puerta-Puerta, C. Ruiz, L. Melguizo-Rodríguez, SARS-CoV-2 infection: The role of cytokines in COVID-19 disease, *Cytokine Growth Factor Rev.*, **54** (2020), 62–75. https://doi.org/10.1016/j.cytogfr.2020.06.001

68. S. Meidaninikjeh, N. Sabouni, H. Z. Marzouni, S. Bengar, A. Khalili, R. Jafari, Monocytes and macrophages in COVID-19: Friends and foes, *Life Sci.*, **269** (2021), 119010. https://doi.org/10.1016/j.lfs.2020.119010

69. L. Vanderbeke, P. Van Mol, Y. Van Herck, F. De Smet, S. Humblet-Baron, K. Martinod, et al., Monocyte-driven atypical cytokine storm and aberrant neutrophil activation as key mediators of COVID-19 disease severity, *Nat. Commun.*, **12** (2021), 4117. https://doi.org/10.1038/s41467-021-24360-w

70. R. Morris, N. J. Kershaw, J. J. Babon, The molecular details of cytokine signaling via the JAK/STAT pathway, *Protein Sci.*, **27** (2018), 1984–2009. https://doi.org/10.1002/pro.3519

71. C. A. Janeway, P. Travers, M. Walport, M. J. Shlomchik, *Immunobiology: The Immune System in Health and Disease*, Garland Publishing, New York, USA, 2001.

72. M. Santillán, On the use of the Hill functions in mathematical models of gene regulatory networks, *Math. Modell. Nat. Phenom.*, **3** (2008), 85–97. https://doi.org/10.1051/mmnp:2008056

73. U. Nagarajan, Induction and function of IFN$\beta$ during viral and bacterial infection, *Crit. Rev. Immunol.*, **31** (2011), 459–474. https://doi.org/10.1615/critrevimmunol.v31.i6.20

74. K. Klöditz, B. Fadeel, Three cell deaths and a funeral: Macrophage clearance of cells undergoing distinct modes of cell death, *Cell Death Discovery*, **5** (2019), 65. https://doi.org/10.1038/s41420-019-0146-x

75. S. Elmore, Apoptosis: A review of programmed cell death, *Toxicol. Pathol.*, **35** (2007), 495–516. https://doi.org/10.1080/01926230701320337

76. P. Chomarat, C. Dantin, L. Bennett, J. Banchereau, A. K. Palucka, TNF skews monocyte differentiation from macrophages to dendritic cells, *J. Immunol.*, **171** (2003), 2262–2269. https://doi.org/10.4049/jimmunol.171.5.2262

77. S. Iwamoto, S. Iwai, K. Tsujiyama, C. Kurahashi, K. Takeshita, M. Naoe, et al., TNF-$\alpha$ drives human CD14+ monocytes to differentiate into CD70+ dendritic cells evoking Th1 and Th17 responses, *J. Immunol.*, **179** (2007), 1449–1457. https://doi.org/10.4049/jimmunol.179.3.1449

78. A. U. H. Khan, A. K. Ali, B. Marr, D. Jo, S. Ahmadvand, C. Fong-McMaster, et al., The TNF$\alpha$/TNFR2 axis mediates natural killer cell proliferation by promoting aerobic glycolysis, *Cell. Mol. Immunol.*, **20** (2023), 1140–1155. https://doi.org/10.1038/s41423-023-01071-4

79. T. Liu, J. Zhang, Y. Yang, H. Ma, Z. Li, J. Zhang, et al., The role of interleukin-6 in monitoring severe case of coronavirus disease 2019, *EMBO Mol. Med.*, **12** (2020), e12421. https://doi.org/10.15252/emmm.202012421

80. A. G. Laing, A. Lorenc, I. Del Molino Del Barrio, A. Das, M. Fish, L. Monin, et al., A dynamic COVID-19 immune signature includes associations with poor prognosis, *Nat. Med.*, **26** (2020), 1623–1635. https://doi.org/10.1038/s41591-020-1038-6

81. Z. Wang, H. Pan, B. Jiang, Type I IFN deficiency: An immunological characteristic of severe COVID-19 patients, *Signal Transduction Targeted Ther.*, **5** (2020), 198. https://doi.org/10.1038/s41392-020-00306-4

82. D. Acharya, G. Liu, M. U. Gack, Dysregulation of type I interferon responses in COVID-19, *Nat. Rev. Immunol.*, **20** (2020), 397–398. https://doi.org/10.1038/s41577-020-0346-x

83. Y. J. Kang, I. C. Jeung, A. Park, Y. J. Park, H. Jung, T. D. Kim, et al., An increased level of IL-6 suppresses NK cell activity in peritoneal fluid of patients with endometriosis via regulation of SHP-2 expression, *Hum. Reprod.*, **29** (2014), 2176–2189. https://doi.org/10.1093/humrep/deu172

84. M. Craig, A. R. Humphries, M. C. Mackey, A mathematical model of granulopoiesis incorporating the negative feedback dynamics and kinetics of G-CSF/neutrophil binding and internalization, *Bull. Math. Biol.*, **78** (2016), 2304–2357. https://doi.org/10.1007/s11538-016-0179-8

85. K. R. Martin, H. L. Wong, V. Witko-Sarsat, I. P. Wicks, G-CSF–a double edge sword in neutrophil mediated immunity, *Semin. Immunol.*, **54** (2021), 101516. https://doi.org/10.1016/j.smim.2021.101516

86. B. Rösler, S. Herold, Lung epithelial GM-CSF improves host defense function and epithelial repair in influenza virus pneumonia—a new therapeutic strategy, *Mol. Cell. Pediatr.*, **3** (2016), 29. https://doi.org/10.1186/s40348-016-0055-5

87. J. Scheller, A. Chalaris, D. Schmidt-Arras, S. Rose-John, The pro-and anti-inflammatory properties of the cytokine interleukin-6, *Biochim. Biophys. Acta (BBA)-Mol. Cell Res.*, **1813** (2011), 878–888. https://doi.org/10.1016/j.bbamcr.2011.01.034

88. R. Yang, Q. Zhao, J. Rao, F. Zeng, S. Yuan, M. Ji, et al., SARS-CoV-2 accessory protein ORF7b mediates tumor necrosis factor-$\alpha$-induced apoptosis in cells, *Front. Microbiol.*, **12** (2021), 654709. https://doi.org/10.3389/fmicb.2021.654709

89. Y. Shi, C. H. Liu, A. I. Roberts, J. Das, G. Xu, G. Ren, et al., Granulocyte-macrophage colony-stimulating factor (GM-CSF) and T-cell responses: What we do and don't know, *Cell Res.*, **16** (2006), 126–133. https://doi.org/10.1038/sj.cr.7310017

90. R. Channappanavar, A. R. Fehr, J. Zheng, C. Wohlford-Lenane, J. E. Abrahante, M. Mack, et al., IFN-I response timing relative to virus replication determines MERS coronavirus infection outcomes, *J. Clin. Invest.*, **129** (2019), 3625–3639. https://doi.org/10.1172/JCI126363

91. T. Sheahan, A. Sims, S. Leist, A. Schäfer, J. Won, A. J. Brown, et al., Comparative therapeutic efficacy of remdesivir and combination lopinavir, ritonavir, and interferon beta against MERS-CoV, *Nat. Commun.*, **11** (2020), 222. https://doi.org/10.1038/s41467-019-13940-6

92. Y. Zhao, L. Qin, P. Zhang, K. Li, L. Liang, J. Sun, et al., Longitudinal COVID-19 profiling associates IL-1RA and IL-10 with disease severity and RANTES with mild disease, *JCI Insights*, **5** (2020), e139834. https://doi.org/10.1172/jci.insight.139834

93. S. Trouillet-Assant, S. Viel, A. Gaymard, S. Pons, J. C. Richard, M. Perret, et al., Type I IFN immunoprofiling in COVID-19 patients, *J. Allergy Clin. Immunol.*, **146** (2020), 206–208. https://doi.org/10.1016/j.jaci.2020.04.029

94. K. Yin, M. J. Peluso, X. Luo, R. Thomas, M. G. Shin, J. Neidleman, et al., Long COVID manifests with T cell dysregulation, inflammation and an uncoordinated adaptive immune response to SARS-CoV-2, *Nat. Immunol.*, **25** (2024), 218–225. https://doi.org/10.1038/s41590-023-01724-6

95. A. Goyal, E. F. Cardozo-Ojeda, J. T. Schiffer, Potency and timing of antiviral therapy as determinants of duration of SARS-CoV-2 shedding and intensity of inflammatory response, *Sci. Adv.*, **6** (2020), eabc7112. https://doi.org/10.1126/sciadv.abc7112

96. B. E. Young, S. W. X. Ong, S. Kalimuddin, J. G. Low, S. Y. Tan, J. Loh, et al., Epidemiologic features and clinical course of patients infected with SARS-CoV-2 in singapore, *JAMA*, **323** (2020), 1488–1494. https://doi.org/10.1001/jama.2020.3204

97. R. Wölfel, V. M. Corman, W. Guggemos, M. Seilmaier, S. Zange, M. A. Müller, et al., Virological assessment of hospitalized patients with COVID-2019, *Nature*, **581** (2020), 465–469. https://doi.org/10.1038/s41586-020-2196-x

98. O. J. McElvaney, N. L. McEvoy, O. F. McElvaney, T. P. Carroll, M. P. Murphy, D. M. Dunlea, et al., Characterization of the inflammatory response to severe COVID-19 illness, *Am. J. Respir. Crit. Care Med.*, **202** (2020), 812–821. https://doi.org/10.1164/rccm.202005-1583OC

99. M. Sa Ribero, N. Jouvenet, M. Dreux, S. Nisole, Interplay between SARS-CoV-2 and the type I interferon response, *PLOS Pathog.*, **16** (2020), e1008737. https://doi.org/10.1371/journal.ppat.1008737

100. C. Maucourant, I. Filipovic, A. Ponzetta, S. Aleman, M. Cornillet, L. Hertwig, et al., Natural killer cell immunotypes related to COVID-19 disease severity, *Sci. Immunol.*, **5** (2020), eabd6832. https://doi.org/10.1126/sciimmunol.abd6832

101. E. Andreakos, C. H. G. Effort, Type I and type III interferons: From basic biology and genetics to clinical development for COVID-19 and beyond, *Semin. Immunol.*, **72** (2024), 101863. https://doi.org/10.1016/j.smim.2024.101863

102. M. M. Islam, S. Islam, R. Ahmed, M. Majumder, B. Sarkar, M. E. R. Himu, et al., Reduced IFN-$\gamma$ levels along with changes in hematologic and immunologic parameters are key to COVID-19 severity in bangladeshi patients, *Exp. Hematol.*, **118** (2023), 53–64. https://doi.org/10.1016/j.exphem.2022.11.006

103. T. Herold, V. Jurinovic, C. Arnreich, B. J. Lipworth, J. C. Hellmuth, M. von Bergwelt-Baildon, et al., Elevated levels of IL-6 and CRP predict the need for mechanical ventilation in COVID-19, *J. Allergy Clin. Immunol.*, **146** (2020), 128–136. https://doi.org/10.1016/j.jaci.2020.05.008

104. W. Hafez, P. Nasa, A. Khairy, M. Jose, M. Abdelshakour, S. Ahmed, et al., Interleukin-6 and the determinants of severe COVID-19: A retrospective cohort study, *Medicine*, **102** (2023), e36037. https://doi.org/10.1097/MD.0000000000036037

105. Q. X. Long, X. J. Tang, Q. L. Shi, Q. Li, H. J. Deng, J. Yuan, et al., Clinical and immunological assessment of asymptomatic SARS-CoV-2 infections, *Nat. Med.*, **26** (2020), 1200–1204. https://doi.org/10.1038/s41591-020-0965-6

106. A. Mohamed, S. Zavoshi, R. Mahmood, H. Gidda, The impact of granulocyte colony-stimulating factor administration in a neutropenic cancer patient with COVID-19-related acute respiratory distress syndrome, *Cureus*, **15** (2023), e35399. https://doi.org/10.7759/cureus.35399

107. A. E. Curtis, T. A. Smith, B. A. Ziganshin, J. A. Elefteriades, The mystery of the Z-score, *Aorta*, **4** (2016), 124–130. https://doi.org/10.12945/j.aorta.2016.16.014

108. E. Brunet-Ratnasingham, S. Morin, H. Randolph, M. Labrecque, J. Bélair, R. Lima-Barbosa, et al., Sustained IFN signaling is associated with delayed development of SARS-CoV-2-specific immunity, *Nat.Commun.*, **15** (2024), 4177. https://doi.org/10.1038/s41467-024-48556-y

109. S. Sunder, R. Jayaraman, H. S. Mahapatra, S. Sathi, V. Ramanan, P. Kanchi, et al., Estimation of renal function in the intensive care unit: The covert concepts brought to light, *J. Intensive Care*, **2** (2014), 31. https://doi.org/10.1186/2052-0492-2-31

110. S. Petrov, H. Taskov, M. Murdjeva, Guardians of immunity: NK cell-mediated defense in COVID-19 and post-COVID scenarios, *Folia Med.*, **66** (2024), 12–18. https://doi.org/10.3897/folmed.66.e113356

111. Y. Nishikawa, K. Yamaguchi, M. A. Shofiudin, M. Mimura, M. Takata, S. Mihara, et al., Distinct immunity dynamics of natural killer cells in mild and moderate COVID-19 cases during the Omicron variant phase, *Front. Immunol.*, **16** (2025), 1594296. https://doi.org/10.3389/fimmu.2025.1594296

112. E. O. Gubernatorova, E. A. Gorshkova, A. Polinova, M. Drutskaya, IL-6: Relevance for immunopathology of SARS-CoV-2, *Cytokine Growth Factor Rev.*, **53** (2020), 13–24. https://doi.org/10.1016/j.cytogfr.2020.05.009

113. T. Nawar, S. Morjaria, A. Kaltsas, D. Patel, R. Perez-Johnston, A. F. Daniyan, et al., Granulocyte-colony stimulating factor in COVID-19: Is it stimulating more than just the bone marrow, *Am. J. Hematol.*, **95** (2020), E210. https://doi.org/10.1002/ajh.25870

114. J. F. Bermejo-Martin, R. Almansa, A. P. Tedim, A. de la Fuente, J. M. Eiros, A. Torres, et al., Mounting evidence of impaired viral control in severe COVID-19, *Lancet Microbe*, **2** (2021), e228–e229. https://doi.org/10.1016/S2666-5247(21)00084-7

115. J. Yang, L. Zhang, C. Yu, X. F. Yang, H. Wang, Monocyte and macrophage differentiation: Circulation inflammatory monocyte as biomarker for inflammatory diseases, *Biomarker Res.*, **2** (2014), 1–9. https://doi.org/10.1186/2050-7771-2-1

116. M. M. Dunagan, N. Dábilla, C. McNinch, J. M. Brenchley, P. T. Dolan, J. M. Fox, Activating fc$\gamma$rs on monocytes are necessary for optimal mayaro virus clearance, *bioRxiv*. https://doi.org/10.1101/2024.07.23.604823

117. A. Banete, J. Barilo, R. Whittaker, S. Basta, The activated macrophage–a tough fortress for virus invasion: How viruses strike back, *Front. Microbiol.*, **12** (2022), 803427. https://doi.org/10.3389/fmicb.2021.803427

118. J. Li, R. Shan, H. Miller, A. Filatov, M. G. Byazrova, L. Yang, et al., The roles of macrophages and monocytes in COVID-19 severe respiratory syndrome, *Cell Insights*, **2** (2025), 100250. https://doi.org/10.1016/j.cellin.2025.100250

119.M. J. Lee, C. A. Blish, Defining the role of natural killer cells in COVID-19, *Nat. Immunol.*, **24** (2023), 1628–1638. https://doi.org/10.1038/s41590-023-01560-8

120.J. Majidpoor, K. Mortezaee, Interleukin-6 in SARS-CoV-2 induced disease: Interactions and therapeutic applications, *Biomed. Pharmacother.*, **145** (2022), 112419. https://doi.org/10.1016/j.biopha.2021.112419

121.S. Zhang, B. Asquith, R. Szydlo, J. S. Tregoning, K. M. Pollock, Peripheral T cell lymphopenia in COVID-19: Potential mechanisms and impact, *Immunother. Adv.*, **1** (2021), ltab015. https://doi.org/10.1093/immadv/ltab015

122.B. Li, L. L. Jones, T. L. Geiger, IL-6 promotes T cell proliferation and expansion under inflammatory conditions in association with low-level ROR$\gamma$t expression, *J. Immunol.*, **201** (2018), 2934–2946. https://doi.org/10.4049/jimmunol.1800016

123.L. Velazquez-Salinas, A. Verdugo-Rodriguez, L. L. Rodriguez, M. V. Borca, The role of interleukin 6 during viral infections, *Front. Microbiol.*, **10** (2019), 1057. https://doi.org/10.3389/fmicb.2019.01057

124.F. Rollwagen, T. Davis, Y. Y. Li, N. Pacheco, X. L. Zhu, Orally administered IL-6 induces elevated intestinal GM-CSF gene expression and splenic CFU-GM, *Cytokine*, **27** (2004), 107–112. https://doi.org/10.1016/j.cyto.2004.03.019

125.T. Hartung, Anti-inflammatory effects of granulocyte colony-stimulating factor, *Curr. Opin. Hematol.*, **5** (1998), 221–225. https://doi.org/10.1097/00062752-199805000-00013

126.M. Kohanawa, A regulatory effect of the balance between TNF-$\alpha$ and IL-6 in the granulomatous and inflammatory response to Rhodococcus aurantiacus infection in mice, *J. Immunol.*, **177** (2006), 642–650. https://doi.org/10.4049/jimmunol.177.1.642

127.M. G. Dorrington, I. D. Fraser, NF-$\kappa$B signaling in macrophages: Dynamics, crosstalk, and signal integration, *Front. Immunol.*, **10** (2019), 705. https://doi.org/10.3389/fimmu.2019.00705

128.T. Ota, K. Takeda, H. Akiba, Y. Hayakawa, K. Ogasawara, Y. Ikarashi, et al., IFN-$\gamma$–mediated negative feedback regulation of NKT-cell function by CD94/NKG2, *Blood*, **106** (2005), 184–192. https://doi.org/10.1182/blood-2004-11-4257

129.S. P. Templeton, S. Perlman, Role of IFN-$\gamma$ responsiveness in CD8 T cell-mediated viral clearance and demyelination in coronavirus-infected mice, *J. Neuroimmunol.*, **194** (2008), 18–26. https://doi.org/10.1016/j.jneuroim.2007.10.030

130.P. Bhat, G. Leggatt, N. Waterhouse, I. H. Frazer, Interferon-$\gamma$ derived from cytotoxic lymphocytes directly enhances their motility and cytotoxicity, *Cell Death Dis.*, **8** (2017), e2836–e2836. https://doi.org/10.1038/cddis.2017.67

131.N. Parameswaran, S. Patial, Tumor necrosis factor-$\alpha$ signaling in macrophages, *Crit. Rev. Eukaryotic Gene Expression*, **20** (2010), 87–103. https://doi.org/10.1615/critreveukargeneexpr.v20.i2.10

132.T. Cantaert, D. Baeten, P. P. Tak, L. G. van Baarsen, Type I IFN and TNF$\alpha$ cross-regulation in immune-mediated inflammatory disease: Basic concepts and clinical relevance, *Arthritis Res. Ther.*, **12** (2010), 219. https://doi.org/10.1186/ar3150

133.F. L. van de Veerdonk, E. Giamarellos-Bourboulis, P. Pickkers, L. Derde, H. Leavis, R. van Crevel, et al., A guide to immunotherapy for COVID-19, *Nat. Med.*, **28** (2022), 39–50. https://doi.org/10.1038/s41591-021-01643-9

134.D. M. Del Valle, S. Kim-Schulze, H. H. Huang, N. D. Beckmann, S. Nirenberg, B. Wang, et al., An inflammatory cytokine signature predicts COVID-19 severity and survival, *Nat. Med.*, **26** (2020), 1636–1643. https://doi.org/10.1038/s41591-020-1051-9

135.T. Tsao, A. M. Buck, L. Grimbert, B. H. LaFranchi, B. A. Poblano, E. A. Fehrman, et al., Long COVID is associated with lower percentages of mature, cytotoxic nk cell phenotypes, *J. Clin. Invest.*, **135** (2024). https://doi.org/10.1172/JCI188182

136.M. A. Matthay, A. F. Luetkemeyer, IL-6 receptor antagonist therapy for patients hospitalized for COVID-19: Who, when, and how, *JAMA*, **326** (2021), 483–485. https://doi.org/10.1001/jama.2021.11121

137.S. Scherger, A. Henao-Martínez, C. Franco-Paredes, L. Shapiro, Rethinking interleukin-6 blockade for treatment of COVID-19, *Med. Hypotheses*, **144** (2020), 110053. https://doi.org/10.1016/j.mehy.2020.110053

138.J. Aguareles, C. Forné, A. García-Casas, G. Santamaría-Corral, D. Carnevali-Ruiz, G. Sotres-Fernández, et al., Influence of anti-spike protein antibody levels on tocilizumab efficacy in hospitalized patients with severe COVID-19 pneumonia: A post-hoc analysis of the COVACTA trial, *BMC Infect. Dis.*, **25** (2025), 1–9. https://doi.org/10.1186/s12879-025-11001-6

139.A. Myasnikov, S. Berns, P. Talyzin, F. Ershov, Interferon gamma in the treatment of patients with moderate COVID-19, *Probl. Virol.*, **66** (2021), 47–54. https://doi.org/10.36233/0507-4088-24

140.L. S. Nguyen, Z. Ait Hamou, N. Gastli, N. Chapuis, F. Pène, Potential role for interferon gamma in the treatment of recurrent ventilator-acquired pneumonia in patients with COVID-19: A hypothesis, *Intensive Care Med.*, **47** (2021), 619–621. https://doi.org/10.1007/s00134-021-06377-3

141.A. van Laarhoven, L. Kurver, G. J. Overheul, E. J. Kooistra, W. F. Abdo, R. van Crevel, et al., Interferon gamma immunotherapy in five critically ill COVID-19 patients with impaired cellular immunity: A case series, *Med*, **2** (2021), 1163–1170. https://doi.org/10.1016/j.medj.2021.09.003

142.A. Sica, M. Erreni, P. Allavena, C. Porta, Macrophage polarization in pathology, *Cell. Mol. Life Sci.*, **72** (2015), 4111–4126. https://doi.org/10.1007/s00018-015-1995-y

143.K. S. Kim, K. Ejima, S. Iwanami, Y. Fujita, H. Ohashi, Y. Koizumi, et al., A quantitative model used to compare within-host SARS-CoV-2, MERS-CoV, and SARS-CoV dynamics provides insights into the pathogenesis and treatment of SARS-CoV-2, *PLOS Biol.*, **19** (2021), e3001128. https://doi.org/10.1371/journal.pbio.3001128

144.J. D. Crapo, B. E. Barry, P. Gehr, M. Bachofen, E. R. Weibel, Cell number and cell characteristics of the normal human lung, *Am. Rev. Respir. Dis.*, **126** (1982), 332–337. https://doi.org/10.1164/arrd.1982.126.2.332

145.J. Armstrong, E. Gluck, R. Crapo, H. A. Jones, J. Hughes, Lung tissue volume estimated by simultaneous radiographic and helium dilution methods, *Thorax*, **37** (1982), 676–679. https://doi.org/10.1136/thx.37.9.676

146.N. Chaffey, Alberts, B., Johnson, A., Lewis, J., Raff, M., Roberts, K. and Walter, P. Molecular biology of the cell. 4th edn., *Ann. Bot.*, **91** (2003), 401–401. https://doi.org/10.1093/aob/mcg023

147.W. Jiang, L. Kang, H. Z. Lu, X. Pan, Q. Lin, Q. Pan, et al., Normal values for CD4 and CD8 lymphocyte subsets in healthy Chinese adults from Shanghai, *Clin. Vaccine Immunol.*, **11** (2004), 811–813. https://doi.org/10.1128/CDLI.11.4.811-813.2004

148.C. L. Gordon, M. Miron, J. J. Thome, N. Matsuoka, J. Weiner, M. A. Rak, et al., Tissue reservoirs of antiviral T cell immunity in persistent human CMV infection, *J. Exp. Med.*, **214** (2017), 651–667. https://doi.org/10.1084/jem.20160758

149.F. Bozzano, C. Perrone, L. Moretta, A. De Maria, NK cell precursors in human bone marrow in health and inflammation, *Front. Immunol.*, **10** (2019), 2045. https://doi.org/10.3389/fimmu.2019.02045

150.M. Osman, R. M. Faridi, W. Sligl, M. T. Shabani-Rad, P. Dharmani-Khan, A. Parker, et al., Impaired natural killer cell counts and cytolytic activity in patients with severe COVID-19, *Blood Adv.*, **4** (2020), 5035–5039. https://doi.org/10.1182/bloodadvances.2020002650

151.M. Maes, A. Lin, L. Delmeire, A. Van Gastel, G. Kenis, R. De Jongh, et al., Elevated serum interleukin-6 (IL-6) and IL-6 receptor concentrations in posttraumatic stress disorder following accidental man-made traumatic events, *Biol. Psychiatry*, **45** (1999), 833–839. https://doi.org/10.1016/s0006-3223(98)00131-0

152.J. Lee, Y. Kim, J. Lim, M. Kim, K. Han, G-CSF and GM-CSF concentrations and receptor expression in peripheral blood leukemic cells from patients with chronic myelogenous leukemia, *Ann. Clin. Lab. Sci.*, **38** (2008), 331–337.

153.K. Suzuki, M. Yamada, S. Kurakake, N. Okamura, K. Yamaya, Q. Liu, et al., Circulating cytokines and hormones with immunosuppressive but neutrophil-priming potentials rise after endurance exercise in humans, *Eur. J. Appl. Physiol.*, **81** (2000), 281–287. https://doi.org/10.1007/s004210050044

154.N. O. Kurtovic, E. K. Halilovic, Serum concentrations of interferon gamma (IFN-$\gamma$) in patients with psoriasis: Correlation with clinical type and severity of the disease, *Med. Arch.*, **72** (2018), 410. https://doi.org/10.5455/medarh.2018.72.410-413

155.S. R. Kapadia, K. Yakoob, S. Nader, J. D. Thomas, D. L. Mann, B. P. Griffin, Elevated circulating levels of serum tumor necrosis factor-alpha in patients with hemodynamically significant pressure and volume overload, *J. Am. Coll. Cardiol.*, **36** (2000), 208–212. https://doi.org/10.1016/s0735-1097(00)00721-x

156.I. Ioannidis, F. Ye, B. McNally, M. Willette, E. Flaño, Toll-like receptor expression and induction of type I and type III interferons in primary airway epithelial cells, *J. Virol.*, **87** (2013), 3261–3270. https://doi.org/10.1128/JVI.01956-12

157.Y. Jamilloux, T. Henry, A. Belot, S. Viel, M. Fauter, T. El Jammal, et al., Should we stimulate or suppress immune responses in COVID-19? Cytokine and anti-cytokine interventions, *Autoimmun. Rev.*, **19** (2020), 102567. https://doi.org/10.1016/j.autrev.2020.102567

158.L. M. Carlin, K. Yanagi, A. Verhoef, E. N. N. Hoen, J. Yates, L. Gardner, et al., Secretion of IFN-$\gamma$ and not IL-2 by anergic human T cells correlates with assembly of an immature immune synapse, *Blood*, **106** (2005), 3874–3879. https://doi.org/10.1182/blood-2005-03-0996

159.O. Lawal, H. Knobel, H. Weda, L. D. Bos, T. M. Nijsen, R. Goodacre, et al., Volatile organic compound signature from co-culture of lung epithelial cell line with pseudomonas aeruginosa, *Analyst*, **143** (2018), 3148–3155. https://doi.org/10.1039/c8an00759d

160.L. Landsman, S. Jung, Lung macrophages serve as obligatory intermediate between blood monocytes and alveolar macrophages, *J. Immunol.*, **179** (2007), 3488–3494. https://doi.org/10.4049/jimmunol.179.6.3488

161.M. L. Ng, S. H. Tan, E. E. See, E. E. Ooi, A. E. Ling, Proliferative growth of SARS coronavirus in vero E6 cells, *J. Gen. Virol.*, **84** (2003), 3291–3303. https://doi.org/10.1099/vir.0.19505-0

162.A. M. Knaapen, F. Seiler, P. A. Schilderman, P. Nehls, J. Bruch, R. P. Schins, et al., Neutrophils cause oxidative DNA damage in alveolar epithelial cells, *Free Radical Biol. Med.*, **27** (1999), 234–240. https://doi.org/10.1016/S0891-5849(98)00285-8

163.C. Nathan, Neutrophils and COVID-19: Nots, nets, and knots, *J. Exp. Med.*, **217** (2020), e20201439. https://doi.org/10.1084/jem.20201439

164.D. Mathew, J. R. Giles, A. E. Baxter, D. A. Oldridge, A. R. Greenplate, J. E. Wu, et al., Deep immune profiling of COVID-19 patients reveals distinct immunotypes with therapeutic implications, *Science*, **369** (2020), eabc8511. https://doi.org/10.1126/science.abc8511

165.J. K. Whitmire, J. T. Tan, J. L. Whitton, Interferon-$\gamma$ acts directly on CD8+ T cells to increase their abundance during virus infection, *J. Exp. Med.*, **201** (2005), 1053–1059. https://doi.org/10.1084/jem.20041463

166.N. Zhang, M. J. Bevan, CD8+ T cells: Foot soldiers of the immune system, *Immunity*, **35** (2011), 161–168. https://doi.org/10.1016/j.immuni.2011.07.010

167.S. Baral, R. Antia, N. M. Dixit, A dynamical motif comprising the interactions between antigens and CD8 T cells may underlie the outcomes of viral infections, *Proc. Natl. Acad. Sci.*, **116** (2019), 17393–17398. https://doi.org/10.1073/pnas.1902178116

168.T. Cassidy, A. R. Humphries, M. Craig, M. C. Mackey, Characterizing chemotherapy-induced neutropenia and monocytopenia through mathematical modelling, *Bull. Math. Biol.*, **82** (2020), 1–26. https://doi.org/10.1007/s11538-020-00777-0

169.B. Sainz Jr, E. C. Mossel, C. Peters, R. F. Garry, Interferon-beta and interferon-gamma synergistically inhibit the replication of severe acute respiratory syndrome-associated coronavirus (SARS-CoV), *Virology*, **329** (2004), 11–17. https://doi.org/10.1016/j.virol.2004.08.011

170.L. Sun, J. Rautela, R. B. Delconte, F. Souza-Fonseca-Guimaraes, E. M. Carrington, R. L. Schenk, et al., GM-CSF quantity has a selective effect on granulocytic vs. monocytic myeloid development and function, *Front. Immunol.*, **9** (2018), 1922. https://doi.org/10.3389/fimmu.2018.01922

171.M. F. Krummel, J. N. Mahale, L. F. Uhl, E. A. Hardison, A. M. Mujal, J. M. Mazet, et al., Paracrine costimulation of IFN-$\gamma$ signaling by integrins modulates CD8 T cell differentiation, *Proc. Natl. Acad. Sci.*, **115** (2018), 11585–11590. https://doi.org/10.1073/pnas.1804556115

172.M. A. Holsti, J. McArthur, J. P. Allison, D. H. Raulet, Role of IL-6, IL-1, and CD28 signaling in responses of mouse CD4+ T cells to immobilized anti-TCR monoclonal antibody, *J. Immunol.*, **152** (1994), 1618–1628. https://doi.org/10.4049/jimmunol.152.4.1618

173. A. P. Smith, D. J. Moquin, V. Bernhauerova, A. M. Smith, Influenza virus infection model with density dependence supports biphasic viral decay, *Front. Microbiol.*, **9** (2018), 1554. https://doi.org/10.3389/fmicb.2018.01554

174. B. Vanherberghen, P. E. Olofsson, E. Forslund, M. Sternberg-Simon, M. A. Khorshidi, S. Pacouret, et al., Classification of human natural killer cells based on migration behavior and cytotoxic response, *Blood, J. Am. Soc. Hematol.*, **121** (2013), 1326–1334. https://doi.org/10.1182/blood-2012-06-439851

175. M. Ardolino, A. Zingoni, C. Cerboni, F. Cecere, A. Soriani, M. L. Iannitto, et al., DNAM-1 ligand expression on Ag-stimulated T lymphocytes is mediated by ROS-dependent activation of DNA-damage response: Relevance for NK-T cell interaction, *Blood, J. Am. Soc. Hematol.*, **117** (2011), 4778–4786. https://doi.org/10.1182/blood-2010-08-300954

176. R. C. Rigden, C. P. Carrasco, A. Summerfield, K. C. MCCullough, Macrophage phagocytosis of foot-and-mouth disease virus may create infectious carriers, *Immunology*, **106** (2002), 537–548. https://doi.org/10.1046/j.1365-2567.2002.01460.x

177. P. Smith, S. Z. Wang, K. Dowling, K. Forsyth, Leucocyte populations in respiratory syncytial virus-induced bronchiolitis, *J. Paediatr. Child Health*, **37** (2001), 146–151. https://doi.org/10.1046/j.1440-1754.2001.00618.x

178. H. Y. Lee, D. J. Topham, S. Y. Park, J. Hollenbaugh, J. Treanor, T. R. Mosmann, et al., Simulation and prediction of the adaptive immune response to influenza a virus infection, *J. Virol.*, **83** (2009), 7151–7165. https://doi.org/10.1128/JVI.00098-09

179. C. S. Zent, M. R. Elliott, Maxed out macs: Physiologic cell clearance as a function of macrophage phagocytic capacity, *The FEBS J.*, **284** (2017), 1021–1039. https://doi.org/10.1111/febs.13961

180. E. A. Hernandez-Vargas, J. X. Velasco-Hernandez, In-host mathematical modelling of COVID-19 in humans, *Annu. Rev. Control*, **50** (2020), 448–456. https://doi.org/10.1016/j.arcontrol.2020.09.006

181. F. Ginhoux, M. Guilliams, Tissue-resident macrophage ontogeny and homeostasis, *Immunity*, **44** (2016), 439–449. https://doi.org/10.1016/j.immuni.2016.02.024

182. R. Eftimie, G. Eftimie, Tumour-associated macrophages and oncolytic virotherapies: A mathematical investigation into a complex dynamics, *Lett. Biomath.*, **5** (2018), S6–S35. https://doi.org/10.1007/s10238-024-01443-8

183. A. A. Patel, Y. Zhang, J. N. Fullerton, L. Boelen, A. Rongvaux, A. A. Maini, et al., The fate and lifespan of human monocyte subsets in steady state and systemic inflammation, *J. Exp. Med.*, **214** (2017), 1913–1923. https://doi.org/10.1084/jem.20170355

184. P. S. Kim, P. P. Lee, D. Levy, Modeling regulation mechanisms in the immune system, *J. Theor. Biol.*, **246** (2007), 33–69. https://doi.org/10.1016/j.jtbi.2006.12.012

185. C. T. Lutz, A. Karapetyan, A. Al-Attar, B. J. Shelton, K. J. Holt, J. H. Tucker, et al., Human NK cells proliferate and die in vivo more rapidly than T cells in healthy young and elderly adults, *J. Immunol.*, **186** (2011), 4590–4598. https://doi.org/10.4049/jimmunol.1002732

186.S. Ye, S. Lowther, J. Stambas, Inhibition of reactive oxygen species production ameliorates inflammation induced by influenza a viruses via upregulation of SOCS1 and SOCS3, *J. Virol.*, **89** (2015), 2672–2683. https://doi.org/10.1128/JVI.03529-14

187.Y. Shibata, P. Y. Berclaz, Z. C. Chroneos, M. Yoshida, J. A. Whitsett, B. C. Trapnell, GM-CSF regulates alveolar macrophage differentiation and innate immunity in the lung through PU. 1, *Immunity*, **15** (2001), 557–567. https://doi.org/10.1016/s1074-7613(01)00218-7

188.M. R. Alderson, T. W. Tough, S. F. Ziegler, K. H. Grabstein, Interleukin 7 induces cytokine secretion and tumoricidal activity by human peripheral blood monocytes, *J. Exp. Med.*, **173** (1991), 923–930. https://doi.org/10.1084/jem.173.4.923

189.M. Hallsworth, C. Soh, S. Lane, J. Arm, T. Lee, Selective enhancement of GM-CSF, TNF-alpha, IL-1 beta and IL-8 production by monocytes and macrophages of asthmatic subjects, *Eur. Respir. J.*, **7** (1994), 1096–1102. https://doi.org/10.1183/09031936.94.07061096

190.M. T. Lee, K. Kaushansky, P. Ralph, M. B. Ladner, Differential expression of M-CSF, G-CSF, and GM-CSF by human monocytes, *J. Leukocyte Biol.*, **47** (1990), 275–282. https://doi.org/10.1002/jlb.47.3.275

191.M. Ohta, T. Okabe, K. Ozawa, A. Urabe, F. Takaku, 1$\alpha$, 25-Dihydroxy vitamin D3 (calcitriol) stimulates proliferation of human circulating monocytes in vitro, *FEBS Lett.*, **185** (1985), 9–13. https://doi.org/10.1016/0014-5793(85)80730-4

192.L. R. Krilov, R. M. Hendry, E. Godfrey, K. McIntosh, Respiratory virus infection of peripheral blood monocytes: Correlation with ageing of cells and interferon production in vitro, *J. Gen. Virol.*, **68** (1987), 1749–1753. https://doi.org/10.1099/0022-1317-68-6-1749

193.C. Fauriat, E. O. Long, H. G. Ljunggren, Y. T. Bryceson, Regulation of human NK-cell cytokine and chemokine production by target cell recognition, *Blood, J. Am. Soc. Hematol.*, **115** (2010), 2167–2176. https://doi.org/10.1182/blood-2009-08-238469

194.H. Aung, Z. Toossi, J. J. Wisnieski, R. S. Wallis, L. A. Culp, N. B. Phillips, et al., Induction of monocyte expression of tumor necrosis factor alpha by the 30-kD alpha antigen of Mycobacterium tuberculosis and synergism with fibronectin, *J. Clin. Invest.*, **98** (1996), 1261–1268. https://doi.org/10.1172/JCI118910

195.C. Timmerman, E. Mattsson, L. Martinez-Martinez, L. De Graaf, J. Van Strijp, H. Verbrugh, et al., Induction of release of tumor necrosis factor from human monocytes by staphylococci and staphylococcal peptidoglycans, *Infect. Immun.*, **61** (1993), 4167–4172. https://doi.org/10.1128/iai.61.10.4167-4172.1993

196.C. M. Freeman, M. K. Han, F. J. Martinez, S. Murray, L. X. Liu, S. W. Chensue, et al., Cytotoxic potential of lung CD8+ T cells increases with chronic obstructive pulmonary disease severity and with in vitro stimulation by IL-18 or IL-15, *J. Immunol.*, **184** (2010), 6504–6513. https://doi.org/10.4049/jimmunol.1000006

197.R. Wang, J. J. Jaw, N. C. Stutzman, Z. Zou, P. D. Sun, Natural killer cell-produced IFN-$\gamma$ and TNF-$\alpha$ induce target cell cytolysis through up-regulation of ICAM-1, *J. Leukocyte Biol.*, **91** (2012), 299–309. https://doi.org/10.1189/jlb.0611308

198.M. Barberà-Cremades, A. I. Gómez, A. Baroja-Mazo, L. Martínez-Alarcón, C. M. Martínez, C. de Torre-Minguela, et al., P2X7 receptor induces tumor necrosis factor-$\alpha$ converting enzyme activation and release to boost TNF-$\alpha$ production, *Front. Immunol.*, **8** (2017), 862. https://doi.org/10.3389/fimmu.2017.00862

199.R. Chentouh, C. Fitting, J. M. Cavaillon, Specific features of human monocytes activation by monophosphoryl lipid A, *Sci. Rep.*, **8** (2018), 7096. https://doi.org/10.1038/s41598-018-25367-y

200.M. A. Brehm, K. A. Daniels, R. M. Welsh, Rapid production of TNF-$\alpha$ following TCR engagement of naive CD8 T cells, *J. Immunol.*, **175** (2005), 5043–5049. https://doi.org/10.4049/jimmunol.175.8.5043

201.Abcam, Human TNF-$\alpha$ ELISA kit (Fluorescent) (ab229399), 2026. Available from: https://www.abcam.com/en-us/products/elisa-kits/human-tnf-alpha-elisa-kit-fluorescent-ab229399.

202.R. Mehra, A. Storfer-Isser, H. L. Kirchner, N. Johnson, N. Jenny, R. P. Tracy, et al., Soluble interleukin 6 receptor: A novel marker of moderate to severe sleep-related breathing disorder, *Arch. Intern. Med.*, **166** (2006), 1725–1731. https://doi.org/10.1001/archinte.166.16.1725

203.J. Stagg, J. H. Wu, N. Bouganim, J. Galipeau, Granulocyte-macrophage colony-stimulating factor and interleukin-2 fusion cDNA for cancer gene immunotherapy, *Cancer Res.*, **64** (2004), 8795–8799. https://doi.org/10.1158/0008-5472.CAN-04-1776

204.P. Arnaud, Different interferons: Pharmacology, pharmacokinetics, proposed mechanisms, safety and side effects, *La Revue de Méd. Interne*, **23** (2002), 449S–458S. https://doi.org/10.1016/S0248-8663(02)00659-8

205.Y. Ma, S. Zhao, S. Shen, S. Fang, Z. Ye, Z. Shi, et al., A novel recombinant slow-release TNF $\alpha$-derived peptide effectively inhibits tumor growth and angiogensis, *Sci. Rep.*, **5** (2015), 13595. https://doi.org/10.1038/srep13595

206.J. E. Nesbitt, G. M. Fuller, Dynamics of interleukin-6 internalization and degradation in rat hepatocytes, *J. Biol. Chem.*, **267** (1992), 5739–5742. https://doi.org/10.1016/S0021-9258(18)42613-0

207.N. A. Nicola, L. Peterson, D. J. Hilton, D. Metcalf, Cellular processing of murine colony-stimulating factor (Multi-CSF, GM-CSF, G-CSF) receptors by normal hemopoietic cells and cell lines, *Growth Factors*, **1** (1988), 41–49. https://doi.org/10.3109/08977198809000245

208.D. E. Mager, W. J. Jusko, Receptor-mediated pharmacokinetic/pharmacodynamic model of interferon-$\beta$ 1a in humans, *Pharm. Res.*, **19** (2002), 1537–1543. https://doi.org/10.1023/a:1020468902694

209.R. Fischer, R. E. Kontermann, K. Pfizenmaier, Selective targeting of TNF receptors as a novel therapeutic approach, *Front. Cell Dev. Biol.*, **8** (2020), 401. https://doi.org/10.3389/fcell.2020.00401

210.M. Grell, H. Wajant, G. Zimmermann, P. Scheurich, The type 1 receptor (CD120a) is the high-affinity receptor for soluble tumor necrosis factor, *Proc. Natl. Acad. Sci.*, **95** (1998), 570–575. https://doi.org/10.1073/pnas.95.2.570

211.S. Tenhumberg, G. H. Waetzig, A. Chalaris, B. Rabe, D. Seegert, J. Scheller, et al., Structure-guided optimization of the interleukin-6 trans-signaling antagonist sgp130, *J. Biol. Chem.*, **283** (2008), 27200–27207. https://doi.org/10.1074/jbc.M803694200

212.R. Sadir, E. Forest, H. Lortat-Jacob, The heparan sulfate binding sequence of interferon-$\gamma$ increased the on rate of the interferon-$\gamma$-interferon-$\gamma$ receptor complex formation, *J. Biol. Chem.*, **273** (1998), 10919–10925. https://doi.org/10.1074/jbc.273.18.10919

213.M. Fallahi-Sichani, M. A. Schaller, D. E. Kirschner, S. L. Kunkel, J. J. Linderman, Identification of key processes that control tumor necrosis factor availability in a tuberculosis granuloma, *PLOS Comput. Biol.*, **6** (2010), e1000778. https://doi.org/10.1371/journal.pcbi.1000778

214.L. Snyers, V. Fontaine, J. Content, Modulation of interleukin-6 receptors in human cells, *Ann. N. Y. Acad. Sci.*, **557** (1989), 388–395. https://doi.org/10.1111/j.1749-6632.1989.tb24031.x

215.T. Taga, Y. Kawanishi, R. R. Hardy, T. Hirano, T. Kishimoto, Receptors for B cell stimulatory factor 2. quantitation, specificity, distribution, and regulation of their expression, *J. Exp. Med.*, **166** (1987), 967–981. https://doi.org/10.1084/jem.166.4.967

216.M. Yamaguchi, M. Michishita, K. Hirayoshi, K. Yasukawa, M. Okuma, K. Nagata, Down-regulation of interleukin 6 receptors of mouse myelomonocytic leukemic cells by leukemia inhibitory factor, *J. Biol. Chem.*, **267** (1992), 22035–22042. https://doi.org/10.1016/S0021-9258(18)41631-6

217.S. Chiba, A. Tojo, T. Kitamura, A. Urabe, K. Miyazono, F. Takaku, Characterization and molecular features of the cell surface receptor for human granulocyte-macrophage colony-stimulating factor, *Leukemia*, **4** (1990), 29–36.

218.D. R. Barreda, P. C. Hanington, M. Belosevic, Regulation of myeloid development and function by colony stimulating factors, *Dev. Comp. Immunol.*, **28** (2004), 509–554. https://doi.org/10.1016/j.dci.2003.09.010

219.A. A. Branca, Interferon receptors, *In Vitro Cell. Dev. Biol.*, **24** (1988), 155–165. https://doi.org/10.1007/BF02623541

220.S. N. Constantinescu, E. Croze, C. Wang, A. Murti, L. Basu, J. E. Mullersman, et al., Role of interferon alpha/beta receptor chain 1 in the structure and transmembrane signaling of the interferon alpha/beta receptor complex, *Proc. Natl. Acad. Sci.*, **91** (1994), 9602–9606. https://doi.org/10.1073/pnas.91.20.9602

221.K. Imamura, D. Spriggs, D. Kufe, Expression of tumor necrosis factor receptors on human monocytes and internalization of receptor bound ligand, *J. Immunol.*, **139** (1987), 2989–2992. https://doi.org/10.4049/jimmunol.139.9.2989

222.E. Pocsik, R. Mihalik, F. Ali-Osman, B. B. Aggarwal, Cell density-dependent regulation of cell surface expression of two types of human tumor necrosis factor receptors and its effect on cellular response, *J. Cell. Biochem.*, **54** (1994), 453–464. https://doi.org/10.1002/jcb.240540412

223.S. Kang, T. Tanaka, T. Kishimoto, Therapeutic uses of anti-interleukin-6 receptor antibody, *Int. Immunol.*, **27** (2015), 21–29. https://doi.org/10.1093/intimm/dxu081

224.T. Hirano, IL-6 in inflammation, autoimmunity and cancer, *Int. Immunol.*, **33** (2021), 127–148. https://doi.org/10.1093/intimm/dxaa078

225.P. J. Murray, The JAK-STAT signaling pathway: Input and output integration, *Int. Immunol.*, **178** (2007), 2623–2629. https://doi.org/10.4049/jimmunol.178.5.2623

226.R. Kurzrock, E. H. Estey, M. Talpaz, J. U. Gutterman, Granulocyte-macrophage colony-stimulating factor in myelodysplastic syndromes and aplastic anemia, *Biol. Response Modif. Treat. Hematopoietic Neoplasia*, **15** (1992), 173. https://doi.org/10.1002/14651858.CD009310.pub2

227.MyBioSource, IFN-beta recombinant protein: Interferon-beta 1a Recombinant Protein, 2020. Available from: https://www.mybiosource.com/ifn-beta-recombinant-protein/interferon-beta-1.

228.GenScript, TNF-$\alpha$, Human (Cat. No. Z01001), 2025. Available from: https://www.genscript.com/protein/Z01001-TNF_Human.html.

229.M. Rosenblum, N. Donato, Tumor necrosis factor alpha: A multifaceted peptide hormone, *Crit. Rev. Immunol.*, **9** (1989), 21–44.

230.Interferon-$\gamma$ protein, recombinant human. Available from: https://www.sigmaaldrich.com/US/en/product/mm/if002?emdredirect=1.

231.Useful pharmacokinetic equations, 2013. Available from: https://pharmacy.ufl.edu/files/2013/01/5127-28-equations.pdf.

232.INTERFERON GAMMA-1B, Available from: https://drugs.ncats.io/substance/21K6M2I7AG.

233.K. Pallmer, A. Oxenius, Recognition and regulation of T cells by NK cells, *Front. Immunol.*, **7** (2016), 251. https://doi.org/10.3389/fimmu.2016.00251

234.L. Cifaldi, G. Prencipe, I. Caiello, C. Bracaglia, F. Locatelli, F. De Benedetti, et al., Inhibition of natural killer cell cytotoxicity by interleukin-6: Implications for the pathogenesis of macrophage activation syndrome, *Arthritis rheumatol.*, **67** (2015), 3037–3046. https://doi.org/10.1002/art.39295

## Appendix materials

*Cytokine's average receptor number*

$$A_L = \frac{MM_L}{6.02214 \times 10^{23}}(K_{L,N} + K_{L,M} + K_{L,T})\frac{10^{-3}}{5000}, \tag{A.1}$$

$$A_G = \frac{MM_G}{6.02214 * 10^{23}}K_{G,M}\frac{10^{-3}}{5000}, \tag{A.2}$$

$$A_C = \hat{p}\frac{MM_C}{6.02214 * 10^{23}}K_{C,N}\frac{10^{-3}}{5000}, \tag{A.3}$$

$$A_F = \frac{MM_F}{6.02214 * 10^{23}}(K_{F,T} + K_{F,I})\frac{10^{-3}}{5000}, \tag{A.4}$$

$$A_\gamma = \frac{MM_\gamma}{6.02214 \times 10^{23}}(K_{\gamma,T} + K_{\gamma,M_{\Phi I}} + K_{\gamma,I})\frac{10^{-3}}{5000}, \tag{A.5}$$

$$A_\alpha = \frac{MM_\alpha}{6.02214 \times 10^{23}}(K_{\alpha,T} + K_{\alpha,M_{\Phi I}} + K_{\alpha,K} + K_{\alpha,I} + K_{\alpha,M})\frac{10^{-3}}{5000}. \tag{A.6}$$

*Table of model parameters*

We provide the detailed information for the parameters and their values, shown in Eqs (2.1)–(2.23), and for how parameters were estimated. Specifically, model parameters were obtained either from the literature or through data-fitting to dose response data or time-series measurements. Remaining parameters were estimated based on homeostasis calculation.

**Table A.1.** Initial conditions for model variables (H refers to homeostasis calculation).

| Symbol | Description | Unit | Value | Reference |
|---|---|---|---|---|
| $V_0$ | Initial viral load | $\log_{10}$(cop/ml) | 4.5 | [143] |
| $S_0$ | Initial susceptible cells | $10^9$ cells/ml | 0.16 | [144, 145] |
| $I_0$ | Initial infected cells | $10^9$ cells/ml | 0 | – |
| $R_0$ | Initial resistant cells | $10^9$ cells/ml | 0 | – |
| $M_{\Phi R,0}$ | Initial resident macrophages | $10^9$ cells/ml | $2.7 \times 10^{-5}$ | [144] |
| $M_{\Phi I,0}$ | Initial inflammatory macrophages | $10^9$ cells/ml | $1.5 \times 10^{-6}$ | H |
| $M_0$ | Initial monocytes | $10^9$ cells/ml | 0.0004 | [146] |
| $M_R$ | Initial reservoir monocytes | $10^9$ cells/ml | 0.0023 | [14] |
| $N_0$ | Initial neutrophils | $10^9$ cells/ml | 0.0053 | [84] |
| $N_R$ | Initial reservoir neutrophils | $10^9$ cells/ml | 0.0316 | [84] |
| $T_0$ | Initial $CD8^+$ T cells | $10^9$ cells/ml | $1.1 \times 10^{-4}$ | [147, 148] |
| $K_0$ | Initial NK cells | $10^9$ cells/ml | $7.15 \times 10^{-5}$ | [149] |
| $K_R$ | Initial reservoir NK cells | $10^9$ cells/ml | $1.1 \times 10^{-4}$ | [150] |
| $L_{U,0}$ | Initial unbound IL-6 | pg/ml | 1.1 | [151] |
| $L_{B,0}$ | Initial bound IL-6 | pg/ml | $1.4 \times 10^{-6}$ | H |
| $G_{U,0}$ | Initial unbound GM-CSF | pg/ml | 2.43 | [152] |
| $G_{B,0}$ | Initial bound GM-CSF | pg/ml | $1.6 \times 10^{-8}$ | H |
| $C_{U,0}$ | Initial unbound G-CSF | ng/ml | 0.025 | [84] |
| $C_{B,0}$ | Initial bound G-CSF | ng/ml | $6.5 \times 10^{-10}$ | [84] |
| $F_{U,0}$ | Initial unbound type I IFN | pg/ml | 0.015 | [153] |
| $F_{B,0}$ | Initial bound type I IFN | pg/ml | $1.1 \times 10^{-8}$ | H |
| $\gamma_{U,0}$ | Initial unbound IFN-$\gamma$ | pg/ml | 0.91 | [154] |
| $\gamma_{B,0}$ | Initial bound IFN-$\gamma$ | pg/ml | $1.432 \times 10^{-7}$ | H |
| $\alpha_{U,0}$ | Initial unbound TNF-$\alpha$ | pg/ml | 0.7 | [155] |
| $\alpha_{B,0}$ | Initial bound TNF-$\alpha$ | pg/ml | $1.3 \times 10^{-6}$ | H |

**Table A.2.** Parameter modifications for severe COVID-19 disease in Figure 2.

| Symbol | Description | Unit | Mild case | Severe case | Reference |
|---|---|---|---|---|---|
| $p_{F,I}$ | Production of type I IFN by infected cells | pg/ml/day | 2.82 | 0.002 | [156] |
| $p_{M,I}$ | Monocyte recruitment rate by infected cells | 1/day | 0.22 | 1.2 | [157] |
| $\eta_{F,M_{\Phi I}}$ | Cytokine production half-effect coefficient of type I IFN by inflammatory macrophages | $10^9$ cells/ml | $1.3 \times 10^{-6}$ | $2 \times 10^{-4}$ | H |
| $\epsilon_{L,K}$ | Half effect constant for IL-6 inhibition of NK cell cytotoxicity | pg/ml | $2.102 \times 10^{-5}$ | $2.102 \times 10^{-6}$ | [83] |
| $p_{\gamma,T}$ | Production rate of IFN-$\gamma$ by T cells | pg/ml/day | 300 | 30 | [158] |

**Table A.3.** Viral kinetic parameters.

| Symbol | Description | Unit | Value | Reference |
|---|---|---|---|---|
| $p$ | Lytic viral production rate | 1/day $\times$ $\log_{10}$(cop/ml)/$10^9$ cells | 591 | [143] |
| $\beta$ | Transmission rate (or virus infection rate) | 1/day $\times$ 1/$\log_{10}$(cop/ml)/$10^9$ cells | 0.29 | [143] |
| $S_{max}$ | Epithelial cells carrying capacity | $10^9$ cells | $S_0 = 0.16$ | [144] |
| $M_{\Phi_{max}}$ | Macrophage carrying capacity | $10^9$ cells | $M_{\Phi R,0} = 2.7{\times}10^{-5}$ | [14] |
| $\lambda_S$ | Proliferation of epithelial cells | 1/day | 0.74 | [159] |
| $\lambda_{M_\Phi}$ | Production of alveolar macrophages | $\log_{10}$(cop/ml)/day | 5943 | [160] |
| $\tau_I$ | Eclipse time | day | 0.17 | [161] |
| $d_I$ | Death rate of infected cells | 1/day | 0.1 | [14] |
| $\tau_T$ | Delay in $CD8^+$ T cell arrival | day | 4.5 | [71] |

**Table A.4.** Cell production, recruitment, and activation rates (H refers to homeostasis calculation).

| Symbol | Description | Unit | Value | Reference |
|---|---|---|---|---|
| $p_{M_{\Phi I},G}$ | Monocyte to macrophage differentiation by GM-CSF | 1/day | 1.68 | [35] |
| $p_{M_{\Phi I},L}$ | Monocyte to macrophage differentiation by IL-6 | 1/day | 0.78 | [76, 77] |
| $a_{I,M_\Phi}$ | Activation of macrophages by infected and dead cells | ml/($10^9$ cells) × (1/day) | $1.1 \times 10^3$ | [162, 163] |
| $p_{M,I}$ | Monocyte recruitment rate by infected cells | 1/day | 0.22 | [157] |
| $p_{T,F}$ | $CD8^+$ T cell production rate by IFN | 1/day | 4 | [164] |
| $p_{T,\gamma}$ | $CD8^+$ T cell production rate by IFN-$\gamma$ | 1/day | 6.56 | [165] |
| $p_{N,L}$ | Neutrophil recruitment rate by IL-6 | 1/day | 0.21 | Homeostasis (H) |
| $p_{T,L}$ | $CD8^+$ T cell recruitment rate by IL-6 | 1/day | 4 | [166] |
| $p_{T,I}$ | $CD8^+$ T cell proliferation rate | 1/day | 0.016 | [167] |
| $p_K$ | NK proliferation rate | 1/day | 0.0365 | [78] |
| $p_{K,\alpha}$ | NK production rate by TNF-$\alpha$ | 1/day | 0.2148 | [78] |
| $M^*_{prod}$ | Homeostasis reservoir release rate | 1/day | 0.13 | H |
| $\psi_{M_{max}}$ | Maximal reservoir release rate | 1/day | 11.55 | [168] |
| $N^*_{prod}$ | Homeostasis reservoir release rate | 1/day | 0.21 | H |
| $\psi_{N_{max}}$ | Maximal reservoir release rate | 1/day | 4.13 | [84] |
| $K^*_{prod}$ | Homeostasis reservoir release rate | 1/day | 0.1 | H |
| $C^*_{BF}$ | Homeostasis neutrophil receptor bound fraction | – | $1.6 \times 10^{-5}$ | [84] |

**Table A.5.** Cell-related half-effect ($\epsilon$), IC50 ($IC_{50}$), and Hill coefficient ($h$) parameters.

| Symbol | Description | Unit | Value | Reference |
|---|---|---|---|---|
| $\epsilon_{F,I}$ | Type I IFN inhibition of viral production | pg/ml | $2 \times 10^{-4}$ | [91] |
| $\epsilon_{\gamma,I}$ | IFN-$\gamma$ inhibition of viral production | pg/ml | $3.147 \times 10^{-4}$ | [169] |
| $\epsilon_{L,M_\Phi}$ | IL-6 monocytes to macrophages | pg/ml | 0.001 | [76] |
| $\epsilon_{\alpha,M_{\Phi I}}$ | TNF-$\alpha$ inhibition of macrophage differentiation | pg/ml | 0.001093 | [76] |
| $\epsilon_{G,M_{\Phi I}}$ | GM-CSF monocyte to macrophages | pg/ml | 0.027 | [170] |
| $\epsilon_{G,M}$ | GM-CSF recruitment of monocytes | pg/ml | 57.2 | [43] |
| $\epsilon_{F,T}$ | Type I IFN production of $CD8^+$ T cells | pg/ml | 0.004 | [171] |
| $\epsilon_{\gamma,T}$ | IFN-$\gamma$ production of $CD8^+$ T cells | pg/ml | 0.004 | [171] |
| $\epsilon_{C,N}$ | G-CSF recruitment of neutrophils | unitless | $1.89 \times 10^{-4}$ | [84] |
| $\epsilon_{L,N}$ | IL-6 recruitment of neutrophils | pg/ml | 57.2 | [43] |
| $\epsilon_{I,M}$ | Infected cell monocyte recruitment | $10^9$ cells/ml | 0.11 | [14] |
| $\epsilon_{L,T}$ | IL-6 production of $CD8^+$ T cells | pg/ml | $1.5 \times 10^{-5}$ | [172] |
| $\epsilon_{V,M_\Phi}$ | Viral load for macrophage replenishing | $\log_{10}$(cop/ml) | 0.905 | [173] |
| $\epsilon_{T,I}$ | Antigen driven proliferation | $10^9$ cells/ml | $10^{-6}$ | [167] |
| $\epsilon_{L,K}$ | IL-6 inhibition of NK cell cytotoxicity | pg/ml | $2.102 \times 10^{-5}$ | [83] |
| $\epsilon_{K,I}$ | NK cells lyse infected cells | $10^9$ cells/ml | $2.345\times 10^{-3}$ | [174] |
| $\epsilon_{K,T}$ | NK cells lyse T cells | $10^9$ cells/ml | $3.646\times 10^{-3}$ | [175] |
| $\epsilon_{\alpha,K}$ | TNF-$\alpha$ recruitment of NK cells | pg/ml | 0.06192 | [78] |
| $\epsilon_{\gamma,\alpha}$ | TNF-$\alpha$ and IFN-$\gamma$ synergestic induced damage to inflammatory macrophages | $(\text{pg/ml})^2$ | $1.994 \times 10^{-5}$ | [52] |
| $h_M$ | GM-CSF monocyte recruitment | – | 1.67 | [43] |
| $h_{M_{\Phi I},\alpha}$ | TNF-$\alpha$ inhibition of inflammatory macrophage differentiation | – | 0.4 | [76] |
| $h_{M,M_\Phi}$ | GM-CSF monocyte to macrophages | – | 2.03 | [170] |
| $h_N$ | Neutrophil induced damage | – | 3.02 | [162] |
| $\text{IC}_{50,N}$ | Neutrophil induced damage | $10^9$ cells/ml | 0.047 | [162] |

**Table A.6.** Cell/virus-induced death rates.

| Symbol | Description | Unit | Value | Reference |
|---|---|---|---|---|
| $\delta_{V,M_\Phi}$ | Rate of viral clearance by macrophages | ml/($10^9$ cells) × 1/day | 1152 | [176] |
| $\delta_{V,N}$ | Rate of viral clearance by neutrophils | ml/($10^9$ cells) × 1/day | 1047 | [14] |
| $\delta_N$ | Rate of neutrophil inflicted damage | 1/day | 1.68 | [176] |
| $\rho$ | Bystander death modulation constant | – | 0.5 | [14] |
| $\delta_{I,M_\Phi}$ | Rate macrophages phagocytose infected cells | ml/($10^9$ cells) × 1/day | 121 | [177] |
| $\delta_{I,T}$ | Rate $CD8^+$ T cells induce apoptosis in infected cells | ml/($10^9$ cells) × 1/day | 47.6 | [178] |
| $\delta_{I,K}$ | Rate NK cells lyse infected cells | 1/day | 1.037 | [174] |
| $\delta_{T,K}$ | Rate NK cells lyse T cells | 1/day | 0.1593 | [175] |
| $\delta_{M_{\Phi I}}$ | Rate inflammatory macrophages die due to TNF-$\alpha$ and IFN-$\gamma$ | 1/day | 0.1543 | [52] |
| $\delta_{M_{\Phi,D}}$ | Rate macrophages die from phagocytosis | ml/($10^9$ cells) × 1/day | 6.06 | [74, 179] |
| $\delta_{D,M_\Phi}$ | Rate macrophages phagocytose dead cells | ml/($10^9$ cells) × 1/day | 8.03 | [74] |

**Table A.7.** Cell death and virus decay rates.

| Symbol | Description | Unit | Value | Reference |
|---|---|---|---|---|
| $d_V$ | Viral decay rate | 1/day | 0 | [180] |
| $d_D$ | Degradation rate of apoptosed cells | 1/day | 8 | [75] |
| $d_{M_{\Phi R}}$ | Alveolar macrophage death rate | 1/day | 0 | [181] |
| $d_{M_{\Phi I}}$ | Inflammatory macrophage death rate | 1/day | 0.3 | [182] |
| $d_M$ | Monocyte death rate | 1/day | 0.76 | [183] |
| $d_N$ | Neutrophil death rate | 1/day | 1.28 | [84] |
| $d_T$ | $CD8^+$ T cell death rate | 1/day | 0.4 | [184] |
| $d_K$ | NK cell death rate | 1/day | 0.156 | [185] |

**Table A.8.** Cytokine production rates.

| Symbol | Description | Unit | Value | Reference |
|---|---|---|---|---|
| $p_{L,I}$ | IL-6 production by infected cells | pg/ml/day | 11.89 | [186] |
| $p_{L,M_\Phi}$ | IL-6 production by activated macrophages | pg/ml/day | 1872 | [187] |
| $p_{L,M}$ | IL-6 production by monocytes | pg/ml/day | 36.28 | [188] |
| $p_{G,M_{\Phi I}}$ | GM-CSF production by inflammatory macrophages | pg/ml/day | 2626 | [189] |
| $p_{G,M}$ | GM-CSF production by monocytes | pg/ml/day | 3070 | [190] |
| $p_{C,M}$ | G-CSF production by monocytes | pg/ml/day | 30.70 | [14] |
| $p_{F,I}$ | Type I IFN production by infected cells | pg/ml/day | 2.82 | [156] |
| $p_{F,M_{\Phi I}}$ | Type I IFN production by inflammatory macrophages | pg/ml/day | 1.3 | [14] |
| $p_{F,M}$ | Type I IFN production by monocytes | pg/ml/day | 3.56 | [191, 192] |
| $p_{\gamma,K}$ | IFN-$\gamma$ production by NK cells | pg/ml/day | 325 | [193] |
| $p_{\gamma,T}$ | IFN-$\gamma$ production by T cells | pg/ml/day | 300 | [158] |
| $p_{\alpha,M_{\Phi I}}$ | TNF-$\alpha$ production by inflammatory macrophages | pg/ml/day | 3824 | [187] |
| $p_{\alpha,M}$ | TNF-$\alpha$ production by monocytes | pg/ml/day | 110 | [194, 195] |
| $p_{\alpha,T}$ | TNF-$\alpha$ production by T cells | pg/ml/day | 450 | [196] |
| $p_{\alpha,K}$ | TNF-$\alpha$ production by NK Cells | pg/ml/day | 1000 | [193, 197] |

**Table A.9.** Cytokine production half-effect ($\eta$) parameters.

| Symbol | Description | Unit | Value | Reference |
|---|---|---|---|---|
| $\eta_{L,I}$ | IL-6 production by infected cells | $10^9$ cells/ml | 0.7 | [186] |
| $\eta_{L,M}$ | IL-6 by monocytes | $10^9$ cells/ml | 0.0045 | [188] |
| $\eta_{L,M_{\Phi I}}$ | IL-6 by inflammatory macrophages | $10^9$ cells/ml | $1.82 \times 10^{-4}$ | [187] |
| $\eta_{G,M_{\Phi I}}$ | GM-CSF by macrophages | $10^9$ cells/ml | $1.82 \times 10^{-4}$ | [14] |
| $\eta_{G,M}$ | GM-CSF by monocytes | $10^9$ cells/ml | 0.15 | H |
| $\eta_{C,M}$ | G-CSF by monocytes | $10^9$ cells/ml | $8 \times 10^{-4}$ | H |
| $\eta_{F,I}$ | Type I IFN by infected cells | $10^9$ cells/ml | 0.011 | [156] |
| $\eta_{F,M_{\Phi I}}$ | Type I IFN by inflammatory macrophages | $10^9$ cells/ml | $2 \times 10^{-4}$ | H |
| $\eta_{F,M}$ | Type I IFN by monocytes | $10^9$ cells/ml | 0.54 | [191, 192] |
| $\eta_{\gamma,K}$ | IFN-$\gamma$ by NK cells | $10^9$ cells/ml | $2.99\times10^{-4}$ | [193] |
| $\eta_{\gamma,T}$ | IFN-$\gamma$ by T cells | $10^9$ cells/ml | $8.37\times10^{-5}$ | [183] |
| $\eta_{\alpha,M_{\Phi I}}$ | TNF-$\alpha$ by inflammatory macrophages | $10^9$ cells/ml | $2.22\times10^{-4}$ | [198] |
| $\eta_{\alpha,M}$ | TNF-$\alpha$ by monocytes | $10^9$ cells/ml | 0.3851 | [199] |
| $\eta_{\alpha,T}$ | TNF-$\alpha$ by T cells | $10^9$ cells/ml | $9.706\times 10^{-5}$ | [200, 201] |
| $\eta_{\alpha,K}$ | TNF-$\alpha$ by NK cells | $10^9$ cells/ml | $4.29 \times 10^{-4}$ | [193, 197] |

**Table A.10.** Cytokine (renal) clearance and internalization rates.

| Symbol | Description | Unit | Value | Reference |
|---|---|---|---|---|
| $k_{lin_L}$ | Rate of IL-6 renal clearance | 1/day | 16.6 | [202] |
| $k_{lin_G}$ | Rate of GM-CSF renal clearance | 1/day | 11.7 | [203] |
| $k_{lin_C}$ | Rate of G-CSF renal clearance | 1/day | 0.16 | [84] |
| $k_{lin_F}$ | Rate of type I IFN renal clearance | 1/day | 16.63 | [204] |
| $k_{lin_\gamma}$ | Rate of IFN-$\gamma$ renal clearance | 1/day | 28.5 | [204] |
| $k_{lin_\alpha}$ | Rate of TNF-$\alpha$ renal clearance | 1/day | 33.27 | [205] |
| $k_{int_L}$ | Internalization rate of IL-6 | 1/day | 61.8 | [206] |
| $k_{int_G}$ | Internalization rate of GM-CSF | 1/day | 73.4 | [207] |
| $k_{int_C}$ | Internalization rate of G-CSF | 1/day | 462 | [84] |
| $k_{int_F}$ | Internalization rate of type I IFN | 1/day | 17 | [208] |
| $k_{int_\gamma}$ | Internalization rate of IFN-$\gamma$ | 1/day | 17 | [14] |
| $k_{int_\alpha}$ | Internalization rate of TNF-$\alpha$ | 1/day | 57.6 | [209,210] |

**Table A.11.** Cytokine binding/unbinding rates and stoichiometric constants.

| Symbol | Description | Unit | Value | Reference |
|---|---|---|---|---|
| $k_{B_L}$ | IL-6 binding rate | ml/pg/day | 0.0018 | [211] |
| $k_{B_G}$ | GM-CSF binding rate | ml/pg/day | 0.0021 | [207] |
| $k_{B_C}$ | G-CSF binding rate | ml/ng/day | 2.24 | [84] |
| $k_{B_F}$ | IFN binding rate | ml/pg/day | 0.011 | [208] |
| $k_{B_\gamma}$ | IFN-$\gamma$ binding rate | ml/pg/day | 0.0382 | [212] |
| $k_{B_\alpha}$ | TNF-$\alpha$ binding rate | ml/pg/day | 0.096 | [213] |
| $k_{U_L}$ | IL-6 unbinding rate | 1/day | 22.3 | [211] |
| $k_{U_G}$ | GM-CSF unbinding rate | 1/day | 522 | [207] |
| $k_{U_C}$ | G-CSF unbinding rate | 1/day | 184 | [84] |
| $k_{U_F}$ | IFN unbinding rate | 1/day | 6.07 | [208] |
| $k_{U_\gamma}$ | IFN-$\gamma$ unbinding rate | 1/day | 432 | [212] |
| $k_{U_\alpha}$ | TNF-$\alpha$ unbinding rate | 1/day | 449.46 | [213] |
| W | Stoichiometric constant (G-CSF) | – | 1.4608 | [84] |
| $\hat{p}$ | Stoichiometry relating constant (IL-6, GM-CSF, IFN, IFN-$\gamma$, TNF-$\alpha$) | – | 1 | [14] |
| $\hat{p}$ | Stoichiometry relating constant (G-CSF) | – | 2 | [84] |

**Table A.12.** Number of cellular receptors and cytokine molecular weights.

| Symbol | Description | Unit | Value | Reference |
|---|---|---|---|---|
| $K_{L,N}$ | No. IL-6 receptors on neutrophils | sites/cell | 720 | [214] |
| $K_{L,T}$ | No. IL-6 receptors on T cells | sites/cell | 300 | [215] |
| $K_{L,M}$ | No. IL-6 receptors on monocytes | sites/cell | 509 | [216] |
| $K_{G,M}$ | No. GM-CSF receptors on monocytes | sites/cell | 1058 | [217] |
| $K_{C,N}$ | No. G-CSF receptors on neutrophils | sites/cell | 600 | [218] |
| $K_{F,T}$ | No. of type I IFN receptors on T cells | sites/cell | 1000 | [219] |
| $K_{F,I}$ | No. of type I IFN receptors on infected cells | sites/cell | 1300 | [220] |
| $K_{\gamma,T}$ | No. of IFN-$\gamma$ receptors on T cells | sites/cell | 500 | [212] |
| $K_{\gamma,I}$ | No. of IFN-$\gamma$ receptors on infected cells | sites/cell | 1800 | [212] |
| $K_{\gamma,M_{\Phi I}}$ | No. of IFN-$\gamma$ receptors on inflammatory macrophages | sites/cell | 760 | [219] |
| $K_{\alpha,M}$ | No. of TNF-$\alpha$ receptors on monocytes | sites/cell | 230 | [221] |
| $K_{\alpha,T}$ | No. of TNF-$\alpha$ receptors on T cells | sites/cell | 300 | [213] |
| $K_{\alpha,M_{\Phi I}}$ | No. of TNF-$\alpha$ receptors on inflammatory macrophages | sites/cell | 1500 | [213] |
| $K_{\alpha,I}$ | No. of TNF-$\alpha$ receptors on infected cells | sites/cell | 714 | [222] |
| $K_{\alpha,K}$ | No. of TNF-$\alpha$ receptors on NK cells | sites/cell | 230 | [221] |
| $MM_L$ | Molecular weight of IL-6 | g/mol | 21,000 | [223–225] |
| $MM_G$ | Molecular weight of GM-CSF | g/mol | 14,000 | [226] |
| $MM_C$ | Molecular weight of G-CSF | g/mol | 19,600 | [84] |
| $MM_F$ | Molecular weight of IFN-$\beta$ | g/mol | 19,000 | [227] |
| $MM_\gamma$ | Molecular weight of IFN-$\gamma$ | g/mol | 16,500 | [204] |
| $MM_\alpha$ | Molecular weight of TNF-$\alpha$ | g/mol | 17,300 | [228, 229] |

*Parameters taken from literature*

NK cell proliferation rate

NK cells are proliferated and activated by various cytokines that are not explicitly represented in our model. For example, IL-2 is a primary cytokine responsible for the proliferation and activation of NK cells. To make up for IL-2's effect, incorporating a proliferation rate into Eq (2.8) in our model is essential. The proliferation rate of NK cells in both young and elderly adults was measured using Ki67 assay [185]. The results indicated no significant difference between the two age groups, so the average NK proliferation rate of $p_K = 0.0365$/day.

NK cell death rate

Like normal cells, NK cells undergo cell death via apoptosis. They undergo apoptosis to regulate immune responses, ensure immune system balance, and prevent prolonged or excessive activity. Hence, a death rate for NK is necessary in Eq (2.8). The apotosis rate of NK cells in both young and elderly adults was measured using terminal deoxynucleotidyl transferase dUTP nick end labeling (TUNEL) assay [185]. The results similarly indicated no significant difference between the two age groups, so the average NK apoptosis rate of $d_K = 0.156$/day is used.

TNF-$\alpha$ internalization rate

Similarly to other cytokines, TNF-$\alpha$ occasionally internalizes into a cell after binding to cell receptors [44]. It should be noted that TNF-$\alpha$ can contain two distinct internalization rates due to having multiple receptors. Namely, TNF-$\alpha$ can bind to TNF-$\alpha$ receptor 1 (TNFR1) and TNF-$\alpha$ receptor 2 (TNFR2) [210]. TNFR1 and TNFR2 have internalization rates of 66.528 and 39.744 per day, respectively [213]. To capture both receptors in our model while incorporating the fact that TNFR1 having higher affinity [210], we take a weighted average of both internalization rates, with TNFR1 having a weight of 0.66 and TNFR2 having a weight 0.33. Through this process we obtain a weighted average $k_{int_\alpha}$ of 57.6 per day.

TNF-$\alpha$ unbinding and binding, and renal clearance rates

Upon binding to a cell receptor, cytokines will eventually unbind, discontinuing the cytokine to cell interaction [221]. TNF-$\alpha$'s unbinding average across both TNFR1 and TNFR2 receptors are found to be 449.46 per day [213]. We thus use $k_{U_\alpha} = 449.46$/day. The rate in which TNF-$\alpha$ binds to cell receptors is found by calculating the weighted average between both receptors. Using different weights (0.66 and 0.33) for TNFR1 and TNFR2, respectively, our average binding rate is $k_{B_\alpha} = 0.096$ pg/ml/day [213]. Circulating (unbound) TNF-$\alpha$ is filtered and cleared away from the system at rate $k_{lin_\alpha}$ of 33.27 per day [205].

TNF-$\alpha$ molecular weight and receptor counts

TNF-$\alpha$, in its common form, has been reported by various studies [228, 229] to possess a molecular weight of 17,300 kD (or g/mol). Thus, $MM_\alpha = 17{,}300$ g/mol.

In our model, monocytes, inflammatory macrophages, NK cells, T cells, and infected cells are found to have significant numbers of TNF-$\alpha$ receptors (TNFR) [213]. While some studies have varying numbers of TNFR, with an upper and lower bound of receptor counts, we specifically looked at lower bounds as we found that studies with higher levels of TNFR often contained stimulants that likely altered surface receptor expressions [221]. Concluding our search for TNF-$\alpha$ receptor counts, we find that, approximately, monocytes contain 230 TNFR, $CD8^+$ T cells contain 300 TNFR, infected cells contain 714 TNFR, and macrophages contain 1500 TNFR [213]. Since it is difficult to find NK cell receptor counts, we decide to set NK TNFR expression similar to monocyte TNFR expressions, as both are from the same lineage of cells [221].

TNF-$\alpha$ initial unbound and bound levels

We obtained the initial levels of unbounded TNF-$\alpha$ by finding the average circulating serum levels of TNF-$\alpha$ in healthy adults across diverse age groups [155]. Studies suggest unbounded levels to be around 0.7 pg/ml, with a statistical significance of $p < 0.025$. Regarding the bounded TNF-$\alpha$ parameter, we calculated it using the following equations:

$$A_\alpha = \frac{MM_\alpha \times 10^{12}}{6.02214 \times 10^{-23}}(K_{\alpha,M_{\Phi I}} + K_{\alpha,T} + K_{\alpha,I} + K_{\alpha,M} + K_{\alpha,K}) \times 10^9 \times \frac{1}{5000},$$
$$\alpha_{B_0} = \frac{k_B \times A_\alpha \times \alpha_{U_0} \times (M_{\Phi I} + M + K)}{k_B \times \alpha_{U_0} + k_{int} + k_U}.$$

Using Eq (A.29) (calculated from homeostasis), we found initial bounded TNF-$\alpha$ levels $\alpha_{B,0}$ to be approximately $1.3 \times 10^{-6}$ pg/ml.

IFN-$\gamma$ inhibition of viral production

Both type I IFN and IFN-$\gamma$ inhibit viral production through the release of interferon stimulated genes (ISGs) [47]. The study in [169] attempted to measure how well IFN-$\gamma$ could inhibit viral replication as well as type 1 IFNs. Using viral plaques as the measure of viral inhibition, this study showed that 100 U/ml of IFN-$\gamma$ was enough to cut viral plaque numbers in half, representing a half effect concentration. In order to convert this number to pg/ml, two steps were taken. First, we divide the half effect concentration by a specific activity derived from the results in [230]. This provides us with $\frac{100}{5\times10^7}$ = 2000 pg/ml.

Since 2000 pg/ml is the number of free circulating IFN-$\gamma$ that produces this effect, we must convert this number to the amount of bound IFN-$\gamma$. We do this by multiplying the unbounded half effect by the ratio between initial bound and unbound IFN-$\gamma$. That is, $2000 \times \frac{1.432\times10^{-7}}{0.91} = 3.147 \times 10^{-4}$ pg/ml.

Internalization rate of IFN-$\gamma$

Given limited information on the pharamcodynamics of IFN-$\gamma$, we choose to use the internalization rate of IFN type I, reported by [14] to be 17/day.

IFN-$\gamma$ unbinding and binding, and renal clearance rates

The half life of IFN-$\gamma$ was reported by [204] to be between 25–35 minutes. Picking the upper bound gives us a half life equivalent to 0.0243 days. We then turned the half life into the clearance rate by rearranging equations from [231]. This gives us $k_{lin_\gamma} = \frac{ln(2)}{0.0243} = 28.5$/day. Sadir et al. [212] reported an unbinding rate $k_{\text{off}} = 5 \times 10^{-3}$/s for IFN-$\gamma$, which converts to $k_{U_\gamma} = 0.005 \times 86{,}400 = 432$/day.

The reported binding rate is $k_{\text{on}} = 7.3 \times 10^6$ 1/(M × s) (or L/(mol × s)) [212]. To express this in ml/pg/day, we divide by the molecular weight $M_\gamma$ in ml/pg/day and convert units: $k_{\text{on}} = (7.3 \times 10^6 \times 1000 \times 86{,}400)/M_\gamma$. We then derive the molar mass from the molecular weight, taking $M_\gamma$ = 16.5 kDa = $1.65 \times 10^{16}$ pg mol$^{-1}$ [232], giving $k_{B_\gamma} \approx 0.0382$ ml/pg/day.

Lastly, the terminal half-life of human IFN-$\gamma$ is $t_{1/2}$ = 25–35 min [204]; using the upper bound (35 min = 0.0243 day), the first-order clearance rate is $k_{lin_\gamma} = \ln(2)/t_{1/2} \approx 28.5$/day.

IFN-$\gamma$ receptor counts

The amount of IFN-$\gamma$ receptors on T cells and infected cells are found from [212]. The receptor counts are $K_{\gamma,I}$ = 1800 receptors/cell and $K_{\gamma,T}$ = 500 receptors/cells. The receptor counts for macrophages were found to be $K_{\gamma,M_{\Phi I}}$ = 760 receptors/cell from [219].

*Parameters estimated from data fitting*

Figures A.1–A.3 present the parameter estimation results obtained through data fitting. Detailed explanations are provided in each subsection below.

Effect of NK cells on infected cells

At higher relative densities of target cells, it is more likely that NK cells encounter target cells that can trigger degranulation. This means that the number of infected cells affect the NK cell's cytotoxicity. NK cell's targeting on infected cells is therefore modeled by:

$$\frac{dI}{dt} = -\frac{\delta_{I,K} I K}{K + \epsilon_{K,I}}, \tag{A.7}$$

where $\delta_{I,K}$ is the infected cells death rate by NK cells measured in 1/day. The study in [174] measured NK cell lysis dependent on NK cell and infected cells. We fit the data to Eq (A.7), resulting in $\delta_{I,K} = 1.037$ 1/day and $\epsilon_{K,I} = 2.345 \times 10^{-3}$ (in $10^9$ cells/ml) with 95% confidence interval (0.8927, 1.18) and $(1.476 \times 10^{-3}, 3.214 \times 10^{-3})$, respectively, as shown in Figure A.1A.

Effect of NK cells on T cells

The study in [233] observed an increase in T cells differentiation when NK is depleted in vivo setting. The dynamic is modeled by:

$$\frac{dT}{dt} = -\frac{\delta_{T,K} T K}{K + \epsilon_{K,T}}, \tag{A.8}$$

where $\delta_{T,K}$ is T-cell death rate by NK cells measured in 1/day. Cytotoxicity assays are conducted utilizing IL-2–activated NK cells as effectors and T cells as target cells [175]. Data fitting involving both natural killer group 2, member D (NKG2D) and DNAX accessory molecule-1 (DNAM-1) receptors to the model equation (A.8) yielded $\delta_{T,K} = 0.1593$ 1/day with 95% confidence interval of (0.146, 0.1725) 1/day (see Figure A.1B).

Effect of TNF-$\alpha$ on NK proliferation

TNF-$\alpha$ promotes aerobic glycolysis, mediating NK cell proliferation. Proliferation of NK cells by TNF-$\alpha$ is given by:

$$\frac{dK}{dt} = \frac{p_{K,\alpha} \alpha_B K}{\alpha_B + \epsilon_{\alpha,K}}, \tag{A.9}$$

where $p_{K,\alpha}$ is the NK production rate by TNF-$\alpha$ measured in 1/day. Khan et al. [78] observed that TNF-$\alpha$ promotes activation and proliferation of NK cells. The percentage of CD25+ cells were measured using stimulation with different doses of TNF-$\alpha$ ex vivo for 3 days. CD25+ is a marker for activated NK cells. Data fitting to the modeled equation yields $p_{K,\alpha} = 0.2148$ 1/day with 95% confidence interval of (0.111, 0.3184) 1/day. The fitting is shown in Figure A.1C.

NK cytotoxicity inhibition by IL-6

IL-6 does not reduce the number of NK cells but decreases their cytotoxic activity. A study in [234] observed no significant difference in the number of NK cells activated with or without IL-6. However, in the presence of IL-6, there was a significant decrease in NK cytotoxicity. This suggests an inhibitory dynamic, where IL-6 reduces the cytotoxicity of NK cells toward infected cells and T-cells. Consequently, the IL-6 term is incorporated into the death term of these cells as mediated by NK cells, modifying Eqs (A.7) and (A.8):

$$\frac{dI}{dt} = -\left(\frac{\delta_{I,K} IK}{K + \epsilon_{K,I}}\right)\left(\frac{\epsilon_{L,K}}{\epsilon_{L,K} + L_B}\right), \tag{A.10}$$

$$\frac{dT}{dt} = -\left(\frac{\delta_{T,K} TK}{K + \epsilon_{K,T}}\right)\left(\frac{\epsilon_{L,K}}{\epsilon_{L,K} + L_B}\right), \tag{A.11}$$

where $\epsilon_{L,K}$ is the half coefficient for the inhibition of NK cells by IL-6 measured in pg/ml.

In vivo observation supports that IL-6 reduces the cytolytic activity of NK cells, accompanied by the down-regulation of granzyme B and perforin. A negative correlation between the concentration of IL-6 and the cytolytic activity of NK cells in PF cells was observed and measured [234]. Using the parameters estimated previously for $\delta_{I,K}$ and $\epsilon_{I,K}$, the data of this correlation is used to fit to the equation for infected cells and yielded $\epsilon_{L,K} = 2.102 \times 10^{-5}$ pg/ml with 95% confidence interval of $(6.636 \times 10^{-6}, 3.546 \times 10^{-5})$ pg/ml (Figure A.1D).

We conducted additional validation using data [83] by graphing the effect of NK on infected cells with different doses of IL-6. Moreover, infected cells killed by NK cells were predicted with different IL-6 concentrations, as shown in Figure A.1E, to confirm the estimated parameter values.

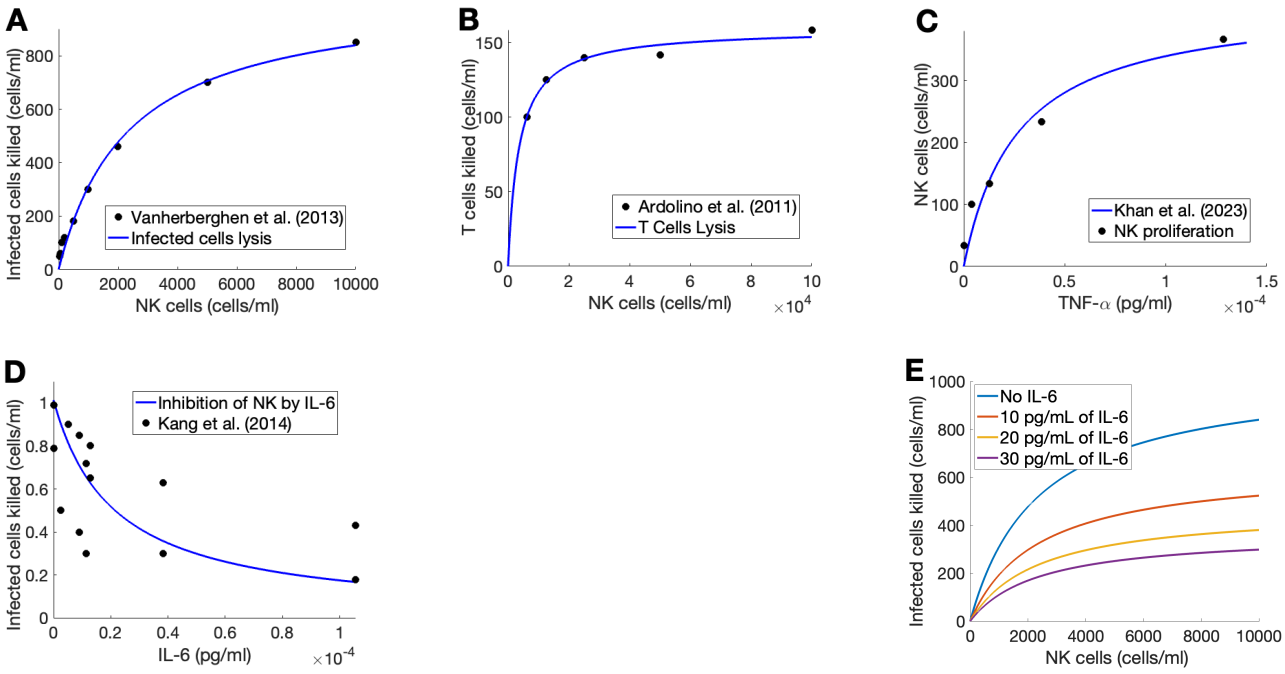


**Figure A.1.** Dynamics of NK cells on other immune cells and cytokines. A) Death rate of infected cells by NK cells (Eq (A.7)), B) Death rate of T cells by NK cells (Eq (A.8)), C) Proliferation of NK cells by TNF-$\alpha$ (Eq (A.9)), D) Inhibition of NK cytotoxicity by IL-6 was fitted to estimate the half-coefficient of the inhibition term (Eq (A.10)), and E) Infected cells killed by NK cells were predicted with different IL-6 concentrations for further confirmation.

TNF-$\alpha$ production by CD8$^+$ T cells

In order to model the production of TNF-$\alpha$ by CD8$^+$ T cells, we used the following fit:

$$\frac{d\alpha_U}{dt} = \frac{p_{\alpha,T}T}{T + \eta_{\alpha,T}}. \tag{A.12}$$

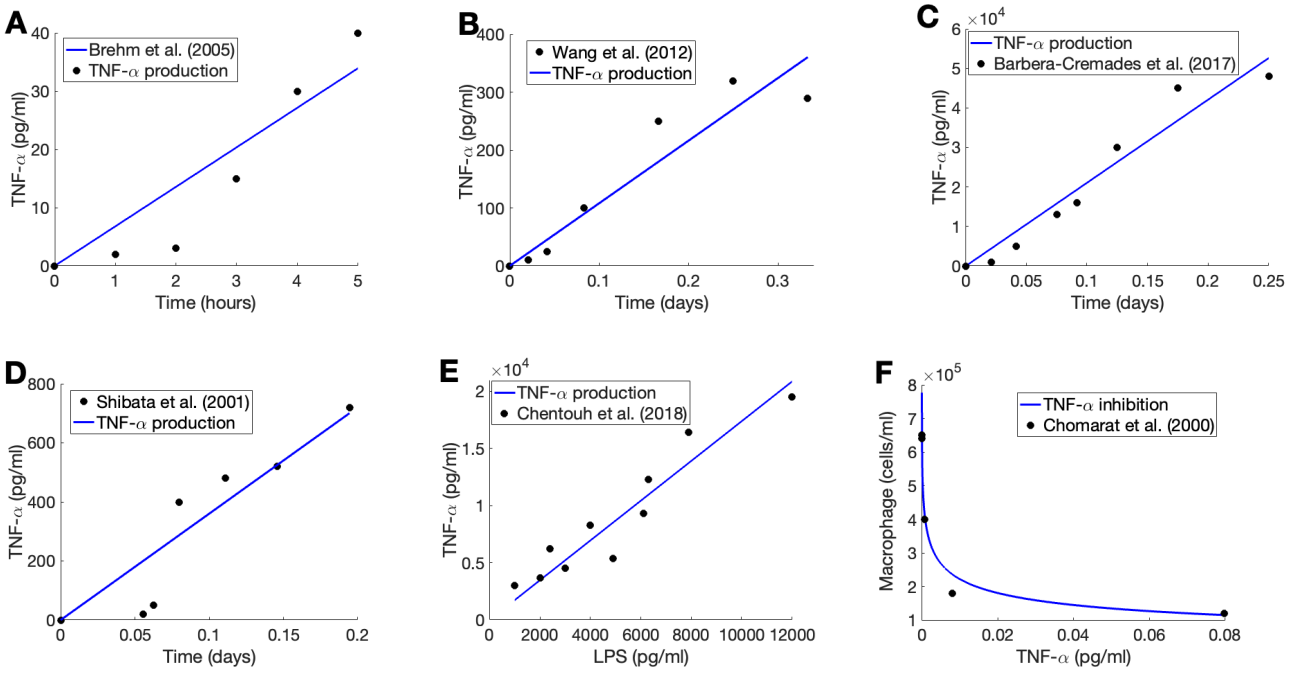


**Figure A.2.** TNF-$\alpha$ production by immune cells and its inhibition on the monocyte differentiation to inflammatory macrophages. **A)–B)** Fitting the equation of TNF-$\alpha$ production by CD8$^+$ T cells (Eq (A.12)) and NK cells (Eq (A.14)), where TNF-$\alpha$ cytokine levels (pg/ml) are expressed over time (hours and days, respectively). **C)–D)** Fitting the equations of TNF-$\alpha$ production by macrophages for maximum production rate and its half-effect concentration, (Eqs (A.15) and (A.16)), respectively, where cytokine levels (pg/ml) are expressed over time (days) with fixed macrophage concentration. Note that **A)–D)** show an intermediate, single-parameter estimation step used to obtain the half-effect coefficients in **A)–B)** and **D)** or maximum rate in **C)** for TNF-$\alpha$ production by immune cells from time-series data at fixed immune cell abundance; the linear fit, thus, reflects this estimation procedure rather than full model dynamics. **E)** Fitting the equation of TNF-$\alpha$ production by monocytes (Eq (A.17)), where TNF-$\alpha$ concentrations (pg/ml) are expressed over lipopolysaccharide (LPS) counts (pg/ml). Lastly, **F)** Fitting the equation of monocyte differentiation to macrophage, induced by IL-6 while being inhibited by TNF-$\alpha$ (Eq (A.18)), where macrophage production (cells/ml) is expressed over TNF-$\alpha$ cytokine levels (pg/ml) with IL-6 level fixed at 200 pg/ml.

The maximum production rate $p_{\alpha,T}$ was interpolated by using data in [196], showing the temporal production of TNF-$\alpha$ by activated CD8$^+$ T cells. This yielded a value of $p_{\alpha,T}$ = 900 pg/ml/2 days =

450 pg/ml/day. The half-effect of production $\eta_{\alpha,T} = 9.706 \times 10^{-5}$ (in $10^9$ cells/ml) was found using a combination of methods with a 95% confidence interval of ($5.816\times10^{-5}$, $1.366\times10^{-4}$) (in $10^9$ cells/ml). First, we used data from [200], which states the mean fluorescence of TNF-$\alpha$ in a $CD8^+$ T cell culture. Given that mean fluorescence is in RFU (relative fluorescence units), we fit the fluorescence values to a standard curve for TNF-$\alpha$ [201], which converts our fluroescence into TNF-$\alpha$ concentration. Using this process, we obtain a concentration for every time step. These values are then fitted using the term below:

$$\alpha_U = time \times \frac{p_{\alpha,T} T}{T + \eta_{\alpha,T}}. \tag{A.13}$$

Note that Figure A.2A illustrates an intermediate parameter-estimation step used to obtain the half-effect coefficient for TNF-$\alpha$ production by T cells, $\eta_{\alpha,T}$. Since the experimental data provide time-series measurements at a fixed T-cell abundance, with the maximal production rate being fixed at $p_{\alpha,T}$ = 450 pg/ml/day the half-effect parameter $\eta_{\alpha,T}$ is estimated from the effective linear-in-time production rate. Thus, this figure is not intended to validate the full dynamic model.

TNF-$\alpha$ production by NK cells

Similarly to monocytes, TNF-$\alpha$ secretion by NK cells is also found through data fitting. In the instance of NK cells, data found in [193, 197] is used for data fit to temporal TNF-$\alpha$ production by NK cells. The following fit is shown below:

$$\frac{d\alpha_U}{dt} = \frac{p_{\alpha,K} K}{K + \eta_{\alpha,K}}. \tag{A.14}$$

Through our findings, we discover that inactive NK cells secrete very little TNF-$\alpha$ levels [193, 197]. To gather accurate pathogenic behaviors in COVID-19 cases, we utilize studies where NK cells were activated by commonly found stimulants in the body [193]. This leads us to a maximum rate $p_{\alpha,K}$ of approximately 1000 pg/ml/day. We then used the fixed maximum rate to obtain the half effect $\eta_{\alpha,K}$ of 4.29 $\times10^{-4}$ (in $10^9$ cells/ml) with the 95% confidence interval of ($2.49 \times 10^{-4}$, $1.19 \times 10^{-3}$) (in $10^9$ cells/ml), as demonstrated in Figure A.2B. Similar to Figure A.2A, Figure A.2B also represents an intermediate, single-parameter estimation step (for $\eta_{\alpha,K}$ at fixed $K$ value) and is not intended as a validation of the full model dynamics.

TNF-$\alpha$ production by inflammatory macrophages

To model TNF-$\alpha$ production of inflammatory macrophages, we used the Hill function below:

$$\frac{d\alpha_U}{dt} = \frac{p_{\alpha,M_{\Phi I}} M_{\Phi I}}{M_{\Phi I} + \eta_{\alpha,M_{\Phi I}}}. \tag{A.15}$$

The half effect is obtained by fitting the term above to temporal production data from [198], giving us $\eta_{\alpha,M_{\Phi I}} = 2.22 \times 10^{-4}$ (in $10^9$ cells/ml) with the 95% confidence interval of ($3.74 \times 10^{-5}$, $1.32 \times 10^{-3}$) (in $10^9$ cells/ml), as shown in Figure A.2C. We then fit this half effect to a study by [187] which measured production of TNF-$\alpha$ under LPS stimulation. We incorporated LPS as a scalar, shown below:

$$\frac{d\alpha_U}{dt} = LPS \frac{p_{\alpha,M_{\Phi I}} M_{\Phi I}}{M_{\Phi I} + \eta_{\alpha,M_{\Phi I}}}. \tag{A.16}$$

This generates a max production rate of TNF-$\alpha$ by macrophages, $p_{\alpha,M_{\Phi I}}$ = 3824 pg/ml/day with the 95% confidence interval of (2981.43, 4533.9) pg/ml/day, as can be seen in Figure A.2D.

TNF-$\alpha$ production by monocytes

When pathogens invade a host, the immune defense includes cytokine secretion by differing cells [194]. During the innate response, monocytes secrete relevant levels of TNF-$\alpha$ [194]. To discover the rate in which monocytes secrete TNF-$\alpha$ upon invasion, we fit data found in multiple sources [194, 195] to the following equation:

$$\frac{d\alpha_U}{dt} = LPS\,\frac{p_{\alpha,M}M}{M+\eta_{\alpha,M}}. \tag{A.17}$$

From literature for TNF-$\alpha$ secretion [194, 195], we obtained the maximum production rate, $p_{\alpha,M}$ = 110 pg/ml. The half effect was obtained by fitting LPS data from [199]. This led us to $\eta_{\alpha,M}$ of 0.3851 $\times 10^9$ cells/ml with the 95% confidence interval of $(0.3248\times10^9, 0.4227\times10^9)$ cells/ml (Figure A.2E).

TNF-$\alpha$ inhibition of monocyte to macrophage differentiation

TNF-$\alpha$ is known to inhibit IL-6 induced monocyte to macrophage differentiation [60]. To capture this behavior, the modified equation from [14] is used, as follows:

$$\frac{dM_{\Phi I}}{dt} = \left(\frac{p_{M_{\Phi I},L}L_B M}{L_B+\epsilon_{L,M_{\Phi I}}}\right)\left(\frac{\epsilon_{\alpha,M_{\Phi I}}^{h_{M_{\Phi I},\alpha}}}{\epsilon_{\alpha,M_{\Phi I}}^{h_{M_{\Phi I},\alpha}}+\alpha_B^{h_{M_{\Phi I},\alpha}}}\right). \tag{A.18}$$

Parameter values for IL-6–induced monocyte-to -macrophage differentiation, $p_{M_{\Phi I},L}$ = 0.78 1/day, and $\epsilon_{L,M_{\Phi I}}$ = 0.001 pg/mL, were obtained from [14]. TNF-$\alpha$ inhibition of this differentiation process was then fitted to experimental data from [60], yielding $\epsilon_{\alpha,M_{\Phi I}}$ = 0.001093 pg/mL with a 95% confidence interval of ($1.32172\times10^{-7}$, 0.925648), and a Hill coefficient $h_{M_{\Phi I},\alpha}$ = 0.4 with a 95% confidence interval of ($3.69\times10^{-3}$, 72.64) (Figure A.2F).

In Eq (A.18), the Hill coefficient controls the steepness of TNF-$\alpha$–mediated inhibition, yielding minimal suppression at low TNF-$\alpha$ concentrations and strong inhibition at higher concentrations. This functional form reproduces the threshold-like regulatory behavior characteristic of cytokine-mediated control of monocyte-to-macrophage differentiation. We note that the confidence interval for the Hill coefficient is wide, reflecting limited identifiability of the steepness parameter from the available data and its correlation with the half-effect concentration. Nevertheless, the fitted inhibitory function captures the qualitative suppression of monocyte-to-macrophage differentiation by TNF-$\alpha$ supported by experimental observations.

Inflammatory macrophage death induced by TNF-$\alpha$ and IFN-$\gamma$

TNF-$\alpha$ and IFN-$\gamma$ have been shown to synergistically induce programmed cell death in inflammatory macrophages [52]. We captured this behavior through the following equation:

$$\frac{dM_{\Phi I}}{dt} = -\frac{\delta_{M_{\Phi I}}\alpha_B\gamma_B}{\alpha_B\gamma_B+\epsilon_{\gamma,\alpha}}. \tag{A.19}$$

Fitting the equation to data found in [52] yields $\delta_{M_{\Phi I}}$ = 0.1543 1/day, and $\epsilon_{\gamma,\alpha}$ = 1.994 $\times10^{-5}$ (pg/ml)$^2$ (see Figure A.3A). The 95% confidence interval for the death rate and half effect are (0.15, 0.16) 1/day and $(8.5\times10^{-6}, 3.14\times10^{-5})$ (pg/ml)$^2$, respectively.

Half-effect of IFN-$\gamma$ production by CD8$^+$ T cells

The half-effect concentration $\eta_{\gamma,T} = 8.37\times10^{-5}$ (in $10^9$ cells/ml) for production of IFN-$\gamma$ was found using data from [183]. This data is fit to the following equation and the fitted curve is provided in Figure A.3B. The 95% confidence interval is $(2.591 \times 10^{-6}, 1.65 \times 10^{-4})$ (in $10^9$ cells/ml).

$$\frac{d\gamma_U}{dt} = \frac{p_{\gamma,T}T}{T + \eta_{\gamma,T}}. \tag{A.20}$$

Half-effect of IFN-$\gamma$ production by NK cells

The following equation was fitted to the data in [193] to estimate the half-effect concentration $\eta_{\gamma,K} = 2.99 \times 10^{-4}$ (in $10^9$ cells/ml) for production of IFN-$\gamma$ by NK cells with the 95% confidence interval of $(10^{-4}, 1.1 \times 10^{-3})$ (in $10^9$ cells/ml). Similar to Figure A.2A–D, Figure A.3C depicts an intermediate step in estimating the half-effect coefficient for IFN-$\gamma$ production by NK cells. In this figure, the maximal production rate is fixed based on literature values, and the data is used solely to estimate the corresponding half-effect parameter from time-series measurements at a fixed NK cell concentration. As a result, the fitted trend shown in Figure A.3C is linear in time and is not intended as a validation of the full model dynamics.

$$\frac{d\gamma_U}{dt} = \frac{p_{\gamma,K}K}{K + \eta_{\gamma,K}}. \tag{A.21}$$

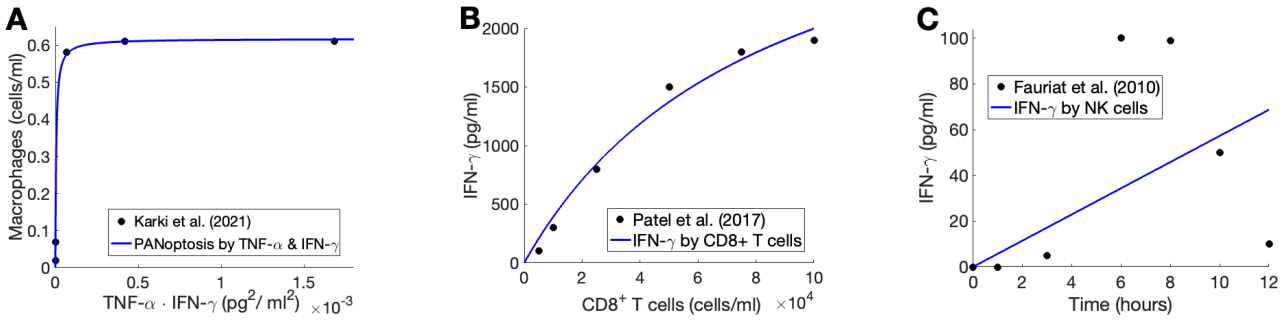


**Figure A.3.** Interactions between IFN-$\gamma$ and immune system. **A)** Equation (A.19) fitted to the death rate of inflammatory macrophages by varying combinations of TNF-$\alpha$ and IFN-$\gamma$: control, $2 + 1, 20 + 10, 50 + 25, 100 + 50$ ng/mL of TNF-$\alpha$ and IFN-$\gamma$, respectively [52]. This fit results in the production rate and half effect of Eq (A.19). **B)** Eq (A.20) was fitted to peptide stimulated production of IFN-$\gamma$. This fit was used to provide the half-effect constant of IFN-$\gamma$ production by CD8$^+$ T cells. **C)** Eq (A.21) was fitted to data for the IFN-$\gamma$ production by stimulated NK cells over $0, 1, 3, 6, 8, 10$, and 12 hours [193]. Note in this figure, while the maximal production rate is fixed, the data in [193] is used solely to estimate the corresponding half-effect parameter from time-series measurements at a fixed NK cell concentration. As a result, the fitted trend shown is linear in time and is not intended as a validation of the dynamic model.

*Parameters calculated from homeostasis*

The remaining parameters in the model are chosen to ensure that the immune system admits a biologically meaningful homeostatic state in the absence of infection. By *homeostasis*, we refer to the uninfected resting state of the immune system, in which immune cell populations and cytokine concentrations remain constant in time. Mathematically, this corresponds to a steady state satisfying $d/dt = 0$ for all model variables, with viral and resistant compartments set to zero ($V = R = 0$).

Rather than fitting these parameters directly to infection time-course data–where many of them are weakly identifiable–we use homeostasis as a biologically motivated constraint that restricts the admissible parameter space. Specifically, we impose steady-state conditions by setting the righthand side of each governing equation to zero and solving the resulting algebraic system,

$$\frac{dX_i}{dt} = 0,$$

for the corresponding homeostatic values $X_i^*$. These steady-state relations yield closed-form expressions linking parameters to baseline immune cell and cytokine levels, which we refer to as the homeostasis equations (Eqs (A.22)–(A.40)). The equations are solved sequentially by substitution, exploiting the hierarchical structure of the model and the biological dependencies among variables.

Importantly, this procedure does not uniquely determine all parameters; instead, it enforces balance between production, binding, and clearance processes so that the model admits a stable resting state consistent with physiological expectations. Any remaining free parameters are subsequently selected to ensure that the system returns to this homeostatic equilibrium following small perturbations in immune cell or cytokine concentrations. Together, these requirements define the homeostatic parameter set used throughout the model and ensure that baseline immune behavior is both biologically plausible and dynamically stable prior to infection.

The resulting homeostatic expressions (denoted by $X_i^*$) for immune cell populations, cytokines, and receptor-bound species are given below.

$$M_{\Phi I}(0) = M_{\Phi I}^* = \frac{\left(\frac{p_{M_{\Phi I},G} G_B^{*h_{M,M_\Phi}} M^*}{G_B^{*h_{M,M_\Phi}} + \epsilon_{G,M_\Phi}^{h_{M,M_\Phi}}} + \frac{p_{M_{\Phi I},L} L_B^* M^*}{L_B^* + \epsilon_{L,M_\Phi}}\right)}{\left(1 - \frac{M_{\Phi R}^*}{M_{\Phi max}^*}\right)\frac{\lambda_\Phi}{\epsilon_{V,M_\Phi}} + d_{M_{\Phi I}}}, \tag{A.22}$$

$$F_B(0) = F_B^* = \frac{k_{B_F} T^* A_F F_U^*}{k_{int_F} + k_{B_F} F_U^* + k_{U_F}}, \tag{A.23}$$

$$C_B(0) = C_B^* = \frac{k_{B_C} C_U^{*W_C} A_C N^*}{k_{int_C} + k_{B_C} C_U^{*W_C} + k_{U_C}}, \tag{A.24}$$

$$C_{BF}(0) = C_{BF}^* = \frac{C_B^*}{A_C N^*}, \tag{A.25}$$

$$L_B(0) = L_B^* = \frac{k_{B_L} (T^* + N^* + M^*) A_L L_U^*}{k_{int_L} + k_{B_L} L_U^* + k_{U_L}}, \tag{A.26}$$

$$G_B(0) = G_B^* = \frac{k_{B_G} M^* A_G G_U^*}{k_{int_G} + k_{B_G} G_U^* + k_{U_G}}, \tag{A.27}$$

$$\gamma_B(0) = \frac{k_{B_\gamma} A_\gamma \gamma_{U,0}(M_{\Phi I,0} + T_0)}{k_{B_\gamma}\gamma_{U,0} + k_{int_\gamma} + k_{U_\gamma}}, \tag{A.28}$$

$$\alpha_B(0) = \alpha_B^* = k_{B_\alpha}(T^*_{prod} + K(0) + M^*_{\text{prod}})A_\alpha \frac{\alpha_U^*}{(k_{int_\alpha} + k_{B_\alpha}\alpha_U^* + k_{U_\alpha})}, \tag{A.29}$$

$$\eta_{C,M} = \frac{p_{C,M}M^* - M^*(k_{lin_C}C_U^* + k_{B_C}(N^*A_C - C_B^*)C_U^{*W_C} - k_{U_C}C_B^*)}{k_{lin_C}C_U^* + k_{B_C}(N^*A_C - C_B^*)C_U^{*W_C} - k_{U_C}C_B^*}, \tag{A.30}$$

$$p_{L,M_\Phi} = \frac{M^*_{\Phi I} + \eta_{L,M_\Phi}}{M^*_{\Phi I}}\left(-\frac{p_{L,M}M^*}{M^* + \eta_{L,M}} + k_{lin_L}L_U^* + k_{B_L}\left((N^* + T^* + M^*)A_L - L_B^*\right)L_U^* - k_{U_L}L_B^*\right), \tag{A.31}$$

$$p_{G,M_{\Phi I}} = \frac{k_{lin_G}G_U^* + k_{B_G}(M^*A_G - G_B^*)G_U^* - k_{U_G}G_B^*}{\frac{M^*_{\Phi I}}{M^*_{\Phi I}+\eta_{G,M_\Phi}} + \frac{M^*}{M^*+\eta_{G,M}}}, \tag{A.32}$$

$$p_{M,G} = \frac{G_B^{*h_M} + \epsilon_{G,M}^{h_M}}{G_B^{*h_M}}\left(\frac{p_{M_\Phi,G}G_B^{*h_{M,M_\Phi}}M^*}{G_B^{*h_{M,M_\Phi}} + \epsilon_{G,M_\Phi}} + \frac{p_{M_{\Phi I},L}L_B^*M^*}{L_B^* + \epsilon_{L,M_\Phi}} + d_M M^*\right), \tag{A.33}$$

$$\eta_{F,M_\Phi} = \frac{p_{F,M_\Phi}M^*_{\Phi I} + \left(\frac{p_{F,M}M^*}{M^*+\eta_{F,M}} - k_{lin_F}F_U^* - k_{B_F}(T^*A_F - F_B^*)F_U^* + k_{U_F}F_B^*\right)M^*_{\Phi I}}{-\frac{p_{F,M}M^*}{M^*+\eta_{F,M}} + k_{lin_F}F_U^* + k_{B_F}(T^*A_F - F_B^*)F_U^* - k_{U_F}F_B^*}, \tag{A.34}$$

$$T^*_{prod} = d_T T^* - \frac{p_{T,L}L_B^*T^*}{L_B^* + \epsilon_{L,T}} - \frac{p_{T,F}F_B^*T^*}{F_B^* + \epsilon_{F,T}}, \tag{A.35}$$

$$p_{N,L} = N^*_{prod} = \left(d_N N^* - \frac{p_{N,L}L_B^*}{L_B^* + \epsilon_{L,N}}\right)\frac{1}{NR}, \tag{A.36}$$

$$p_{N,L} = N^*_{prod} = \frac{d_N N^*}{N_R + \frac{L_B^*}{L_B^*+\epsilon_{L,N}}}, \tag{A.37}$$

$$M^*_{\text{prod}} = \frac{\frac{1}{MR}\left(\frac{p_{M_{\Phi I},G}G_B^{*h_{M,M_\Phi}}M^*}{G_B^{*h_{M,M_\Phi}}+\epsilon_{G,M_\Phi}^{h_{M,M_\Phi}}} + \frac{p_{M_{\Phi I},L}L_B^*M^*}{L_B^*+\epsilon_{L,M}} + d_M M^*\right) - \psi_M^{max}\frac{G_B^{*h_M}}{G_B^{*h_M}+\epsilon_{G,M}^{h_M}}}{1 - \frac{G_B^{*h_M}}{G_B^{*h_M}+\epsilon_{G,M}^{h_M}}}, \tag{A.38}$$

$$K^*_{prod} = \left(p_K K_0 - \frac{p_{K,\alpha}\alpha_{B,0}K_0}{\alpha_{B,0} + \epsilon_{\alpha,K}}\right)\frac{1}{K_R}, \tag{A.39}$$

$$\eta_{L,M_\Phi} = \frac{M^*_{\Phi_I} - \frac{1}{p_{L,M_\Phi}}\left(-\frac{p_{L,M}M^*}{M^*+\eta_{L,M}} + k_{lin_L}L_U^* + k_{B_L}((N^* + T^* + M^*)A_L - L_B^*)L_U^* - k_{U_L}L_B^*\right)M^*_{\Phi_I}}{\frac{1}{p_{L,M_\Phi}}\left(-\frac{p_{L,M}M^*}{M^*+\eta_{L,M}} + k_{lin_L}L_U^* + k_{B_L}((N^* + T^* + M^*)A_L - L_B^*)L_U^* - k_{U_L}L_B^*\right)}. \tag{A.40}$$

*Additional model results*

Additional model results for comparing mild and severe COVID-19 dynamics, which are not included in Figure 2, are provided in Figure A.4. Also, the complete heatmap from local sensitivity analysis (in addition to top 23 sensitive parameters shown in Figure 3) is attached.

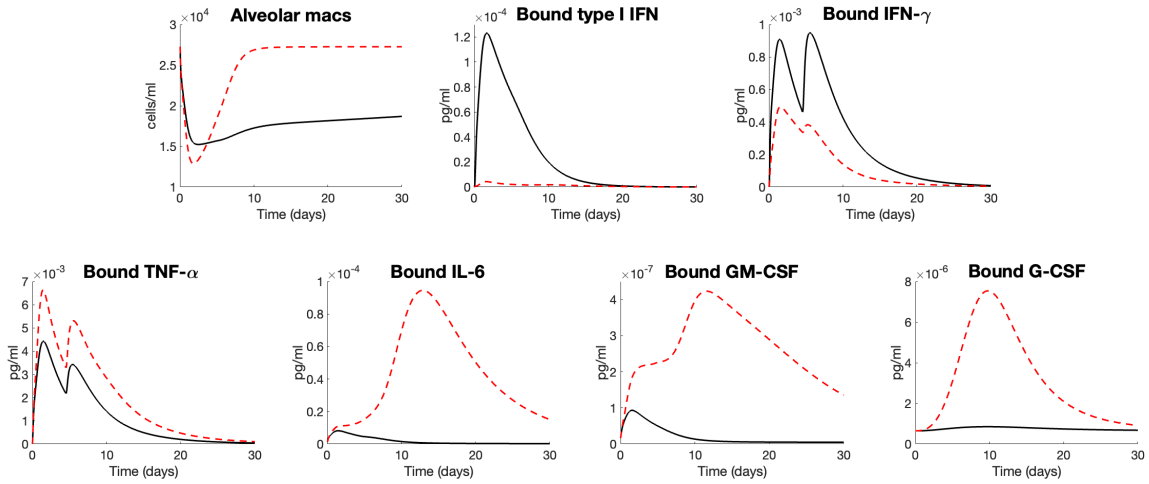


**Figure A.4.** Model predictions for mild vs. severe COVID-19 dynamics (for all other variables). Mild disease (solid lines) dynamics obtained by solving Eqs (2.1)–(2.23) with baseline parameters summarized in Tables A.3–A.12. The graphs depict the predicted concentrations of resident macrophages and all bound cytokines over the course of a 30-day infection, and those for all other model variables can be found in Figure 2.